INTERACTION OF 157-NM EXCIMER LASER LIGHT WITH FUSED SILICA, POLYTERTRAFLUOROETHYLENE AND CALCIUM FLUORIDE

By

SHARON ROSE GEORGE

A dissertation submitted in partial fulfillment of the requirement for the degree of

DOCTOR OF PHILOSOPHY

WASHINGTON STATE UNIVERSITY
Department of Physics and Astronomy

May 2010

To the Faculty of Washington State University:

The members of the Committee appointed to examine the dissertation of Sharon Rose George find it satisfactory and recommend that it be accepted

_____

J. T. Dickinson, Ph.D, Chair

_____

Gary Collins, Ph.D.

_____

Kerry Hipps, Ph.D.

_____

Yi Gu, Ph.D

ACKOWLEDGEMENT

I would like to express my gratitude to my Dr. J. Thomas Dickinson, for his guidance and support during this work. My thanks to Dr. Stephen C. Langford for his valuable suggestions in data analysis. I would also like to thank John A. Leraas for teaching me experimental techniques in the lab during the early months of my research. He also contributed to the study of positive ion emission from fused silica that is presented in this thesis. I also wish to thank Enamul Khan, Mingdong Cai and Forrest Stevens for their assistance in the lab.

This work was supported by the Department of Energy under grant DE-FG02-04ER-15618.

INTERACTION OF 157-NM EXCIMER LASER LIGHT WITH FUSED SILICA, POLYTERTRAFLUOROETHYLENE AND CALCIUM FLUORIDE

ABSTRACT

By
Sharon Rose George, Ph.D.
Washington State University
May 2010

Chair: J. Thomas Dickinson

Emission of positive ions, neutral atoms and molecules and negative ions was observed during 157-nm irradiation of fused silica. Positive ion emission from fused Silica is best explained by a hybrid mechanism involving (a) excitation of an antibonding chemical state (Menzel-Gomer-Redhead mechanism) and (b) acceleration of the positive ion by repulsive electrostatic forces due to the photoionization of nearby electron traps. Neutral emission results from the absorption of single 157 nm photons that cleave strained bonds to produce defects that subsequently diffuse to the surface. There then react with dangling bonds to release neutral atoms and molecules. Negative ions are created *after* the laser pulse, by electron attachment to the neutral particles.

Time- and mass-resolved measurements on neutral particles emitted PTFE during exposure to 157-nm laser radiation. We observe neutral $(CF_2)_N$ radicals for all N up to the limit of our mass filter (N = 6). These radicals are emitted directly from the surface with high kinetic energies of about 0.6 eV of the fastest $(CF_2)_N$ radicals consistent with photochemical scission of the polymer backbone. A great majority of emitted material is in the form of heavier fragments ranging from 300 to 2000 amu. The presence of heavy and light particles in the cloud of emitted particles gives rise to some unique behavior in the way it expands. The trajectories of the

heaviest fragments are preferentially directed at large angles away from the surface normal—often nearly parallel to the substrate surface. This behavior is due to density and pressure gradients associated with the Gaussian intensity profile of the laser beam.

Transient absorption was observed in Calcium Fluoride during 157-nm irradiation with peaks at 153 nm, 220 nm and 375 nm under 157-nm irradiation due to the H_s^- center, Ca^{1+} interstitial and the F-center respectively. Capture of a hole by H_s^- center, Ca^{1+} interstitial destroys the absorption and trapping of an electron at H_i^0 center and the Ca^{2+} interstitial re-induces absorption. Aggregation of F-centers to form M-centers leads to loss of absorption at 375 nm and the dissociation of the M-center when irradiation is restored re-induces absorption.

TABLE OF CONTENTS

LIST OF FIGURES

CHAPTER ONE

CHAPTER TWO

CHAPTER THREE

CHAPTER FOUR

CHAPTER FIVE

CHAPTER SIX

Dedication

This thesis is dedicated to my husband Billy George, my parents Reymond and Lalitha John, my Aunt and Uncle Bala and Ashok Lalli, my grandmother Mary Spratt and everyone in my wonderful family back in India and here in the U.S.A. for their love, support and encouragement through these years.

FORWARD

This thesis is largely composed of material previously published or to be submitted for publication including text and/or figures from the following references

S. R. George, J. A. Leraas S. C. Langford, and J. T. Dickinson, "Interaction of vacuum ultraviolet excimer laser radiation with fused silica: I. Positive ion emission," J. Appl. Phys. **107,** 033107 (11) (2010).

S. R. George, S. C. Langford, and J. T. Dickinson, "Interaction of vacuum ultraviolet excimer laser radiation with fused silica: II. Neutral atom and molecule emission," J. Appl. Phys. **107,** 033108 (11) (2010).

S. R. George, S. C. Langford, and J. T. Dickinson, "Interaction of vacuum ultraviolet excimer laser radiation with fused silica: III. Negative ion formation," J. Appl. Phys. **107,** 033109 (10) (2010).

S. R. George, J. A. Leraas, S. C. Langford, and J. T. Dickinson, "Interaction of 157-nm excimer laser radiation with fluorocarbon polymers," Appl. Surf. Sci. **255,** 9558-9561 (2009).

S. R. John, S. C. Langford, and J. T. Dickinson, "Ablation mechanism of PTFE under 157 nm irradiation," Appl. Phys. A **92,** 981-985 (2008)

S R. George, S. C. Langford and J. T. Dickinson, “Interactions between fluorocarbon polymers and 157-nm excimer laser radiation I: Emission of $(CF_2)_N$ fragments from polytetrafluoroethylene,” to be submitted to J. Appl. Phys. (2010)

S R. George, S. C. Langford and J. T. Dickinson, “Interactions between fluorocarbon polymers and 157-nm excimer laser radiation II: Off-normal trajectories of heavy molecules during ablation of PTFE,” to be submitted to J. Appl. Phys. (2010)

S R. George, S. C. Langford and J. T. Dickinson, “157 nm laser induced transient absorption centers in CaF_2,” to be submitted to J. Appl. Phys. (2010)

GENERAL INTRODUCTION

Over the last decades the F_2 (157 nm) excimer laser has obtained the key position among lasers in various sectors of micromachining and in pulsed laser deposition. Because of its short wavelength this laser offers excellent quality of machining and a great versatility in features which can be produced. Understanding the interaction of 7.9 eV photons with wide band gap materials like fused silica and polymers like polytetrafluoroethylene (PTFE) can be beneficial to laser machining and pulsed laser deposition applications. Both these materials absorb strongly at 157 nm unlike other wide band gap materials like Calcium Fluoride. Particle emission is a valuable probe of interactions between these materials and laser radiation. In this study neutral and ion emission from these two materials was characterized to reveal details involving bond breaking and photodecomposition of these two materials under 157-nm irradiation.

Synthetic fused Silica is an important UV optical material but absorption due to disorder-related states in the band gap renders fused silica unsuitable for most optical applications at 157 nm (7.9 eV photons. Measurements of positive ions (Si^+ and O^+) neutral atoms and molecules (O, Si and SiO) and negative ions (O^- and Si^-) emitted from fused silica during 157-nm laser irradiation at fluences well below the threshold for optical breakdown are described in Chapters 1-3. Positive ions with several eV of kinetic energy are emitted from surface defect states by a combination of photoexcitation and photoionization processes. Neutral atoms and molecules are emitted by defect interactions along the surface; these defects are produced principally by the photo-induced cleavage of strained bonds and negative ions are formed by the attachment of electrons to neutral atoms.

Polytetrafluoroethylene (PTFE) is a chemically stable, biocompatible polymer with a low surface energy, low coefficient of friction, and high resistivity. Although these properties are desired in many applications, its use is often hindered by its poor machinability using conventional techniques. Precision etching of PTFE has been demonstrated using 157-nm

excimer lasers. High quality thin films have also been deposited by laser ablation deposition at 157 nm. These results have been attributed in part to the photodecomposition of PTFE at 157-nm. That said, the evidence for photochemical decomposition at 157 nm has not been entirely unequivocal; some other groups have proposed thermal decomposition as the mechanism for particle emission.

Chapter 4 of this work shows that the primary neutral products of ablation of PTFE at 157 nm are $(CF_2)_N$ fragments. These $(CF_2)_N$ fragments are consistent with random photochemical scission of the polymer chain. The fastest of the fragments at each mass have kinetic energies of about 0.6 ± 0.2 eV, independent of fluence. These energies are well above typical thermal energies which are usually less than 0.2 eV, and support a photochemical emission mechanism.

The presence of heavy and light particles in the cloud of emitted particles, during 157 nm ablation of PTFE, gives rise to some unique behavior in the way it expands. The cloud in this case is a mixture of neutral fragments ranging from 50 amu to 2000 amu. Heavy fragments were found to be preferentially emitted in paths away from the surface and almost parallel to the surface while the lighter fragments are more forward directed. We propose in, Chapter 5, that this behavior is due to pressure gradients created due to the distribution of masses from the center of the laser spot toward the edges due to the Gaussian profile of the laser beam. The presence of heavy fragments emitted during laser ablation is very advantageous to thin film growth by pulsed laser deposition as it eliminates the need for the substrate to be heated to drive polymerization reactions. Also, high quality films were successfully deposited at room temperature on silicon wafers placed above and below the samples in this work. Moreover our calculations show that it may be possible to deposit larger uniform thin-films by using two laser beams to create pressure gradients in the plume.

Chapter 6 is a study of the interaction of single crystal Calcium Fluoride (CaF_2) with 157 nm irradiation. CaF_2 is an ionic crystal with a band gap of 11.8 eV. This wide band gap contributes to the damage resistance of this material, which is much greater than fused silica at

wavelengths less than 200 nm and is therefore used for making optics for 157 nm applications. That said, the optical properties of CaF_2 can be degraded by two-photon processes at 157 nm that generate defects, including vacancy-interstitial pairs. F-center aggregation can lead to the production of metallic Ca nanoparticles. On occasion, transient absorption features have been observed during 157-nm and 193-nm excimer laser radiation.

In this work, both transient VUV and UV absorption changes during 157-nm irradiation in CaF_2 with absorption peaks at 153 nm, 220 nm and 375 nm were observed. The transient absorptions at 153 and 220 nm are typically superimposed on persistent absorption changes. The absorption near 153-nm is consistent with absorption due to the substitutional hydride ion, H_s^-. Consistent with this identification, this absorption is strengthened by high temperature annealing in hydrogen gas. We attribute the absorption near 220 nm to electrons trapped at a Ca^{2+} interstitials, and the absorption near 375 nm to the F-center. We propose that charge transfer to and from substitutional H_s^- and interstitial Ca^{2+} centers can rapidly change the absorption intensities at 153 and 220 nm. This charge transfer is facilitated in the presence of ionizable electron traps, including the F and M centers, which are produce during 157-nm irradiation. In the case of the F-center aggregation of F-centers to form M-centers leads to loss of absorption at 375 nm and the dissociation of the M-center when irradiation is restored re-induces absorption

CHAPTER ONE

Interaction of vacuum ultraviolet excimer laser radiation with fused silica: I. Positive ion emission

Sharon R. George, John A. Leraas, S. C. Langford, and J. T. Dickinson

Abstract

We report time- and mass-resolved measurements of Si^+ and O^+ emission from ultraviolet-grade fused silica during exposure to pulsed, 157-nm excimer laser radiation at fluences below the threshold for optical breakdown. The emission intensities are increased by treatments that increase the density of surface defects, such as abrasion, and reduced by treatments that reduce the density of surface defects, such as annealing. Ion emission is a sensitive probe of mechanical damage on silica surfaces. The mean ion kinetic energies are typically several eV: 8-9 eV for Si^+ and about 4 eV for O^+. Hartree-Fock studies of candidate defect sites suggest that antibonding states excited by 157-nm photons play a critical role in the release of these ions. We propose that positive ion emission from fused silica under these conditions is best explained by a hybrid mechanism involving (a) the excitation of an antibonding chemical state (Menzel-Gomer-Redhead mechanism) and (b) acceleration of the positive ion by repulsive electrostatic forces due to the photoionization of nearby electron traps.

1. Introduction

Despite fused silica's 8.9 eV bandgap, it is unsuitable for optical applications which employ the 7.9 eV photons produced by F_2 excimer lasers. This failure is attributed to an Urbach tail of disorder-related states that extend well below the conduction band.[1] Absorption due to these states has been used to explain the well known clean etching of fused silica surfaces by F_2 excimer lasers.[2-4] Here we describe the emission of positive ions during 157-nm irradiation in the absence of optical breakdown and at fluences below those required to substantially etch the material used in this work. This avoids complications due to high charge densities and potential ionization in the ablation plume. Under our conditions, the intensity, mass, and time-of-flight measurements strongly constrain proposed mechanisms for ion emission.

Positive ion emission (PIE) often accompanies ultraviolet laser irradiation of wide band gap materials, at photon energies below bandgap and at fluences below the threshold for optical breakdown.[5-8] In ionic materials, ions sorbed at surface defect sites can be ejected by repulsive electrostatic forces when the underlying defects are photoionized by the laser.[7,9-11] In contrast with these ionic materials, the bonding in silica is predominately covalent. The forces associated with bonding-to-antibonding transitions in covalent bonds are responsible for the desorption of neutral particles by the Menzel-Gomer-Redhead mechanism.[12,13] We find that the excitation of antibonding chemical states plays an important role in ion emission from fused silica. Nevertheless, the ions we observe have kinetic energies of several eV and require additional repulsive electrostatic forces. We therefore propose that ion emission is best described in terms of a hybrid mechanism, described in detail below.

This study characterizes ion emission from a typical high-OH silica, Suprasil 2, (Heraus-Amersil, about 1200 ppm OH) produced by exposure to pulsed 157-nm radiation at fluences below the threshold for optical breakdown. Time-resolved quadrupole mass spectroscopy shows that the principle ions are Si^+ and O^+. The mean kinetic energy of the Si^+ ion is typically 8-9

eV—somewhat greater than the 7.9-eV energy of 157-nm photons; the mean kinetic energy of the O^+ ion is lower, about 4 eV. Both Si^+ and O^+ intensities are strongly affected by mechanical and thermal treatments that alter the density of surface point defects.

To help identify the relevant defects, the geometry and electronic structures of silica clusters incorporating a variety of plausible emission sites were modeled by Hartree-Fock methods. We show that clusters incorporating the surface Si-Si^+ dimer, with Si^+ adsorbed on a surface Si atom, have electronic structures suitable for Si^+ emission. Similarly, the surface peroxy group (O-O^+ dimer) is a possible source of O^+. Both defect structures show localized molecular orbitals with strong antibonding character that can be excited by one or more 157-nm photons. Since the emitted ions are positively charged and have kinetic energies of several eV, electrostatic forces must also be important. Furthermore, these ions serve as a highly sensitive probe for the relevant surface defects, including changes in defect densities due to and mechanical, thermal, or optical stimuli.

In two companion papers (Parts II and III of this series), we describe the emission of neutral particles (atoms and molecules) [14] from Suprasil 2 under comparable conditions, as well as the production of negative ions by electron attachment to the emitted neutral particles. [15]Strong ties between negative ion formation and *both* the neutral and the positive ion emissions are presented.

2. Experiment

Samples were cut from UV grade fused silica (Suprasil 2, ≈ 1 ppm metal content; ≈ 1200 ppm OH) from Heraus-Amersil using a diamond saw. After cleaning in ethanol, some samples were tested as cut. Others were abraded with 600-grit SiC sandpaper, and others were polished to a 0.25-μm surface finish with diamond paste. Plastically deformed samples were prepared by producing an array of indents on polished surfaces with a diamond scribe; care was taken to avoid fracture. Annealed samples were prepared by heating polished samples to 1100 °C for

eight hours. Although these treatments can contaminate the sample surface with carbon- and hydrogen-containing species, OH, H_x, and CO were *not* detected under the conditions of this work. We believe any contaminants were desorbed by the first few laser pulses and did not contribute significantly to the observed emissions.

Mass-selected time-of-flight measurements were performed in a vacuum chamber with a base pressure of about 3×10^{-7} Pa. A Lambda Physik LPF200 laser (F_2 excimer) provided 20-ns pulses of 157-nm laser radiation at a pulse repetition rate of 5 Hz. The beam was focused into a 0.009 cm^2 spot with a CaF_2 lens. Samples were mounted on a translation stage directly in front of and normal to the axis of a UTI 100C quadrupole mass spectrometer. The average electric fields along the axis of the mass filter were perpendicular to the ion trajectory and thus had little effect on the ion time-of-flight from the sample to the exit aperture of the mass filter. All nearby metal surfaces were maintained at ground potential. Thus the apparatus, including the quadrupole mass filter, functioned as a time-of-flight tube at ground potential with a length equal to the distance between the sample and the exit aperture of the mass filter. Ions exiting the mass filter were detected with a Channeltron electron multiplier biased for the detection of positive ions and operated in the pulse-counting mode. The output of the detector was amplified, discriminated, and pulse counted over 200-ns intervals with an EG&G PARC 914P multichannel scalar. Unless otherwise noted, the signals presented below represent the average emission accompanying 200 successive pulses on the same spot.

To characterize the ion kinetic energies, the quadrupole mass-selected time-of-flight (TOF) signals were fit to functions representing the particle flux of ions with a one-dimensional Gaussian energy distribution with a mean kinetic energy E_0 and standard deviation σ. If these ions are emitted along the surface normal at time $t = 0$, their flux $I(t)$ at a detector mounted a distance d (= 0.28 m) from the sample at time t is given by:

$$I(t) = \frac{N_I m d^2}{\sqrt{2\pi}\,\sigma t^3} \exp\left\{\frac{-\left[E(t) - E_0\right]^2}{2\sigma^2}\right\} , \qquad (1)$$

where N_I is the total number of detected ions and $E(t)$ ($= mv^2/2 = md^2/2t^2$) is the kinetic energy of an ion of mass m arriving at the detector at time t after the laser pulse.

To characterize defect production a function of fluence, we exposed samples to measured doses of 157-nm radiation, removed them from the vacuum system, and measured the near-ultraviolet transmission in the irradiated region with a Perkin Elmer Lambda 9000 UV-VIS-NIR spectrophotometer. This instrument was also employed for diffuse reflectance measurements on abraded silica surfaces. Vacuum ultraviolet spectra were acquired *in situ* after 157-nm irradiation with a McPherson 302 monochromator mounted on the experimental vacuum chamber.

Electron-hole pair production was probed by monitoring the luminescence produced by the decay self-trapped excitons (STE) at 80 K. The 157-nm laser beam was directed through silica samples held at liquid nitrogen temperature, and the resulting luminescence spectra were acquired with a Roper Scientific PI-Max 512RB gated, intensified CCD camera mounted at the exit aperture of a Jarrel Ash Monospec 18 monochromator. The STE luminescence is due a spin forbidden, triplet-to-singlet transition[16] which has a lifetime of milliseconds.[17] This long lifetime allowed us to delay the onset of data acquisition by 100 μs without significantly reducing the luminescence intensity. The energy of STE photons emitted immediately after the laser pulse is about 2.05 eV;[18] the large difference between the photon energy and the band gap is due to an exceptionally large Stokes shift.[19] Importantly, the STE photon energies gradually blue-shift with time after excitation to about 2.4 eV after 100 μs.[18] In our uncorrected photoluminescence spectra, this peak appears at 2.5 eV.

3. Results and Discussion

3.1 Positive ion emission

At fluences between 1 and 3 J/cm^2 the only ions observed during pulsed 157-nm laser radiation are Si^+ (28 amu/e) and O^+ (16 amu/e). For comparison purposes, we note that the breakdown threshold we measure for polished Suprasil 2 under UHV conditions is about 3.5 J/cm^2. The ionization potentials of atomic O and Si are significantly greater than the 7.9 eV photon energy (13.6 and 8.2 eV, respectively);[20] thus we rule out ion production by single-photon ionization of neutral atoms after emission. Likewise, gas phase multiphoton ionization is not likely at these low power densities. We conclude that Si^+ and O^+ are emitted directly from the surface as ions. Interestingly, the excimer laser fluence required to generate significant positive ion emission from fused silica is about 15 times higher than the fluence required to produce comparable positive ion emissions from ionic single crystals such as the alkali halides.[21]

Si^+ and O^+ time-of-flight (TOF) signals from polished silica, averaged over the first 200 laser pulses, are shown in Fig. 1. The Si^+ signal reproducibly displays two peaks in time, one near 28 μs and the other near 35 μs. Fitting the signals in Fig. 1 with the sum of two Gaussian distributions from Eq. (1) yields mean kinetic energies E_0 of 8.6 and 8.2 eV, respectively. Sample-to-sample and spot-to-spot variations result in uncertainties (in E_0) of about ±1 eV. The widths of the corresponding energy distributions [full-widths at half-maxima, from σ in Eq. (1)] are typically 4-6 eV. These energy distributions do not change significantly as the fluence is increased from 1 to 2.6 J/cm^2.

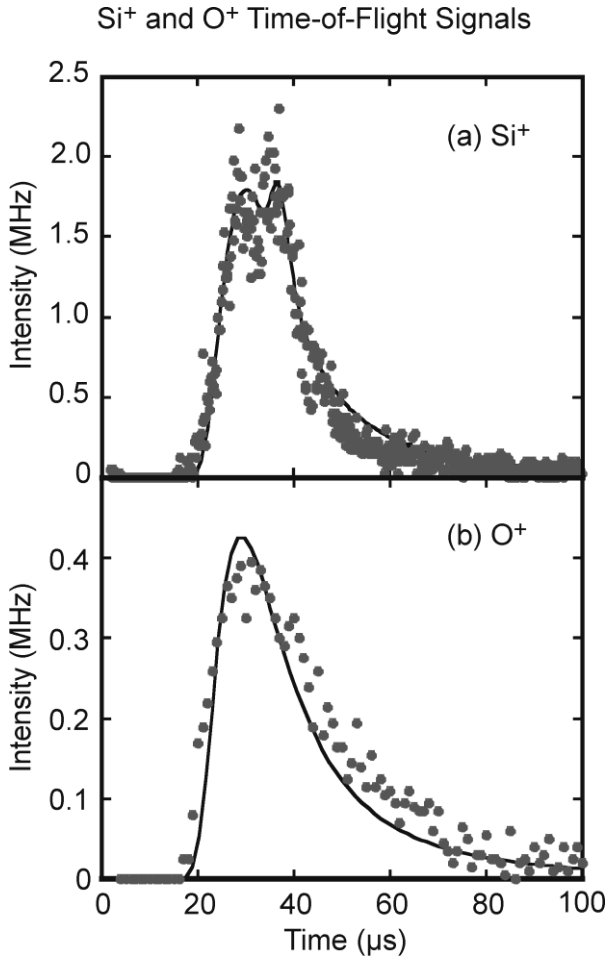

Fig. 1. Mass selected time-of-flight signals for ions from polished silica under 157-nm irradiation: (a) Si^+ at 2.2 J/cm^2, and (b) O^+ at 2.5 J/cm^2. The dark lines are least-squares fits of Eq. (1) to the data, employing the sum of two Gaussian energy distributions in (a) and one in (b).

Under the same conditions, the O^+ signals are typically weaker and display a single peak about 25 μs after the laser pulse, as shown in Fig. 1(b). Least squares fits of Eq. (1) to the O^+ signals yield peak kinetic energies of ~4 eV and full-widths at half-maxima of about 8 eV. Although the peak of the O^+ TOF signal nearly coincides in time with the peak in the Si^+ signal, the O^+ signal is significantly broader. As with Si^+, the O^+ energy distributions change little with laser fluence.

Both ion intensities are strong functions of laser fluence, as shown in Fig. 2. The Si^+ emission intensity varies roughly with the 1.7^{th} power of fluence; thus we expect that Si^+ emission requires (on average) more than one photon. The O^+ intensity is a much stronger function of fluence, varying with the 5.3^{th} power of fluence. Comparable nonlinear fluence dependences have been observed in our previous studies of ion emission due to 248-nm radiation, including Mg^+ from MgO, Na^+ from $NaNO_3$, and alkali ions from various alkali halides.[7,9,21-23]

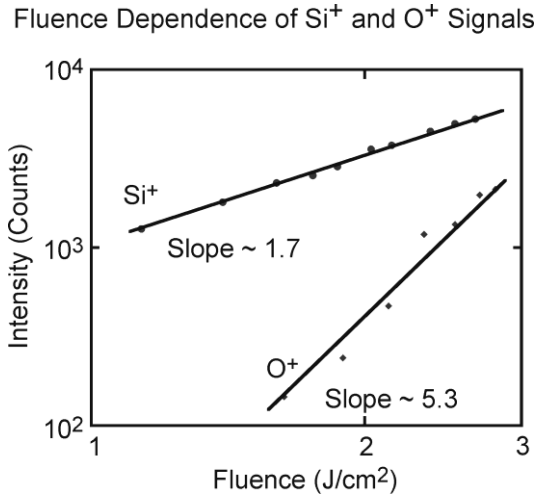

Fig. 2. Si^+ and O^+ intensities versus fluence from as-cut fused silica.

Positive ion emission from ionic crystalline materials has been attributed to the desorption of ions adsorbed near ionizable surface electron traps, such as anion vacancies.[7,21,24,25] Surface defects such as atomic dimension steps and kinks offer possible sites for initial binding states. When the underlying defect is photoionized, the net electrostatic force on the sorbed ion (adion) becomes strongly repulsive, and the adion is ejected with considerable kinetic energy. Ion ejection involving repulsive Coulomb forces involves a sequence of photon absorption events that photoionize other electron traps near the adion. This gives rise to the higher order fluence dependencies observed in these ionic materials.

Ion emission sites in covalently bonded fused silica would involve Si^+ and O^+ adsorbed on surface defects that serve as electron traps, such as the E' center and the nonbridging oxygen hole center (NBOHC). High densities of surface E' centers have been detected by electron spin resonance on mechanically treated silica surfaces.[26] UV reflectivity measurements (shown below) on our abraded samples display features near 210 and 250 nm that are consistent with absorption due to the E' center[27] and the NBOHC, respectively.[28] At the surface, these defects would provide favorable sites for positive ion sorption and laser-stimulated desorption.

If the ion-desorption sites responsible for ion emission are produced by mechanical treatments, it is reasonable to expect mechanical treatments to increase the intensity of the laser-induced ion emissions. The bar graph in Fig. 3 shows the relative Si^+ and O^+ intensities during exposure to 2.5 J/cm^2 pulses of 157-nm radiation from surfaces with five different surface treatments. As-cut surfaces (cut with a diamond saw) yield relatively intense emissions. Treatments expected to yield lower surface defect densities, such as annealing and polishing, reduce the ion intensities. Conversely, treatments expected to produce higher surface defect densities, such as abrading and indenting, increase the ion intensities. Our previous studies have shown that surface defects play important roles in ion emission from other wide bandgap materials as well.[7,9,21-23,29]

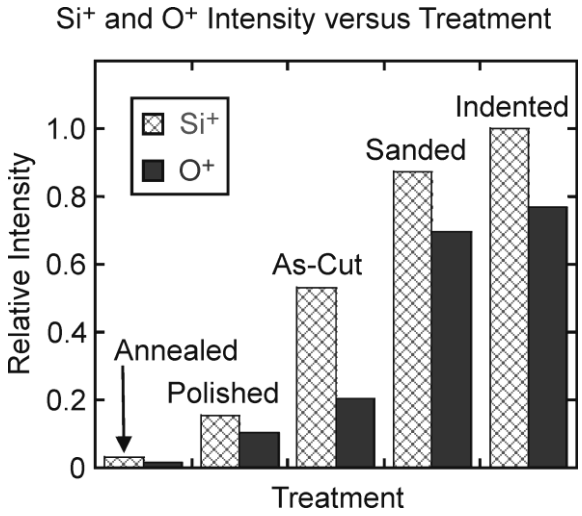

Fig. 3. Si^+ and O^+ intensities (relative units) from fused silica surfaces exposed to 157-nm radiation at a fluence of 2.5 J/cm^2. The annealed sample was held at 1100 °C for eight hours. The polished sample was smoothed to a 0.25-μm finish with diamond paste. The abraded sample was roughened with 600 grit, SiC sandpaper. An array of indentations was produced on the indented surface with a diamond scribe.

The strong influence of surface treatment on ion intensity can be exploited to detect damaged surface material. Figure 4 shows a series of Si^+ and O^+ intensity measurements made while scanning a 1.5-mm laser spot across a scratch on a polished silica surface. (The scratch, made with a diamond scribe, was about 100 μm wide.) As the laser spot encounters the scratch, the Si^+ and O^+ intensities rise by a factor of four. Since the scratch is much thinner than the laser spot, the contrast between ion intensities (per unit sample area) from damaged and undamaged material is significantly underrepresented. Further, the great majority of the ions emitted from the sample are not transmitted through the mass filter employed to collect the data in Fig. 4. Orders-of-magnitude higher sensitivities are possible. (Near-unity detection efficiencies can be achieved with ion detectors mounted near the sample.) Similarly, the spatial resolution for damage detection can be improved by focusing the laser beam into a smaller spot. This sensitivity to damage may be of practical utility as a non-contact probe of surface damage. Mechanical defects can render optics especially prone to catastrophic failure at high fluences.[30,31] For example, we observe optical breakdown on polished silica surfaces at fluences above 3.5

J/cm^2; whereas on diamond-abraded surfaces, we observe breakdown at fluences below 2.7 J/cm^2.

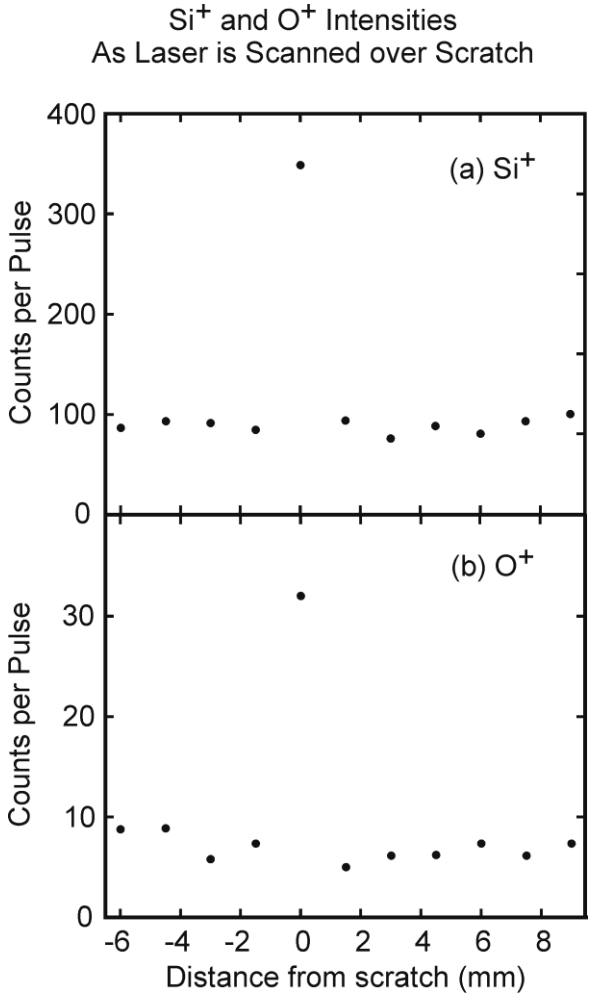

Fig. 4. (a) Si^+ and (b) O^+ intensities versus position along a polished silica surface with a single scratch. The laser beam was scanned across the scratch at a fluence of 1.9 J/cm^2.

3.2 Effect of prolonged irradiation

Ion emission. Over the course of thousands of laser pulses, the intensity of the Si^+ and O^+ signals varies dramatically. Figure 5(a) shows how the Si^+ intensity from a polished sample varies during exposure to 1.5 J/cm^2 pulses at a pulse repetition rate of 1 Hz. The Si^+ intensity falls by at least an order of magnitude—rapidly during the first 200 pulses and more gradually

for another 2000 pulses. Subsequently, the intensity slowly increases. Under the same conditions, the O^+ intensity drops markedly during the first 800 pulses and subsequently plateaus at a level well above background, as shown in Fig. 5(b). In each of these measurements, the laser exposure was interrupted for 200 s after 4800 pulses and again after 6400 pulses. No discontinuity in the ion intensities at these exposures is observed when the laser beam is temporarily blocked. Therefore accumulative, pulse-to-pulse heating, if any, is *not* responsible for the observed intensity changes during prolonged exposure.

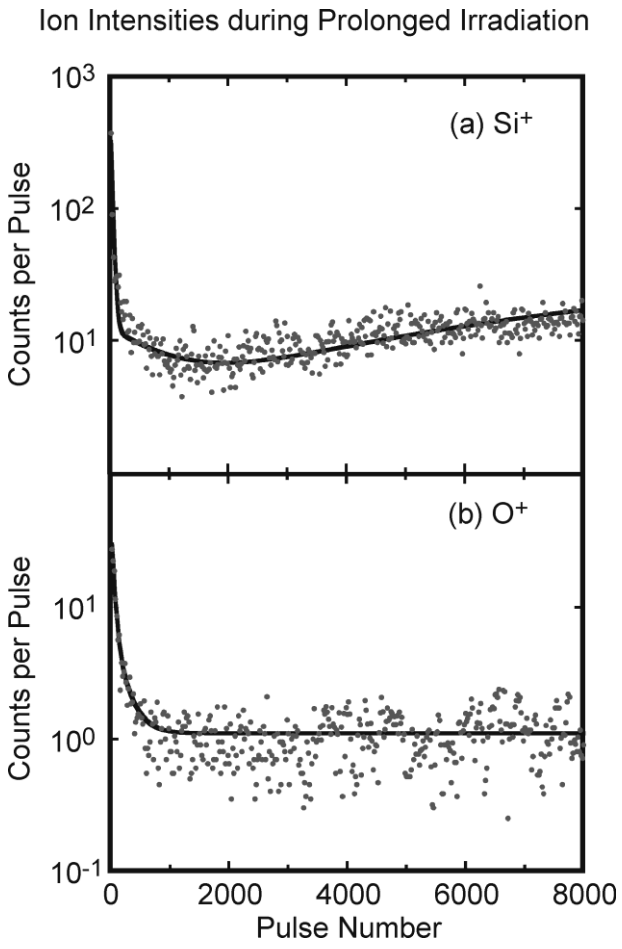

Fig. 5. (a) Si^+ and (b) O^+ intensities versus number of laser pulses from polished silica during exposure to 157 nm laser radiation at a fluence of 1.5 J/cm^2. The solid lines represent a least squares fit of the sum of an exponential decay and linear growth to the data.

The order-of-magnitude drop in both Si^+ and O^+ intensities during the first few hundred laser pulses suggests that a major share of the surface ion desorption sites responsible for emission—in this case, originally created by mechanical polishing—are gradually eliminated in the initial stages of 157-nm exposure. However, since the ion intensities remain well above background for several thousands of laser pulses, 157-nm exposure must also produce defects that yield emission. Thus laser irradiation both depletes *and* supplies ion desorption sites responsible for emission. In the case of Si^+, which shows the slow rise with pulse number, the rate of initial state production slightly exceeds destruction during prolonged exposure.

Despite the large changes in ion intensities with pulse number, the shapes of the Si^+ and O^+ time-of-flight signals are remarkably consistent. Figure 6 compares normalized time-of-flight signals for Si^+ and O^+ acquired after the first 200 laser pulses at 1.5 J/cm^2, and again after 9000 laser pulses (averaged over 200 laser pulses in each case). Although the time-of-flight signals broaden slightly during long exposures, the peak arrival times and mean kinetic energies are almost identical. Assuming that the ion kinetic energies reflect the local chemical and electrostatic environment of the ion desorption sites responsible for emission, we conclude that the ion emission sites produced by laser exposure (responsible for emission after several thousand pulses) are similar to the ion emission sites produced by mechanical treatments (responsible for emission during the early stages of exposure).

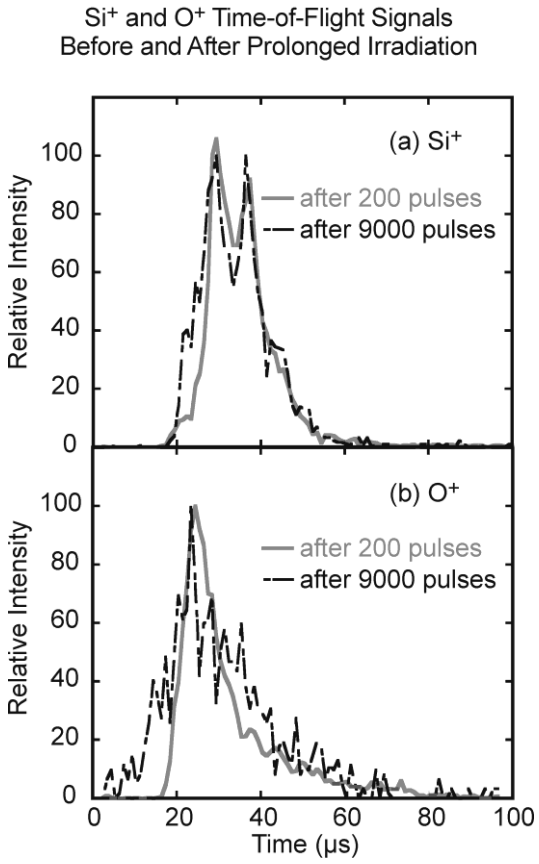

Fig. 6. (a) Si^+ and (b) O^+ time-of-flight signals acquired during irradiation of polished silica after 200 and after 9000 laser pulses at a fluence of 1.5 J/cm^2.

Laser-induced defects. We emphasize that to explain the observed initial *and* sustained ion emission from fused silica we must have defects and the laser must continue to make these defects. After an extensive analysis of a variety of fused silica defect structures, our best emission models involve surface Si-Si^+ and O-O^+ units. In the Si-Si^+ unit, a surface E' center provides a suitable chemical and electronic environment for the adsorption and release of Si^+. In the O-O^+ unit, a surface NBOHC provides a suitable environment for the adsorption and release of O^+. These Si-Si^+ and O-O^+ units can be produced by reactions involving E' centers and NBOHCs.

E' centers and NBOHCs are produced in significant numbers during 157 nm irradiation. Figure 7(a) shows the UV absorbance (calculated from the measured transmission through a 1-

mm thick sample) before and after exposure to 3000, 1.5 J/cm^2 pulses. The laser-generated absorption peaks near 212 nm and 257 nm correspond to absorption due to the E' center[27] and the NBOHC, respectively.[28] [We also observe a small peak at 615 nm (not shown) that is also associated with the NBOHC.] Photoelectron measurements by Zatsepin suggest that high densities of these centers are produced along the surface of electron irradiated fused silica.[32] Although 157-nm photons penetrate much further (about 400 μm at low fluences[33]), it is reasonable to assume that significant densities of E' centers and NBOHC are produced along the surface during laser irradiation as well.

We also observe minima in the spectra of light reflected from abraded fused silica that correspond roughly to the absorption maxima in Fig. 7(a). A typical diffuse reflection spectrum appears in the inset of Fig. 7(a). (A large feature due to Rayleigh scattering was removed from the reflection spectrum by subtracting a term proportional to λ^{-4}.) Thus we have spectroscopic evidence for the E' and the NBOHC on both mechanically treated samples and on samples that have undergone prolonged 157-nm irradiation. Further, the time-of-flight signals for Si^+ and O^+ are essentially identical for these two sets of samples. We expect that these two defects (the E' center and the NBOHC) play critical roles in both the initial Si^+ and O^+ emissions from mechanically treated silica and from the emissions much later, after extensive laser exposure.

The photoelectronic production of E' centers and NBOHCs in fused silica is often attributed to the nonradiative decay of self-trapped excitons.[34-36] This normally requires the absorption of two-photons, even at 157 nm. However, Hosono *et al*. have suggested that these defects can also be generated by single-photon absorption at disorder-related states associated with strained bonds.[37,38] To determine whether one- or two-photon absorption is responsible for the production of E' centers and NBOHC under the conditions of this work, the growth of the E' and NBOHC absorption peaks during 3000 pulse exposures was measured as a function of fluence. The resulting absorbance changes are plotted as a function of fluence on a log-log scale in Fig. 7(b). At fluences above 0.9 J/cm^2, where most of our positive ion emission measurements are made, the slope of the plot is nearly two; thus the dominant mechanism for the

production of E' and NBOHC defects at these fluences involves two-photon absorption. At lower fluences, however, the slope of the plot is very nearly one. The low fluence behavior is consistent with defect generation by single-photon absorption at disordered-related states associated with strained bonds as suggested by Hosono *et al*.[37] Such states can also enhance the cross section for two-photon absorption by many orders of magnitude by serving as intermediate (transient) states.

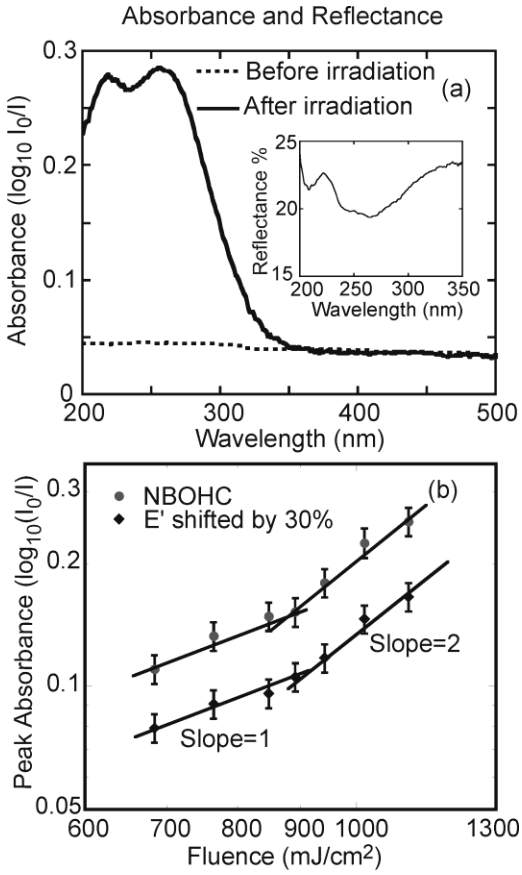

Fig. 7. (a) Room temperature absorption spectra of polished silica before (dotted line) and after (dark line) exposure to 3000, 1.5 J/cm^2 pulses of 157-nm radiation. The inset shows a diffuse reflectance spectrum acquired on an abraded silica surface; to emphasize the defect-related absorption, the contribution of Rayleigh scattering from the rough surface (proportional to λ^{-4}) was removed. (b) Log-log plot of the absorbance at 212 nm (E' center) and at 257 nm (NBOHC) as a function of fluence. The data for the 212 nm absorbance has been shifted upward for clarity. Line segments of slope one and slope two have been drawn through the data at low and high fluences, respectively.

As mentioned above, defect production by two-photon absorption in fused silica involves the nonradiative decay of the self-trapped exciton (STE).[36] To verify that such excitons are produced in our system, we monitored the STE luminescence of silica under 157-nm irradiation. At low temperatures, radiative decay proceeds in parallel with nonradiative decay,[17,39] and the resulting luminescence probes exciton production. A typical luminescence spectrum acquired at liquid nitrogen temperature from previously unexposed, polished silica sample is shown in Fig. 8(a). The spectrum is well described by the sum of three Gaussian peaks. The onset of spectra acquisition was delayed 100 μs after the laser pulse; at this delay the STE luminescence peaks near 2.5 eV, as described in the Experiment Section. A second peak at 2.8 eV corresponds to emission from the oxygen-deficiency center (II).[40] A third peak of uncertain origin is found at 3.0 eV.[41-43] No significant changes in either the width or the height of the 2.5 eV peak are observed over the first few thousand laser pulses, consistent with a signal that depends only on the number of electron hole pairs produced by band-gap excitations at any given laser fluence.

Figure 8(b) shows the fluence dependence of the area of the STE luminescence peak (determined from the curve fit) on a log-log plot. Over this limited fluence range ($0.3 < F < 0.5$ J/cm^2), the luminescence intensity varies with the square of the fluence, F (F^N where $N = 2.0 \pm 0.1$). The observation of STE luminescence and its second-order fluence dependence at fluences below 0.5 J/cm^2 confirm that electron hole pairs and self-trapped excitons are very likely generated at the fluences above 1 J/cm^2 employed in this study. Although the STE luminescence is quenched at room temperature (due to temperature dependent non-radiative decay), the relevant two-photon *absorption* process of creating electron hole pairs should not be strongly affected by temperature. Furthermore, the non-radiative production of E' centers and NBHOCs via STE decay still operates at room temperature. We emphasize that the continuous production of these defects during prolonged laser exposure would explain the sustained Si^+ and O^+ emissions which we observe.

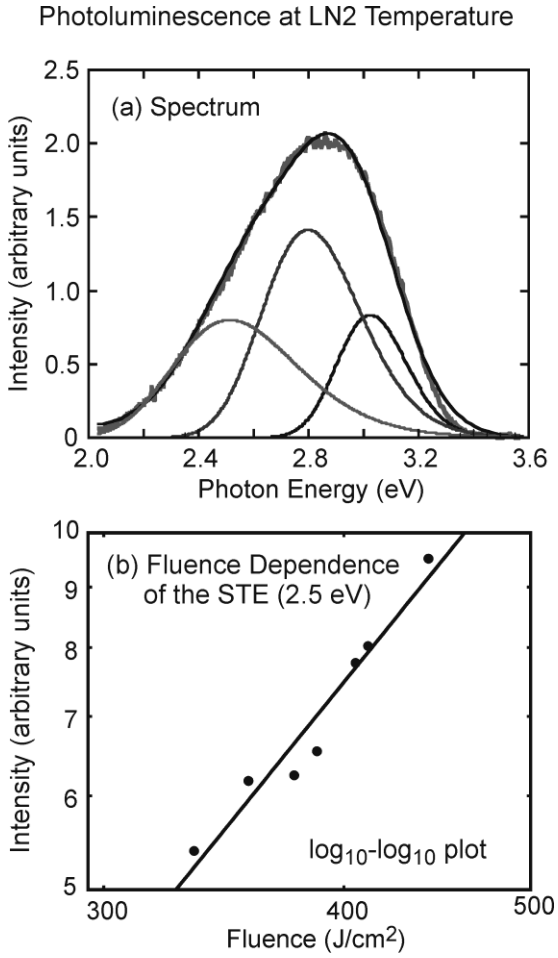

Fig. 8. (a) Uncorrected photoluminescence spectrum excited in polished silica at 80 K by two hundred, 450 mJ/cm^2 pulses of 157-nm radiation on a previously unexposed area of the sample. (b) Log-log plot of the intensity of the 2.5 eV peak versus laser fluence.

Reactions between E' centers produced by STE decay can produce surface Si-Si$^+$ units. These are the best candidate defect structures for Si$^+$ emission we have identified to date. Indicating intact bridging bonds by – and nonbridging bonds by •, the E' center becomes ≡Si• and the Si-Si$^+$ unit ≡Si-Si•••. Two E' centers can react to form an ODC(I) defect,[44] ≡Si–Si≡.[45] From the ODC(I), the Si-Si$^+$ unit can be formed by additional reactions with E' centers:

$$\equiv Si–Si\equiv \; + \; 3(\equiv Si\bullet) \; \rightarrow \; \equiv Si–Si\bullet\bullet\bullet \; + \; 3(\equiv Si–) \qquad (2)$$

Hartree-Fock calculations below indicate that the terminal Si atom in the surface ≡Si–Si••• unit is a good hole trap. Thus it is reasonable to expect that the terminal Si retains a net positive charge, consistent with subsequent emission as Si^+.

Reaction (2) consumes ODC(I) centers. ODC(I) centers are produced during prolonged 157-nm irradiation under the conditions of this work, as shown in the VUV absorption spectra of Fig. 9. The spectra of Fig. 9 were acquired before and after exposure to 30,000 157-nm pulses at 2.0 J/cm^2. The feature near 163 nm (7.6 eV) in the exposed material can be unambiguously assigned to the ODC(I),[45] also denoted the neutral oxygen vacancy. The long exposure required to produce the ODC(I) absorption is consistent with the known difficulty of producing this defect in wet silicas, and with the relatively high E' center densities required for E' + E' reactions.[41] This difficulty is also consistent with the gradual increase in Si^+ intensity only after relatively long exposures [2000 pulses at 1.5 J/cm^2 in Fig. 5(a)].

E' center reactions would naturally produce a variety of oxygen deficient centers, including the ODC(II). Although the structure of the ODC(II) is open to debate, it is closely related to the more abundant ODC(I) defect. The photoluminescence peak at 2.8 eV in Fig. 8(a) is indirect evidence for ODC(II) production during 157 nm exposure.

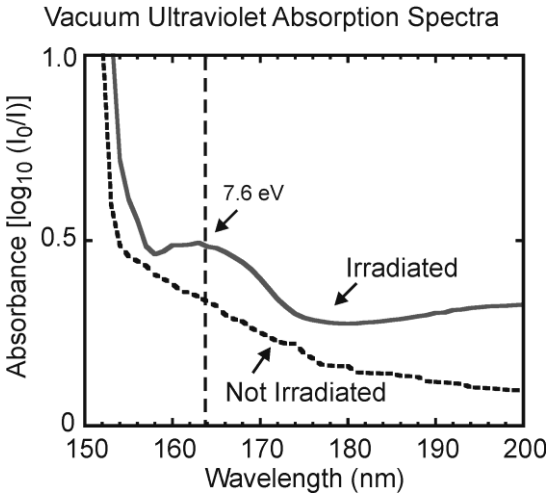

Fig. 9. Vacuum ultraviolet absorption spectrum of fused silica before and after 30,000 157-nm pulses at a fluence of 2.3 J/cm^2. The peak at 163 nm is due to the ODC(I) defect.

The proposed desorption site for O^+ emission is the surface peroxy radical, O–O•. Surface peroxy radicals are formed when atomic O (released by the dissociation of an NBOHC) reacts with a surface NBOHC.[46]

$$\equiv Si–O\bullet \quad + \quad O \quad \rightarrow \quad \equiv Si–O–O\bullet \qquad (3)$$

Hartree-Fock calculations described below show that the surface peroxy radical is a good hole trap. The terminal O retains a net positive charge consistent with subsequent emission as a positive ion. Both E' centers and NBOHCs appear to play important roles in ion emission from fused silica during 157-nm irradiation.

3.3 Hartree-Fock models of candidate surface defects and ion emission mechanism

We investigated the potential of several surface defects to yield ion emission by performing *ab-initio* Hartree-Fock calculations on silica clusters incorporating these defects. These calculations provide information on bonding, charge distributions, and possible excited states that constrain emission models. Many candidate clusters could be eliminated due to lack of stability or insufficient positive charge on the adion. Emission due to photoelectronic excitations normally involve transitions from bonding states to antibonding states localized near the emitted species; in addition, the energy difference between these states must be similar to the photon energy. Candidate clusters lacking these features were excluded from further consideration. Finally, ion emission requires that any antibonding final state persist until the ion escapes from the cluster; this rules out final states that lie in either the valence or conduction bands, where the large number of states with similar energy would favor rapid transitions to states that lack antibonding character.

Our search proceeded by designing a cluster incorporating a candidate defect structure; computing the corresponding equilibrium geometry and molecular orbitals; searching the band gap for orbitals with antibonding character localized on the candidate defect; and, if found, examining those orbitals 7.9 ± 1 eV below the candidate antibonding orbital for bonding orbitals also localized on the candidate defect. We emphasize that clusters satisfying all our criteria might still not yield emission. To verify emission would require currently difficult molecular dynamics simulations of highly excited systems. By virtue of their size, our clusters are also much less constrained that a semi-infinite silica solid—and this lack of constraint can allow for defect interactions (preventing emission in our cluster models) that would be unlikely on a physical silica surface. The models described below are but a first step in identifying the chemical and electronic properties that affect ion emission from a covalent material.

Proposed Si^+ emission mechanism. As mentioned above, the most promising structures for Si^+ emission that we have identified to date incorporate an Si-Si^+ unit. We show below that the energy levels in the Si-Si^+ unit are well situated for the absorption of a 7.9 eV photon. However, it is not clear that this excitation, by itself, will result in emission. We suggest that an electron must actually be *removed* from the excited state of the Si-Si^+ unit before emission takes place. The final state for the removed electron is likely a deep electron trap, such as a nearest-neighbor nonbridging oxygen.[47,48] The proposed sequence of events leading to emission is illustrated in Fig. 10.

The first step in the proposed emission process is the photoionization of a nearest neighbor electron trap [Fig. 10(b)]. Photoionization takes place by the absorption of a single, 7.9 eV photon, and provides a deep, unoccupied level to receive an electron from the Si-Si^+ unit. A second photon absorption event [Fig. 10(c)] excites a bonding-to-antibonding transition in the Si-Si^+ unit. This excited state then decays nonradiatively by electron transfer to the empty electron trap produced in Fig. 10(b). This electron transfer renders the Si-Si^+ unit unstable, and terminal Si^+ ion is ejected from the surface with several eV of kinetic energy [Fig. 10(d)]. We discuss

each of these steps below. The Si^+ charge estimates in Fig. 10 are used to estimate the kinetic energy of the ejected Si^+.

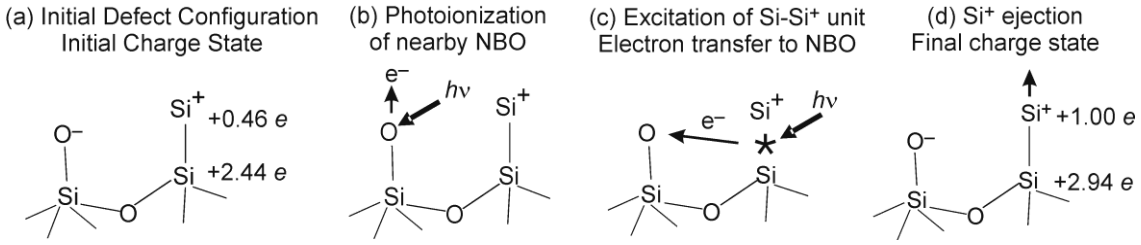

Fig. 10. (a) Initial defect configuration for the proposed Si^+ emission mechanism; the effective charges on the Si^+ ions (in the electrostatic approximation, calculated from Hartree-Fock electron densities) are noted to the right of each ion. (b) A nearest neighbor nonbridging oxygen (NBO) is photoionized by a 157-nm photon. (c) A second 157-nm photon excites the Si-Si^+ bond; the excitation decays by electron transfer to the unoccupied NBO state. (d) Repulsive electrostatic forces eject the terminal Si^+. The charge states on the Si^+ ions in (d) are estimated from those in (a), assuming that the emitted Si^+ carries a charge of +1 *e*, and that the electron transfer in (c) has removed one electron from the Si-Si^+ unit.

Electron Trap Photoionization. Recent theoretical work suggests that the surface nonbridging oxygen and E' centers are deep electron trap in high-OH silicas.[47,48] For the sake of definiteness, we focus on the nonbridging oxygen (NBO). The ability of the NBO at the surface to trap electrons is somewhat counterintuitive, as the same defect in the bulk is a good hole trap (the NBOHC). At the surface, the trapped electron is stabilized by lattice relaxations that are hindered in the bulk.[47] The surface NBO can be produced from surface Si-OH during 157-nm irradiation,[49] allowing for especially high trap densities. Other investigators have observed defect-related photoelectron emission from fused silica at photon energies as low as 4.5 eV;[32] in our calculations, the most easily ionized traps were identified as surface NBO's. We observe intense electron emission from silica during 157-nm irradiation, confirming that 7.9 eV photons can photoionize electron traps in amorphous silica under the conditions of this work.[15]

Excitation of the surface Si-Si^+ defect. Hartree-Fock calculations can provide information on the local structure and charge states of candidate structures. For instance, defects

yielding positive ion emission should show some tendency to trap positive charge. Photoexcitation processes are often much more likely to yield emission if the initial or final states are localized near the ion to be emitted. Further, the energy difference between the initial and final states must be similar to the photon energy—here 7.9 eV.

The most promising candidate defect structures for Si^+ emission identified to date incorporate a surface ≡Si-Si^+ unit, with a surface NBO in a nearest neighbor position. The ≡Si-Si^+ unit is equivalent to a Si^+ ion bonded to a surface E' center. A typical cluster was composed of 12 silicon ions and 28 oxygen ions, shown in Fig. 11(a). The cluster framework is provided by four, six-member rings connected in a tetrahedral fashion. The defects in this cluster render it metastable in the sense that its total energy would be reduced by reactions between the terminal Si^+ and nearby NBOs. Since almost all our cluster atoms lie on the surface, they are much less constrained than surface atoms on a semi-infinite bulk. To prevent these reactions, additional constraint was provided by connecting the Si-Si^+ unit to three four-member rings; this structure is geometrically equivalent to a six-member ring with an Si-Si^+ unit bonded to three members of the six-member ring. A diagram of the local geometry of the Si-Si^+ unit relative to the surrounding six-member ring is shown in the inset of Fig. 11(a). Using the simple STO-3G basis also hindered energy-minimizing reactions with nearby NBOs. All the NBOs in the cluster except the nearest-neighbor electron trap were terminated with hydrogen. The cluster was assigned a net charge of +1 *e*, consistent with a neutral cluster with one positive adion. The calculated equilibrium geometry of the cluster is shown in Fig. 11(a).

Significantly, the equilibrium geometry calculations indicate that the cluster, including the adion, is bound and that the adion remains positively charged. Mulliken charge analysis shows over half of the net positive charge of the cluster is localized on the adion. The charge on the underlying Si ion is also net positive. Although the Si-Si^+ pair is bound, the net positive charge on the two silicon ions helps account for ion, as opposed to neutral, emission.

In Figs. 11(b) and 11(c), we show surfaces of constant electron probability amplitude for candidate initial and final states under 7.9 eV excitation. [The incorporation of the un-terminated

NBO (electron trap) introduces an unpaired spin. Unrestricted Hartree-Fock results distinguish between electron spin states with spins parallel and anti-parallel to the net cluster spin, denoted α and β states, respectively.] The candidate initial state is two levels below the highest occupied molecular orbital (the β-HOMO-2 state), and the candidate final state is two levels above the lowest unoccupied molecular orbital (the β-LUMO+2 state). To compare the energy required to produce the β-LUMO+2 final state with the laser photon energy, the calculated (uncorrected) β molecular orbital energies for the cluster in Fig. 11 were tabulated. The results are shown in Fig. 12. The clusters of energy levels near –6 eV and +4 eV correspond to the valence and conduction bands of the bulk silica, respectively. The difference between the highest level in the lower band and the lowest level in the upper band is 9.57 eV—about 7% higher than the experimental band gap of 8.9 eV. This overestimate is consistent with the failure of Hartree-Fock methods to properly account for electron correlation.[50] A reasonable correction to the calculated energy differences can be made by reducing all the calculated energies by the same 7% required to bring the calculated and experimental band gaps into agreement. Decreasing the calculated energy difference between the bonding HOMO-1,2 pair and the antibonding LUMO+2 state (8.3 eV) by 7% yields an energy difference of 7.7 eV. Thus the corresponding transition should be efficiently excited by 7.9 eV photons.

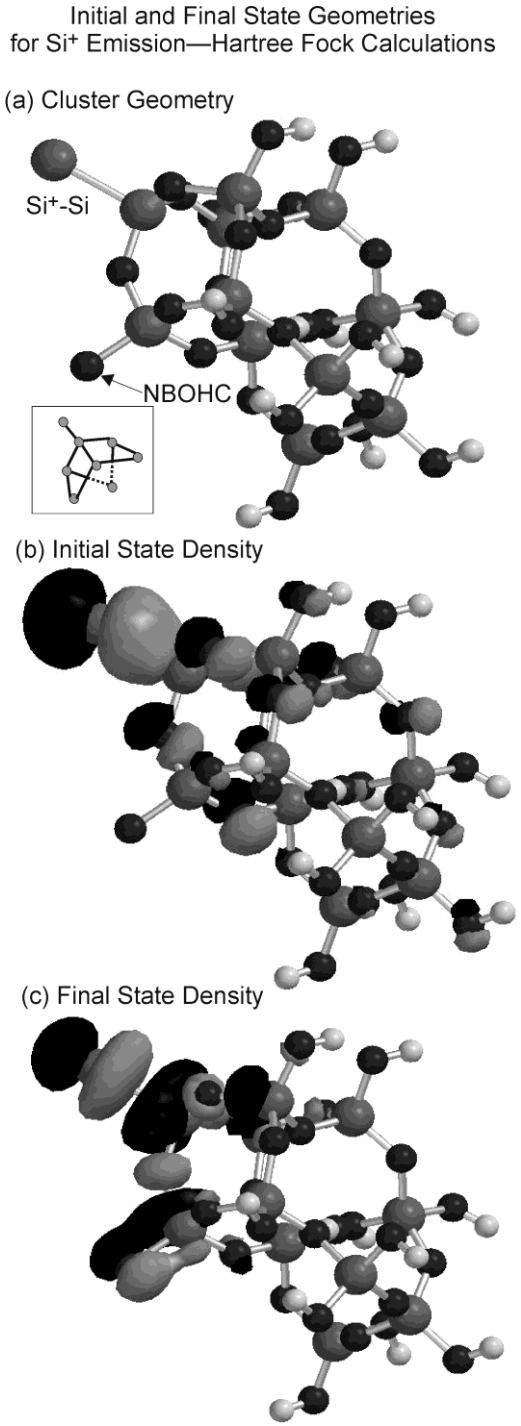

Fig. 11. Results of Hartree-Fock calculations for a $Si_{12}O_{16}(OH)_{12}^{+}$ cluster with a silicon adion attached to a silicon dangling bond. (a) Equilibrium geometry. The inset shows the local geometry of the Si-Si^{+}, which is bonded to three corners of a six member silicate ring. Surfaces of constant electron density for (b) the β-HOMO-2 orbital, the proposed initial state for ion emission; and (c) the β-LUMO+2 orbital, the proposed final state for ion emission. The surface darkness indicates sign of the wave function.

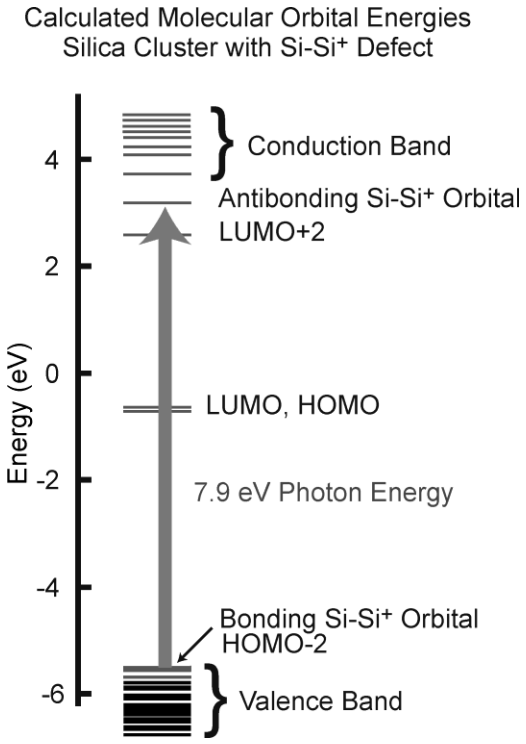

Fig. 12. Schematic band diagram corresponding to the silica cluster in Fig. 11(a). The length of the gray arrow corresponds to the 7.9-eV photon energy; this energy is sufficient to excite the transition from bonding to antibonding states localized on the $Si\text{-}Si^+$ unit.

The calculated 7.7 eV transition energy in the $Si\text{-}Si^+$ unit is similar to experimental excitation energies of the Si-Si bond in other compounds. For instance, Hosono *et al.* attribute an absorption band centered at 7.6 eV in fused silica to an Si-Si defect.[51] Gas-phase Si_2H_8 also absorbs near 7.6 eV, where the initial state has been assigned to a sigma Si-Si bond.[52] Since changing the identity of other species bound to the Si-Si unit apparently has little effect on the energy of the absorption, we expect that both the initial and final states are localized near the Si-Si bond. Thus, our 7.9 eV photons are likely suitable for the excitation from bonding to antibonding orbitals on the proposed $Si\text{-}Si^+$ defect.

Electron transfer to trap. The node between the two silicon ions in the $Si\text{-}Si^+$ unit of Fig. 11(c) indicates antibonding character. Menzel, Gomer,[12] and Redhead[13] proposed that

electron-stimulated desorption (ESD) of adsorbed gases on metal surfaces takes place by similar bonding-to-antibonding transitions. However, our experimental evidence suggests that a single bonding-to-antibonding transition is insufficient to yield Si^+ emission in this system. If single photon absorption yielded emission, we would expect the Si^+ intensity to vary with the first power of fluence: the observed fluence dependence is closer to the square of fluence. Further, emission due to a single 7.9 eV excitation would be inconsistent with conservation of energy (given the 8-9 eV *average* kinetic energy of the emitted Si^+).

An additional excitation would be required for Si^+ emission if the excited state of the Si-Si^+ unit is weakly bound, or if the excited state decays radiatively. Hartree-Fock calculations on the $Si(SiH_3)^+$ ion—a small molecule analog of the surface Si-Si^+ unit—suggest (but do not prove) that the LUMO+2 is indeed weakly bound. Conversely, the $Si(SiH_3)^{2+}$ ion, formed by removing a second electron, spontaneously dissociates. Therefore we suggest that removing an electron from the Si-Si^+ unit is required for emission. For instance, the LUMO+2 excitation could decay by electron transfer to a nearby (empty) electron trap.

Significantly, the wave function density for candidate final state in Fig. 11(c) is shared between the Si-Si^+ unit and the nearby empty electron trap. This excitation therefore reduces the electron density on the Si-Si^+ unit and favors an increase in the Si-Si^+ bond length. Electron transfer to the NBO would be a natural result. Coupled quantum mechanics and molecular dynamics simulations would be required to establish whether the Si-Si^+ bond length subsequently increases in an unstable fashion to yield emission. However, emission appears to be a reasonable expectation. If the electron trap must be emptied by a separate excitation, emission would require two photons and thus vary with the second power of laser fluence.

Si^+ kinetic energy. In principle, both electrostatic and antibonding chemical forces contribute to the ion kinetic energy. We focus here on changes in electrostatic potential energy. (The potential contribution of antibonding chemical forces is discussed below.) Initially, the terminal Si^+ is bound to the cluster. To remove it, an energy equal to the binding energy, *BE*, must be supplied. The Appendix describes an estimate of *BE* appropriate to the case of rapid

removal, where the rest of the ions in the cluster remain fixed in their initial positions. We find that $BE \approx 3.7$ eV. The laser-induced excitations described above and in Fig. 10 increase the potential energy of the ion by an amount ΔPE. If $\Delta PE > BE$, the potential energy of the Si^+ adion is sufficient for emission. Further, if all the excess potential energy is converted to kinetic energy (consistent with rapid removal), the final ion kinetic energy, *KE*, is given by:

$$KE = \Delta PE - BE \quad . \tag{4}$$

In the scenario illustrated in Fig. 10, ΔPE includes changes in the electrostatic potential energy of the Si^+ adion due to the removal of an electron from the Si-Si^+ unit and the changes within the Si-Si^+ unit necessary to yield a +1 *e* charge on the departing adion. (We neglect potential charge exchange with the rest of the cluster.) The charge on the neighboring NBO is unchanged by these two excitations, as the electron removed by the first excitation is replaced by electron transfer from the Si-Si^+ unit (the second excitation). The electrostatic contribution to ΔPE is then

$$\Delta PE = \left.\frac{q_{adion} q_{trap}}{4\pi\varepsilon_0 r_{trap}}\right|_{after\ excitation} - \left.\frac{q_{adion} q_{trap}}{4\pi\varepsilon_0 r_{trap}}\right|_{before\ excitation} \tag{5}$$

where q_{adion} is the charge on the Si^+ adion, q_{trap} is the charge on the underlying Si (which serves as a surface electron trap or adsorption site), and r_{trap} is the length of the Si-Si^+ bond.

We take q_{adion} and q_{trap} before excitation from Hartree-Fock "electrostatic" charge estimates. In electrostatic charge estimates, the cluster is treated as a lattice of point charges located at the equilibrium atomic positions. The magnitude and sign of each charge is chosen to reproduce (as well as possible) the electrostatic potential distribution calculated from the Hartree-Fock charge densities.[50] Electrostatic charge values often differ significantly from those calculated from the contribution of each atomic basis function to the occupied molecular orbitals.

For the purpose of describing the electrostatic environment of the cluster ions, electrostatic charge values are preferred. Our Hartree-Fock calculations yield q_{adion} = +0.46 *e*, q_{trap} = +2.44 *e*, and r_{trap} = 2.37 Å.

The charge values after excitation are estimated by assuming that the Si-Si^+ unit loses an electron in the excitation process, and that the final charge on the adion is +1 *e*. With these assumptions, q_{adion} = +1.0 *e* and q_{trap} = +2.94 *e*. Electron transfer from the Si-Si^+ unit is presumably very rapid, so that r_{trap} is unchanged. With these values, ΔPE = 17.9 – 6.8 = 11.1 eV, and the final ion kinetic energy *KE* = 7.4 eV. While this is somewhat less than the observed 8-9 eV Si^+ kinetic energies, the agreement is plausible given the uncertainties in the model and the calculated parameters.

The energy estimate above neglects atomic relaxation (which would reduce the ion kinetic energies) and antibonding chemical forces (which would increase the ion kinetic energies). The neglect of relaxation during ion emission from ionic solids is rationalized in Ref. 17. In a number of ionic materials, relaxation is frustrated by the close packed nature of their lattices. Even in more open lattices, relaxation processes that require the collective motion of several atoms will probably be limited on the time scales of a typical ion emission event (tens of picoseconds). As noted above, molecular dynamics simulations are required to address this issue.

Antibonding chemical forces are also neglected in Eq. (5). These forces arise from the contribution of electron kinetic energy to the total cluster energy. In the simplest diatomic molecule, H_2, the electron kinetic energy can be estimated from the derivative of total energy with respect to atomic separation.[53] In H_2, the kinetic energies of the (ground) $^1\Sigma_g^+$ and $^3\Sigma_u^+$ states evaluated at the equilibrium atomic separation for the $^1\Sigma_g^+$ state differ by only 0.2 eV; in contrast, the electron kinetic energy of the $^1\Pi_u$ state at the same atomic separation is several eV.[54] Thus the magnitude of kinetic energy effects is a strong function of the states involved in the excitation. Given the available computational resources, we are not able to estimate the

contribution of antibonding chemical forces to the ion kinetic energy in this system. This would presumably require coupled quantum mechanics and molecular dynamics simulations.

Surface O-O$^+$ defect. Our efforts to model the O^+ emission precursor were not entirely successful. The strongly nonlinear dependence of the O^+ intensity on fluence implies the involvement of about five photon absorption events per emitted ion. It is difficult to incorporate this many absorption events into a simple model.

Any surface absorption site for O^+ emission must have a strong affinity for positive charge (holes) in order to overcome the normally negative charge on the oxygen atom. The peroxy defect (≡Si-O-O•) is an important hole trap in silica[55] and is readily formed by the reaction between atomic oxygen and a NBOHC. Hartree-Fock calculations (discussed below) show that the terminal oxygen on a surface peroxy defect (≡Si-O-O•) retains a positive charge, suggesting that O^+ can be emitted by a suitable sequence of electronic transitions. We note that the fracture of fused silica in vacuum produces intense O^+ emissions;[56] thus we expect mechanically generated O^+ on the silica surface. As discussed above, peroxy defects are also produced in the bulk by 157-nm laser radiation,[57,58] consistent with the sustained emission of O^+ during prolonged irradiation in Fig. 5.

Figure 13(a) shows the Hartree-Fock equilibrium geometry of a $Si_{10}O_{14}(OH)_{14}^+$ cluster incorporating a surface peroxy unit (O-O$^+$). The spin multiplicity of the ground state is four, consistent with the triplet ground state of the oxygen molecule plus an additional unpaired spin within the cluster. Spin states parallel and antiparallel to the net cluster spin are designated α and β states, respectively. Surfaces of constant wave function density for initial and final states for excitations that might lead to emission are shown in Figs. 13(b) and 13(c).

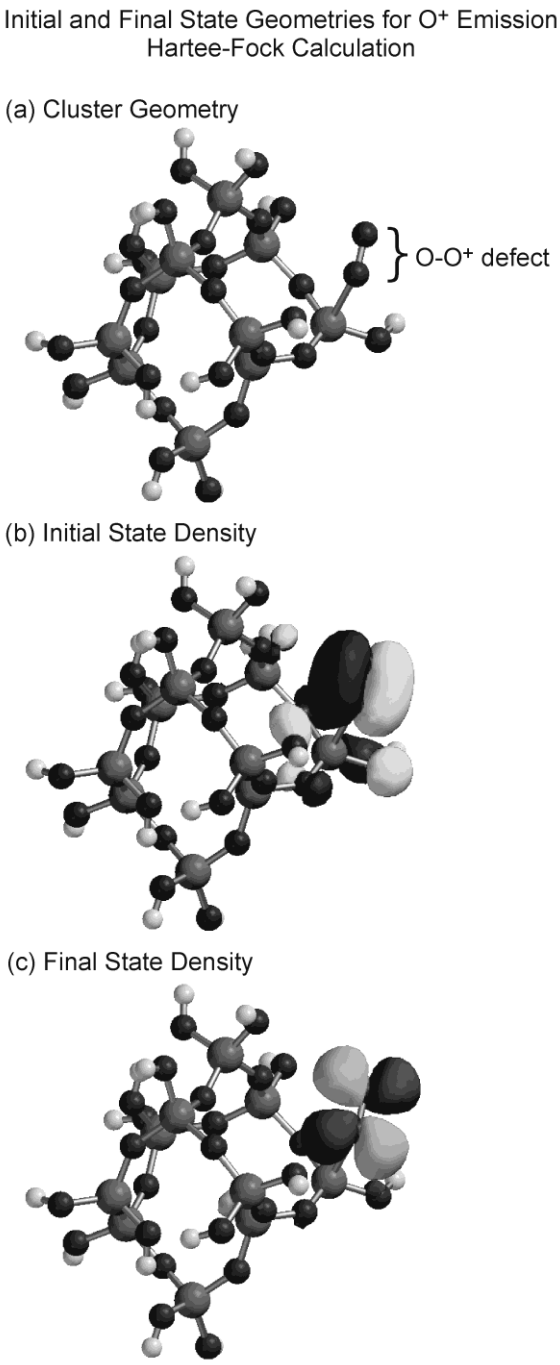

Fig. 13. Results of Hartree-Fock calculations for a $Si_{10}O_{14}(OH)_{14}^{+}$ cluster with a peroxy group attached to a silicon dangling bond. (a) Equilibrium geometry. Surfaces of constant wave function density for (b) the β-HOMO-51 orbital, one of the proposed initial states for ion emission; and (c) the β-LUMO+2 orbital, the proposed final state for ion emission. The surface darkness indicates the sign of wave function.

The terminal oxygen on the $O\text{-}O^+$ unit in Fig. 12 exhibits a net positive charge of about +0.2 *e*. Although the magnitude of this charge is much less than the +1.0 *e* of the emitted ions, it is comfortably positive. We assume that the net charge on the terminal O^+ can be increased by electron transfer to nearby electron traps, as in the case of Si^+ emission from the $Si\text{-}Si^+$ unit. The photoexcitations necessary to photoionize these nearby electron traps and to transfer an electron from the $O\text{-}O^+$ unit to an empty trap would contribute to the high-order fluence dependence of the O^+ signal.

The bonding states associated with the surface peroxy unit in Fig. 13 lie deep in the valence band. The bonding orbital in Fig. 13(b) (β-HOMO-51) is one of several similar orbitals located about 3 eV *below* the top of the valence band. The β-LUMO+2 orbital in Fig. 13(c) is strongly antibonding and is well localized on the $O\text{-}O^+$ unit. Excitations from the β-HOMO-51 orbital to the β-LUMO+2 orbital could contribute to O^+ emission. Pauli exclusion forces associated with antibonding chemical states in the $O\text{-}O^+$ defect (which we ignore in electrostatic models of emission) would contribute to the kinetic energy of the ejected O^+.

To compare the energies required for the bonding-to-antibonding transitions in the surface peroxy unit, the molecular orbital energies for the cluster of Fig. 13 were tabulated. The energies for the β molecular orbitals in the vicinity of the band gap are plotted in Fig. 14. The energy difference between the bonding and antibonding orbitals of Fig. 14 is about 9 eV—well above the photon energy. Transitions between these two states would likely require a sequence of single-photon excitations, possibly involving nearby defects. A similar sequence of excitations has been invoked to explain the high-order (up to sixth order) fluence dependence of ion intensities during UV irradiation of ionic materials, including MgO and $NaNO_3$.[7] The high cross section for two-photon absorption in fused silica at 157-nm has also been attributed to a sequence of single photon absorption events involving defect related intermediate states.[38]

The high-order fluence dependence of the O^+ signal and the lack of a simple path from 7.9 eV excitations to O^+ emission complicate the task of building a more complete model of the emission process. In particular, attempts to estimate the binding energy were not successful.

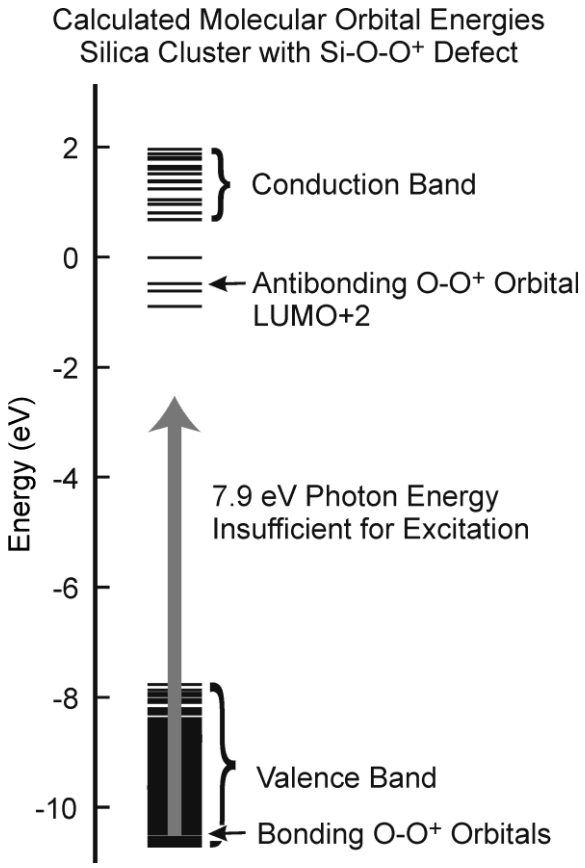

Fig. 14. Schematic band diagram corresponding to the silica cluster of Fig. 13(a), showing the β-manifold energy levels. The bonding states for the $O\text{-}O^+$ unit lie deep within the valence band. The length of the gray arrow corresponds to the 7.9 eV photon energy; this energy is insufficient for exciting a transition from bonding to antibonding states associated with the peroxy group. Multiple excitations, possibly involving intermediate states, would be required for O^+ emission.

4. Summary and Conclusions

Laser-induced positive ion emission has been observed from a number of wide bandgap, ionic materials.[7,9-11] These ions often have kinetic energies well in excess of the photon energy. A good account of the ion kinetic energies and the fluence dependences of the ion intensities are provided by electrostatic models that incorporate:

(1) electron traps near (but not adjacent to) an adsorbed positive ion, whose photoionization increases the electrostatic potential energy of the adion, and

(2) a nearest-neighbor electron trap, whose photoionization releases the ion into vacuum.

As long as the nearest-neighbor electron trap remains occupied, the trapped charge produces a local potential energy minimum at the adion site and emission is prevented. After the ionization of one or more nearby electron traps, ion emission is triggered by the ionization of the nearest-neighbor trap.[7]

Here we have shown that energetic positive ions (Si^+ and O^+) are emitted from *covalently* bonded fused silica during 157-nm irradiation. Like the ion emissions from the more ionic materials, these ions are:

(1) energetic (> 8 eV for Si^+ and about 4 eV for O^+);

(2) their intensities are strongly nonlinear functions of fluence; and

(3) their intensities are increased dramatically by treatments that increase the density of surface point defects. Conversely, their intensities are reduced by treatments that reduce the density of surface point defects.

The high Si^+ kinetic energy and nonlinear fluence dependence require the involvement of more than a single photon excitation event. We emphasize that these excitations involve sequential, single-photon absorption (i.e., multiple photon absorption), as opposed to a single multiphoton absorption event.

A reasonably complete account of the Si^+ kinetic energy can be constructed with input from Hartree-Fock calculations on the surface Si-Si^+ site. Although the Si-Si^+ unit shows a bonding-to-antibonding transition that is well situated for excitation by 7.9 eV photons, this excitation alone is not sufficient for Si^+ emission. Emission also requires (1) a nearby, empty electron trap (produced by a single-photon photoexcitation), and (2) electron transfer from the Si-Si^+ unit to the resulting empty nearby trap (produced by a single photon, excitation of the Si-Si^+ bonding to antibonding transition, which relaxes by electron transfer to the nearby empty

trap). The Si^+ adion remains bound in the Si-Si^+ unit until the Si-Si^+ antibonding state is excited and decays by transfer to the nearby empty trap.

The ion desorption sites required for ion emission can be produced by mechanical treatments, including abrasion and indentation. Laser absorption at 157-nm produces similar sites by both one- and two-photon processes. Thus ion emission can be sustained at modest levels even after thousands of laser pulses. Mishandling and polishing errors can produce similar defects during the preparation of optical components. Since ions can be detected with near-unity efficiencies, ion emission is a sensitive probe of flaws and defects on silica components for critical optical applications.

The covalent nature of the Si-O bond in silica argues against a purely electrostatic emission mechanism for ion emission. The classic example of emission in covalent systems is electron-stimulated emission from adsorbate-covered metal surfaces.[12,13] These emissions are attributed to the production of chemical states whose antibonding character is sufficient to yield emission (the Menzel-Gomer-Redhead mechanism).

Important details of the ion emission process from fused silica remain unresolved. These include the contributions of antibonding chemical forces and lattice relaxation to the ion kinetic energies. The factors controlling the width of the ion kinetic energy distributions are also not clear. Some of the required calculations are beyond the current state of the art. The close relation between ion emission and atomic-level damage processes provides a powerful motive for developing improved models of excitation and lattice dynamics. As a check on chemical models, the high sensitivity with which ions can be detected is an important advantage. Experimental studies of laser-induce damage often require higher fluences, higher defect densities, and even more complex excitations.

Acknowledgments

This work was supported by the U.S. Department of Energy under Grant DE-FG02-04ER-15618. One of us acknowledges summer support from the Washington State University College of Sciences.

Appendix: Binding Energy Calculation

This binding energy *BE* of the Si^+ ion in the ground state cluster in Fig. 10(a) was estimated from Hartree-Fock energy calculations on clusters that represent the absorption site before and after emission. The potential energy of the cluster before emission [$E_{Si_{12}O_{16}(OH)_{12}^+}$] is taken directly from calculations on the cluster of Fig. 11(a). The potential energy after emission (neglecting kinetic energies) is the sum of the energy of an isolated Si^+ ion (E_{Si^+}) and the energy of the neutral $Si_{11}O_{16}(OH)_{12}$ cluster with adion removed [$E_{Si_{11}O_{16}(OH)_{12}}$]; the latter energy was calculated with atomic positions fixed, as most atomic motions along the surface are constrained by the underlying bulk. Then the binding energy *BE* becomes

$$BE = E_{Si_{12}O_{16}(OH)_{12}^+} - [E_{Si_{11}O_{16}(OH)_{12}} + E_{Si^+}] \quad (3)$$

This procedure yields $BE \approx 3.7$ eV.

References

1 K. Saito and A. J. Ikushima, "Absorption edge in silica glass," Phys. Rev. B **62,** 8584-8587 (2000).

2 J. Ihlemann, S. Müller, S. Puschmann, S. Schäfer, M. Wei, J. Li, and P. R. Herman, "Fabrication of submicron gratings in fused silica by F_2-laser ablation," Appl. Phys. A **76,** 751-753 (2003).

[3] D. Schäfer, J. Ihlemann, G. Marowsky, and P. R. Herman, "F_2-laser ablation patterning of dielectric layers," Appl. Phys. A **72,** 377-379 (2001).

[4] P. R. Herman, R. S. Marjoribanks, A. Oettl, K. Chen, I. Konovalov, and S. Ness, "Laser shaping of photonic materials: Deep-ultraviolet and ultrafast lasers," Appl. Surf. Sci. **154-155,** 577-586 (2000).

[5] E. Matthias, H. B. Nielsen, J. Reif, A. Rosen, and E. Westin, "Multiphoton induced desorption of positive ions from barium fluoride," J. Vac. Sci. Technol. B **5,** 1415-1422 (1987).

[6] L. L. Chase, A. V. Hamza, and H. W. Lee, in *Laser Ablation—Mechanisms and Applications*, edited by J. C. Miller and R. F. H. Jr. (Springer-Verlag, Berlin, 1991), p. 193-202.

[7] D. R. Ermer, J.-J. Shin, S. C. Langford, K. W. Hipps, and J. T. Dickinson, "Interaction of wide bandgap single crystals with 248 nm excimer laser radiation. IV. Positive ion emission from MgO and $NaNO_3$," J. Appl. Phys. **80,** 6452-6466 (1996).

[8] Y. Kawaguchi, M. L. Dawes, S. C. Langford, and J. T. Dickinson, "Interaction of wide band gap single crystals with 248 nm excimer laser irradiation: VI. The influence of thermal pre-treatment on laser desorption of positive ions from a water-containing ionic crystal ($CaHPO_4 \cdot 2H_2O$)," J. Appl. Phys. **88,** 647-656 (2000).

[9] J. T. Dickinson, S. C. Langford, J. J. Shin, and D. L. Doering, "Positive ion emission from excimer laser excited MgO surfaces," Phys. Rev. Lett. **73,** 2630-2633 (1994).

[10] J. J. Shin, M.-W. Kim, and J. T. Dickinson, "Effect of tribological wear on UV laser interactions with single crystal $NaNO_3$ and $CaCO_3$," J. Appl. Phys. **80,** 7065-7072 (1996).

[11] M. Dawes, S. C. Langford, and J. T. Dickinson, "Laser desorption of positive ions from a model hydrated inorganic crystal ($CaHPO_4 \cdot 2H_2O$) by 248 nm irradiation," Appl. Surf. Sci. **127-129,** 81-87 (1998).

[12] D. Menzel and R. Gomer, "Desorption from metal surfaces by low-energy electrons," J. Phys. Chem. **41,** 3311-3328 (1964).

[13] P. A. Redhead, "Interaction of slow electrons with chemisorbed oxygen," Can. J. Phys. **42,** 886-905 (1964).

[14] S. R. George, S. C. Langford, and J. T. Dickinson, "Interaction of vacuum ultraviolet excimer laser radiation with fused silica: II. Neutral atom and molecule emission," J. Appl. Phys. **107,** 033108 (11) (2010).

[15] S. R. George, S. C. Langford, and J. T. Dickinson, "Interaction of vacuum ultraviolet excimer laser radiation with fused silica: III. Negative ion formation," J. Appl. Phys. **107,** 033109 (10) (2010).

[16] A. J. Fisher, W. Hayes, and A. M. Stoneham, "Structure of the self-trapped exciton in quartz," Phys. Rev. Lett. **64,** 2667 (1990).

[17] T. Tanaka, T. Eshita, K. Tanimura, and N. Itoh, "Transient optical absorption and luminescence centers in amorphous SiO_2 induced by electron excitation," Cryst. Lattice Defects Amorph. Mater. **11,** 221-228 (1985).

[18] K. Tanimura, C. Itho, and I. Noriaki, "Transient optical obsorption and luminescence induced by band-to-band excitation in amorphous SiO_2," J. Phys. C **21,** 1869-1876 (1988).

[19] A. L. Shluger, "Model of the triplet self-trapped exciton in crystalline SiO2," J. Phys. C **21,** L431-L434 (1988).

[20] CRC, *CRC Handbook of Chemistry and Physics*, 85 ed. (CRC Press LLC, 2004).

[21] C. Bandis, S. C. Langford, and J. T. Dickinson, "Desorption of positive ions from ionic crystals accompanying 248 nm laser irradiation," Appl. Phys. Lett. **76,** 421-423 (2000).

[22] K. H. Nwe, S. C. Langford, and J. T. Dickinson, "Interaction of wide-band-gap single crystals with 248-nm excimer laser irradiation. IX. Photo-induced atomic desorption from cleaved NaCl(100) surfaces," J. Appl. Phys. **98,** 013506 (2005).

[23] J. T. Dickinson, J. J. Shin, and S. C. Langford, "The role of defects in laser induced positive ion emission from ionic crystals," Appl. Surf. Sci. **96-98,** 316-320 (1996).

[24] S. Kano, S. C. Langford, and J. T. Dickinson, "Interaction of wide band gap single crystals with 248 nm excimer laser irradiation. VIII. Laser desorption of molecular ions from MgO," J. Appl. Phys. **89,** 2950-2957 (2001).

[25] K. H. Nwe, S. C. Langford, and J. T. Dickinson, "The effect of water vapor and bulk temperature on positive ion emission from wide bandgap single crystals during exposure to 248 nm excimer laser radiation," Appl. Surf. Sci. **197-198,** 83-89 (2002).

[26] G. Hochstrasser and J. F. Antonini, "Surface states of pristine silica surfaces: I. ESR studies of E_S' dangling bonds and of CO_2^- adsorbed radicals," Surf. Sci. **32,** 644-664 (1972).

[27] D. L. Griscom, "Defect structures in glasses: Some outstanding questions in regard to vitreous silica," J. Non-Cryst. Solids **73,** 51-77 (1985).

[28] L. Skuja, K. Tanimura, and N. Itoh, "Correlation between the radiation-induced intrinsic 4.8 eV optical absorption and 1.9 eV photoluminescence bands in glassy SiO_2," J. Appl. Phys. **80,** 3518-3525 (1996).

[29] K. H. Nwe, S. C. Langford, and J. T. Dickinson, "Interaction of wide-band-gap single crystals with 248-nm excimer laser irradiation. X. Laser-induced near-surface absorption in single-crystal NaCl," J. Appl. Phys. **97,** 043501 (2005).

[30] S. Gogoll, E. Stenzel, H. Johansen, M. Reichling, and E. Matthias, "Laser-damage of cleaved and polished CaF_2 at 248 nm," Nucl. Instrum. Meth. Phys. Res. B **116,** 279-283 (1996).

[31] E. Stenzel, S. Gogoll, J. Sils, M. Huisinga, H. Johansen, G. Kästner, M. Reichling, and E. Matthias, "Laser damage of alkaline-earth fluorides at 248 nm and the influence of polishing grades," Appl. Surf. Sci. **109-110,** 162 (1997).

[32] A. F. Zatsepin, "Electron emission from excited states of E′ centers in SiO_2," J. Non-Cryst. Solids **353,** 590-593 (2007).

[33] J. Zhang, P. R. Herman, C. Lauer, K. P. Chen, and M. Wei, in *Laser Applications in Microelectronic and Optoelectronic Manufacturing VI*; *Vol. 4274*, edited by M. C.

Gower, H. Helvajian, K. Sugioka, and J. J. Dubowski (SPIE, Belleview, WA, 2001), p. 125-132.

[34] K. Arai, H. Imai, H. Hosono, Y. Abe, and H. Imagawa, "Two-photon processes in defect formation by excimer lasers in synthetic silica glass " Appl. Phys. Lett. **53,** 1891-1893 (1988).

[35] T. E. Tsai, D. L. Griscom, and E. J. Friebele, "Mechanism of intrinsic Si E'-center photogeneration in high-purity silica," Phys. Rev. Lett. **61,** 444-446 (1988).

[36] T. E. Tsai and D. L. Griscom, "Experimental evidence for excitonic mechanism of defect generation in high-purity silica," Phys. Rev. Lett. **67,** 2517-2520 (1991).

[37] H. Hosono, Y. Ikuta, T. Kinoshita, K. Kajihara, and M. Hirano, "Physical disorder and optical properties in the vacuum ultraviolet region of amorphous SiO_2," Phys. Rev. Lett. **87,** 175501-1-4 (2001).

[38] K. Kajihara, Y. Ikuta, M. Hirano, and H. Hosono, "Power dependence of defect formation in SiO_2 glass by F_2 laser irradiation," Appl. Phys. Lett. **81,** 3164-3166 (2002).

[39] J. H. Stathis and M. A. Kastner, "Time-resolved photoluminescence in amorphous silicon dioxide," Phys. Rev. B **35,** 2972-2979 (1987).

[40] L. Skuja, "Direct singlet-to-triplet optical absorption and luminescence excitation band of the twofold-coordinated silicon center in oxygen-deficient glassy SiO_2," J. Non-Cryst. Solids **167,** 229-238 (1994).

[41] H. Nishikawa, T. Shiroyama, R. Nakamura, Y. Ohki, K. Nagasawa, and Y. Hama, "Photoluminescence from defect centers in high purity silica glasses observed under 7.9 eV excitation," Phys. Rev. B **45,** 586-591 (1992).

[42] Y. Sakurai, "The 3.1 eV photoluminescence band in oxygen-deficient silica glass," J. Non-Cryst. Solids **271,** 218-223 (2000).

[43] M. Ishii, T. Yoshida, and K. Sakurai, "X-ray excited 3.2 eV luminescence from amorphous silica: Radiative electron relaxation through an unidentified centre and its thermal switching," Journal of Physics: Condensed Matter **20,** 255249 (2008).

[44] L. Skuja, "Optically active oxygen-deficiency-related centers in amorphous silicon dioxide," J. Non-Cryst. Solids **239,** 16-48 (1998).

[45] R. Tohmon, H. Mizuno, Y. Ohki, K. Sasagane, K. Nagasawa, and Y. Hama, "Correlation of 5.0- and 7.6-eV absorption bands in SiO_2 with oxygen vacancy," Phys. Rev. B **39,** 1337-1345 (1989).

[46] L. Skuja and B. Güttler, "Detection of interstitial oxygen molecules in SiO_2 glass by a direct photoexcitation of the infrared luminescence of singlet O_2," Phys. Rev. Lett. **77,** 2093 - 2096 (1996).

[47] L. Giordano, P. V. Sushko, G. Pacchioni, and A. L. Shluger, "Electron trapping at point defects on hydroxylated silica surfaces," Phys. Rev. Lett. **99,** 136801 (2007).

[48] M. Benoit, M. Pöhlmann, and W. Kob, "On the nature of native defects in high OH-content silica glasses: A first-principles study," Europhys. Lett. **82,** 57004 (2008).

[49] K. Kajihara, L. Skuja, M. Hirano, and H. Hosono, "Formation and decay of nonbridging oxygen hole centers in SiO_2 glasses induced by F_2 laser irradiation: In situ observation using a pump and probe technique," Appl. Phys. Lett. **79,** 1757-1759 (2001).

[50] W. J. Hehre, J. Uy, P. E. Klunzinger, and L. Lou, *A Brief Guide to Molecular Mechanics and Quantum Mechanical Calculations* (Wavefunction, Irvine, CA, 1998).

[51] H. Hosono, Y. Abe, H. Imagawa, H. Imai, and K. Arai, "Experimental evidence for the Si-Si bond model of the 7.6-eV band in SiO_2 glass," Phys. Rev. B **44,** 12043-12045 (1991).

[52] U. Itoh, Y. Toyoshima, H. Onuki, N. Washida, and T. Ibuki, "Vacuum ultraviolet absorption cross sections of SiH_4, GeH_4, Si_2H_6, and Si_3H_8," J. Chem. Phys. **85,** 4867-4872 (1986).

[53] M. Karplus and R. N. Porter, *Atoms and Molecules: An Introduction for Students of Physical Chemistry* (Benjamin/Cummings, Menlo Park, CA, 1970).

[54] W. Kolos and L. Wolniewicz, "Potential-energy curves for the $X\ ^1\Sigma_g^+$, $b\ ^3\Sigma_u^+$, and $C\ ^1\Pi_u$ states of the hydrogen molecule," J. Chem. Phys. **43,** 2429-2441 (1965).

[55] D. L. Griscom and E. J. Friebele, "Fundamental defect centers in glass: ^{29}Si hyperfine structure of the nonbridging oxygen hole center and the peroxy radical in *a*-SiO_2," Phys. Rev. B **24,** 4896-4898 (1981).

[56] S. C. Langford, J. T. Dickinson, L. C. Jensen, and L. C. Pederson, "Positive ion emission from the fracture of fused silica," J. Vac. Sci. Technol. A **7,** 1829-1834 (1989).

[57] L. Skuja, M. Hirano, and H. Hosono, "Oxygen-related intrinsic defects in glassy SiO_2: Interstitial ozone molecules," Phys. Rev. Lett. **84,** 302-305 (2000).

[58] K. Kajihara, L. Skuja, M. Hirano, and H. Hosono, "Role of mobile interstitial oxygen atoms in defect processes in oxides: Interconversion between oxygen-associated defects in SiO_2 glass," Phys. Rev. Lett. **92,** 015504 (2004).

CHAPTER TWO

Interaction of vacuum ultraviolet excimer laser radiation with fused silica: II. Neutral atom and molecule emission

Sharon R. George, S. C. Langford, and J. T. Dickinson*

Abstract

We report mass-resolved time-of-flight measurements of neutral Si, O, and SiO from ultraviolet-grade fused silica during pulsed 157-nm irradiation at fluences well below the threshold for optical breakdown. Although the emission intensities are strongly affected by thermal treatments that affect the density of strained bonds in the lattice, they are not consistently affected by mechanical treatments that alter the density of point defects, such as polishing and abrasion. We propose that the absorption of single 157 nm photons cleave strained bonds to produce defects that subsequently diffuse to the surface. There they react with dangling bonds to release neutral atoms and molecules. Hartree-Fock calculations on clusters containing these defects support the contention that defect interactions can yield emission. More direct emission by the photoelectronic excitation of antibonding chemical states is also supported.

1. Introduction

Fused silica is a technologically important optical material for UV applications. Despite a bandgap of 8.9 eV,[1] fused silica is not suitable for most optical applications at 157 nm (7.9 eV) due to strong absorption by point defects[2] and an Urbach tail of disorder-related states.[3] These states may also facilitate the etching of fused silica surfaces by F_2 excimer lasers.[4-6]

Particle emission can be a valuable probe of interactions between optical materials and laser radiation in the near-surface region. In companion papers, we describe observations of positive ions[7] and negative ions[8] from fused silica during 157-nm irradiation at fluences well below the threshold for optical breakdown. Here we report observations of the emission of neutral atoms and molecules in vacuum from fused silica surfaces during 157-nm irradiation under comparable conditions. The number of neutral atoms and molecules emitted during laser irradiation is typically six orders of magnitude greater than the number of ions. Thus the great majority of the material removed during laser etching at 157 nm appears as neutral atoms and molecules.

SiO is generally the most intense neutral particle observed during 157-nm irradiation; Si and O (16 amu/e) are also detected. Neutral emissions have been previously observed during the excimer laser irradiation of other wide band-gap (but crystalline) materials at photon energies below the bandgap.[9-13] In each case, the emission intensities show strong, non-linear fluence dependences. In contrast, the neutral emission intensities from fused silica during 157-nm irradiation are relatively weak functions of fluence—about first order. Moreover, a significant fraction of the detected atoms and molecules are released from the surface well after the laser pulse, producing long tails in the time-of-flight signals. We present models of the bond breaking necessary for the production of these signals. Hartee-Fock calculations on silica clusters confirm that reactions between surface and subsurface defects can lead to the emission of these neutral species. We propose that the high efficiency of defect production by photon absorption at

stained bonds is responsible for the high intensities and weak fluence dependences of the observed neutral emissions from fused silica during 157-nm irradiation.

2. Experiment

Samples were cut from UV grade fused silica from Heraus-Amersil (Suprasil 2) using a diamond saw and then cleaned in ethanol. This material is a high purity silica (typically 1 ppm total metal content) with a high water content (typically 1200 ppm OH). To modify the character and density of surface defects, some samples were abraded with 600-grit SiC sandpaper or polished to a 0.3-μm surface finish with alumina or diamond abrasives. Extensively deformed surfaces were produced by forming an array of indentations on a polished surface with a diamond scribe; care was taken to avoid fracture. Surfaces with relatively low densities of mechanically-produced defects were produced by annealing polished samples at 1100 °C for eight hours. Surfaces with relatively low densities of mechanically produced defects but relatively high fictive temperatures (high densities of strained bonds) were prepared by annealing polished samples at 1400 °C for 10 minutes in a vertical tube furnace and then dropping them into a beaker of room temperature, 3 M nitric acid. Although some of these treatments are expected to leave hydrogen- and carbon-rich residues, no emission of water, OH, H, H_2, or CO was detected under the conditions of this work. Residual contaminants from these treatments were likely desorbed by the first few laser pulses and did not contribute significantly to the observed emissions.

Samples were mounted on a translation stage directly in front of and normal to the axis of a UTI 100C quadrupole mass spectrometer (QMS). All experiments were performed in a vacuum chamber with a base pressure of about 3×10^{-7} Pa. 20-ns pulses of 157-nm laser radiation were provided by a Lambda Physik LPF200 laser (F_2 excimer) at a pulse repetition rate of 5 Hz. The beam was focused to a 0.008 cm^2 spot on the sample with a calcium fluoride lens. The pulse energies were measured with a Star Tech Instruments model CF20C energy probe for

157 nm. The fluences reported below were obtained by dividing the pulse energy by the spot size.

Neutral atoms and molecules were ionized by electron impact with 70-eV electrons. Ions exiting the mass filter were detected with a Channeltron electron multiplier (CEM) biased to detect positive ions. The output of the detector was amplified, discriminated, and pulse counted over 200-ns intervals with an EG&G PARC 914P multichannel scaler. Unless otherwise noted, the signals accompanying 200 successive pulses on the same spot were summed. Most of the time-of-flight signal intensities below are reported in terms of counts per microsecond (MHz): counts per laser pulse per channel interval (in microseconds).

The mass-selected time-of-flight (TOF) signals in this work are quite broad and are not satisfactorily described by thermal desorption limited to the duration of the laser pulse.[14] As described below, emission is sustained for hundreds of microseconds after the laser pulse. To describe this sustained emission, we assume that emission after the laser pulse is rate-limited by a thermally activated process whose rate decreases as the laser-heated surface cools. If the density of adsorbed species is not significantly depleted by emission, the corresponding emission rate $S(t')$ is given by:

$$S(t') = S_0 \exp\left[\frac{-E_a}{kT(t')}\right] \quad , \tag{1}$$

where t' is time after the laser pulse, S_0 is a constant, E_a is an activation energy, k is the Boltzmann constant, and $T(t')$ is the surface temperature. Equation (1) describes emissions that are rate-limited by thermal desorption from the surface and/or by thermally-activated diffusion to the surface.

The absorption of silica at 157 nm is dominated by the Urbach tail of disorder-related states extending from the silica conduction band into the nominal bandgap. The corresponding state densities are high enough to yield strong absorption, but well below atomic densities.

Under these conditions, it is possible for photon fluxes employed in this work (at least 10^{17} cm^{-2} per laser pulse) to saturate the absorbing defects in a thin surface layer. In this case, Beer's law does not apply. To describe the surface temperature as a function of time, we assume that a surface layer of thickness a is uniformly heated to a temperature $T_{RT} + \Delta T$, where T_{RT} is room temperature and ΔT is the temperature change due to the laser pulse. Assuming that the material cools by thermal diffusion, the surface temperature after the laser pulse varies as:[15]

$$T(t') = T_{RT} + \Delta T\, erf\left(\frac{a}{2\sqrt{\kappa t'}}\right) = T_{RT} + \Delta T\, erf\left(\frac{\alpha}{\sqrt{t'}}\right), \quad (2)$$

where κ is the thermal diffusivity, and $\alpha = a/(2\kappa^{1/2})$; α^2 has units of seconds and the time scale for surface cooling. For simplicity, we assume that α is independent of temperature.

The velocities of particles desorbed in thermal equilibrium with a surface are described by the Maxwell-Boltzmann distribution for effusing particles. The detected signal is proportional to the particle density in the quadrupole ionizer, which is readily obtained by transformation of the velocity distribution. We employ a coordinate system where the particles are emitted from the origin, with the sample lying in the *y*-*z* plane, and the quadrupole ionizer is centered at position (d = 10.5 cm, 0, 0) along the *x*-axis. (For simplicity, we assume that all ionization takes place at the center of the 3-cm long ionizer mounted at the entrance aperture of the mass filter, and that these ions immediately enter the mass filter.) As in Eq. (1), we take t' to be the time of emission, where t' = 0 at the laser pulse. After the particles are ionized, they require time t_Q to travel the 15.5-cm length of the mass filter before reaching the detector at time t. In this work, t_Q was computed iteratively for each experimental arrival time, t, noting that each ionized neutral gains 15 eV of kinetic energy as it passes into the mass filter. (The interior of the ionizer is held at a potential of +15 eV relative to the average potential along the central axis of the mass filter.) The contribution of particles emitted at time t' to the signal detected at time $t > (t' + t_Q)$ is

$$M(t-t') = \frac{S(t')\eta d}{2\pi\left[t-t_Q-t'\right]^4}\left(\frac{m}{kT(t')}\right)^2 \exp\left\{\frac{-md^2}{2kT(t')\left[t-t_Q-t'\right]^2}\right\} \quad (3)$$

where η is the quadrupole sensitivity (counts per second per particle in ionizer, assumed to be constant over the ionizer volume), and m is the particle mass. The resulting quadrupole output $I(t)$ is the integral of contributions due to particles emitted at times $t' < (t - t_Q)$:

$$I(t) = \int_0^{t-t_Q} S(t')MB(t-t')dt' \quad . \quad (4)$$

The integral was solved for each experimental time by Romberg's method. The four model parameters (S_0, E_a, α and ΔT) were chosen to minimize the variance between the curve of Eq. (4) and the data using nonlinear least-squares techniques (the Levenburg-Marquart algorithm[16,17]).

This model provided a good description of the signals and provided physically reasonable parameters. This was not the case for several other models of similar complexity, including models based on linear, Beer's law absorption.

Hartree-Fock calculations were performed with the 6-31G* basis set on a variety of silica clusters incorporating defects using the Wavefunction (Irvine, CA) Spartan '06 molecular modeling program.

3. Results and Discussion

3.1 Mass-selected time-of-flight signals

Direct versus indirect signals. At the level of sensitivity of our quadrupole mass spectrometer, we detect three neutral species from silica during 157-nm irradiation: SiO, Si and

O. As noted below, the emission intensity typically drops about 30% during the first 300 laser pulses. Unless otherwise stated, the surface was exposed to 300 laser pulses prior to acquiring time-of-flight data to minimize the effect of this initial surface evolution. Figure 1 shows a raw time-of-flight signal (marked "total emission") for the most intense neutral product, SiO, from polished silica at a fluence of 1.2 J/cm^2 per pulse. This time-of-flight is much broader than simple Maxwell-Boltzmann distributions with the same peak time-of-flight. Unfortunately, broad time-of-flight signals are often distorted by the contribution of particles that bounce off nearby surfaces into the quadrupole ionizer. To characterize the contribution of particles reaching the ionizer by these indirect paths, time-of-flight measurements were made after blocking the direct path between the sample and the ionizer with a copper plate; the resulting signal is marked "indirect beam" in Fig 1. The signal we can physically interpret includes only those particles that travel directly from the sample to the ionizer, that is, the difference between the unblocked signal (total emission) and the blocked signal (indirect beam). This difference signal is labeled "direct beam" in Fig. 1.

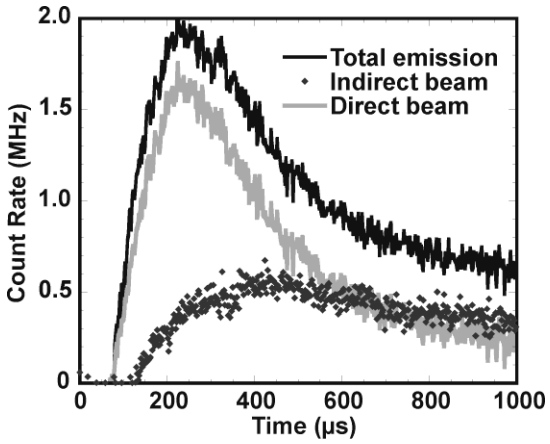

Fig. 1. Neutral SiO from as-cut fused silica exposed to 157-nm radiation at a fluence of 1.2 J/cm^2 per pulse. The curve labeled total emission is the raw data. The curve labeled indirect beam was obtained by blocking the direct path between the sample and the ionizer. The direct beam is the difference between the total emission and the indirect beam.

The small mass difference between CO_2 and SiO is not resolved by our mass filter. Since CO_2 is a common vacuum system contaminant, care was taken to rule out CO_2 as a major source of the signal at 44 amu. The fragmentation of CO_2 in the ionizer under the conditions of this work produces a weak signal at 12 amu (C) and stronger signals at 16 amu (O) and 28 amu (CO); the intensities of the signals at 16 amu and 28 amu are roughly equal. No signal at 12 amu was detected during laser irradiation. Further, signal intensity at 28 amu (Si or CO) is typically at least twice the intensity at 16 amu (O). Thus the contribution of CO_2 to the signal at 44, 28 or 16 amu is modest at best.

Corrected, "direct" time-of-flight signals for each of the observed species at a fluence of 1.2 J/cm^2 are shown in Fig. 2. Even after subtracting the indirect signal due to particles bouncing off the vacuum system walls, the time-of-flight signals remain well above background 1000 μs after the laser pulse. In our apparatus, particles emitted with thermal velocity distributions during the laser pulse (well described by Maxwell-Boltzmann distributions) typically decay to near-background levels in less than 500 μs. As might be expected, the time-of-flight distributions in Fig. 1 are poorly described by simple Maxwell-Boltzmann distributions for effusive particles, *if* we assume that the particles are emitted during the laser pulse. (Forced curve fits yielded unphysically low effective temperatures—often below room temperature.) Therefore we conclude that particle emission in not confined to the duration of the laser pulse, but continues for some hundreds of microseconds after the laser pulse. The dashed line in Fig. 2(a) represents the source function $S(t')$ for SiO (in arbitrary units) where t' is the time of emission after the laser pulse. To adequately describe these time-of-flight signals, the source function must remain significantly positive for times on the order of 1 ms.

Contribution of SiO fragments to Si and O signals. In the case of atomic Si and O, the fragmentation (cracking) of molecular SiO in the quadrupole ionizer can contribute to the Si and O signals. As each of the ionized neutrals pass into the mass filter, they are accelerated to the same kinetic energy (15 eV). When SiO molecules and fragments ionized at the same time, the lighter Si and O fragments will therefore reach the detector before the heavier SiO. In our

apparatus, the Si and O signals corresponding to SiO fragments would lead the SiO signal by 12 μs and 20 μs, respectively. Since observed Si and O signals lead the SiO signal by at least twice

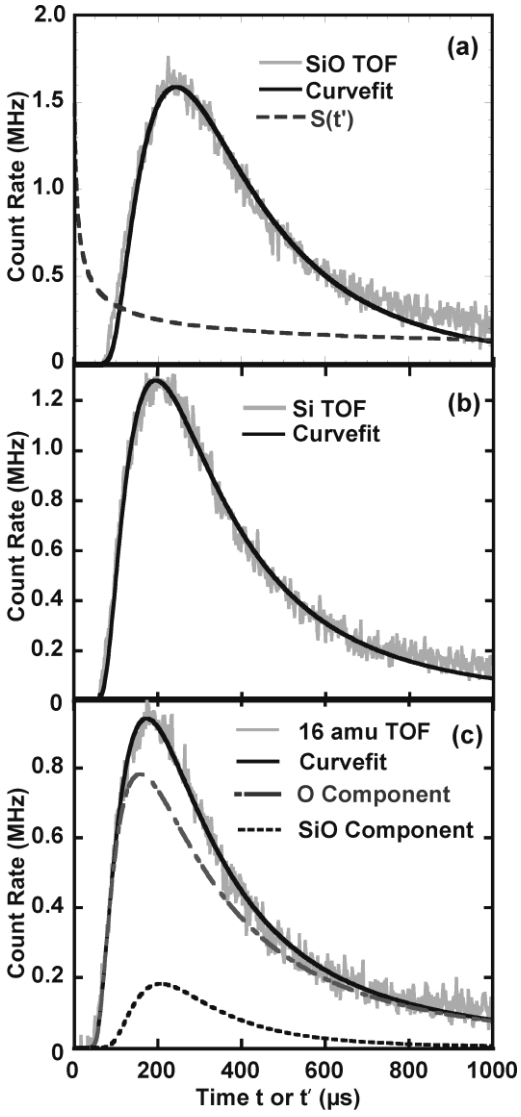

Fig. 2. Time-of-flight signals for neutral (a) SiO, (b) Si, and (c) O from polished fused silica exposed to 157-nm radiation at a fluence of 1.2 J/cm^2 per pulse. The dark line in each diagram represents a least squares fit of Eq. (4) to the data. The dashed line in (a) shows the source function $S(t')$ used in the curve fit for SiO (arbitrary units), where t' is the time of emission after the laser pulse. The dashed line in (c) represents the expected contribution of atomic O produced by the dissociation of SiO in the quadrupole ionizer. The contribution of Si produced by the dissociative ionization of SiO in (b) could not be unambiguously determined and is neglected. The maximum effective surface temperatures employed for the curve fits in (b) and (c) were constrained to equal that in (a) for SiO: $T_{RT} + \Delta T = 1170$ K.

these amounts, the majority of the observed O and Si signals can be assigned to atomic O and atomic Si emitted directly from the surface. Consistent with emission in thermal equilibrium with the surface, the leading edges of the time-of-flight signals for each species shift to shorter times with increasing fluence. In the model, this behavior was ensured by giving each particle thermal velocities appropriate to the surface temperature at the time of emission.

The dark line in Fig. 2(a) show a least squares fits of Eq. (4) to the SiO time-of-flight signal. This model incorporates a thermally activated process that allows for sustained emission after the laser pulse. The curve fitting procedure for the SiO signal yields a peak effective surface temperature of 1170 K. Assuming that SiO, Si, and O are emitted in thermal equilibrium with the surface, their time-of-flight signals should reflect the same peak surface temperature. In the curve fits of Fig. 2, the peak surface temperatures for the Si and O signals were fixed at the value obtained for SiO. This procedure was necessary to overcome numerical uncertainties caused by the contribution of SiO fragments to the Si and O signals.

The Si signal is significantly more intense than the expected signal due to SiO fragments, making it difficult for curve fitting techniques to characterize the proportionally small contribution of SiO fragments. Reasonable fits of Eq. (4) to the Si time-of-flight signals are obtained when SiO fragments are neglected. This is not the case for the relatively weak signal due to atomic O in Fig. 2(c). The dashed line in Fig. 2(c) shows the expected contribution of SiO fragments (taken as a fraction of the SiO intensity, corrected for O time-of-flight through the mass filter) required to adequately describe the O signal.

Curve fit parameters for SiO. The peak surface temperatures obtained from curve fits to the SiO signals (the most intense neutral product) increase from 600 to 1400 K as the fluence is raised from 0.7 to 2 J/cm^2. The highest temperatures are still below the melting point of fused silica (about 1600 K), consistent with the lack of melt-like surface features in scanning electron microscope images of our irradiated surfaces. We note that temperatures near the material *boiling* point (about 2230 °C for fused silica) are normally required to produce detectable

quantities of vapor during a nanosecond laser pulse. In previous work on neutral emissions during 248-nm irradiation of MgO,[9] NaCl,[10] $NaNO_3$,[11] Si_3N_4[12] and $CaHPO_4 \cdot 2H_2O$[13], we found that the effective surface temperatures derived from time-of-flight analysis often exceeded the material *boiling* points at fluences sufficient to produce melt-like features on the surface. The activation energies for these emissions, when determined, were consistent with thermal vaporization or decomposition.

Thermally activated processes with activation energies greater than about 2 eV (including typical vaporization enthalpies) are strong functions of temperature, and the resulting emission is generally confined to the duration of peak surface temperatures (usually less than a microsecond). Even at room temperature, the thermal desorption of loosely bound species (binding energies < 0.2 eV) can be rapid and complete on time scales of microseconds. Under these conditions, time-of-flight signals behave as if emission were confined to the duration of the laser pulse. Emissions with thermal velocities well after the laser pulse are most likely due to the production of weakly bound species well after the laser pulse. The activation energies [E_a in Eq. (1)] obtained by fitting Eq. (4) to the SiO, Si and O signals are 0.8, 0.6 and 0.5 eV, respectively. Similar values were obtained from time-of-flight signals acquired over the entire range of probed fluences. These activation energies are below those expected for the diffusion of O and Si in fused silica[18] and well below the enthalpy for the vaporization of silica (5-7 eV).[19] Yet they are well above typical binding energies for physisorbed atoms and molecules (< 0.2 eV). As discussed below, we propose that moving chain fragments generated by the photolysis of Si-O bonds play a critical role in the emission process. Although the relevant activation energies are not known, these motions are presumably thermally activated.[20]

The time-of-flight signals over the entire range of fluences were adequately described by $\alpha = a/(2\kappa^{1/2}) \approx 0.02\ s^{1/2}$, where $\alpha^2 \approx 400\ \mu s$ corresponds to a time-scale for surface cooling by thermal conduction. In the context of the model, this time scale parameter and the room temperature thermal diffusivity, $\kappa \approx 0.007\ cm^2\ sec^{-1}$,[21] require that the silica is uniformly heated to a depth $a \approx 30\ \mu m$. This is less than 10% of the measured, linear absorption depth of high-OH

silicas at 157 nm (≈ 400 μm).[22] Although the value of a is lower than one might expect, the laser fluences employed in this work are simply too low to significantly heat the material in a layer of this thickness. The change in surface temperature, ΔT, due to a radiant energy input per unit area, J, absorbed uniformly in a surface layer of thickness a over a time interval τ (τ must be much less than the time scale for thermal diffusion), is given by

$$\Delta T = \frac{(1-R)J}{\rho c_p a} \quad , \tag{5}$$

where $R \approx 0.1$ is the surface reflectivity, $\rho \approx 2.2$ g cm^{-2} is the density, and $c_p \approx 0.8$ J g^{-1} K^{-1} is the specific heat capacity. Using values from the curve fit in Fig. 2 ($a \approx 30$ μm and $J = 1.2$ J cm^{-2}), ΔT in Eq. (5) is 205 K—about 25% of the ΔT derived from our time-of-flight measurements at this fluence—about 900 K in Fig. (2). As required for self-consistency, the time scale for the deposition of thermal energy (equal to the 20 ns laser pulse duration), is much less than the time scale for thermal diffusion $\tau = a^2/\kappa \approx 60$ ms, assuming a typical room temperature thermal diffusivity $\kappa \approx 0.007$ cm^2 s^{-1}.[21]

More plausible surface temperatures can be reached if a small fraction of the laser energy is deposited in a much thinner surface layer. For the purpose of temperature estimates, heated layers that are thinner than the thermal diffusion length δ will behave roughly as if they are one diffusion length thick, where $\delta = (\kappa \Delta t)^{1/2} \approx 150$ nm for the duration $\Delta t = 30$ ns of our laser pulse. If 2% of the laser energy is deposited within a layer of thickness $a = \delta = 150$ nm along the surface, the surface temperature rise from Eq. (5) is 700 K—sufficient to account for the TOF derived surface temperature at 1 J/cm^2. Measurements of enhanced near-surface absorption in silica at 157 nm are difficult due to the strong bulk absorption at this wavelength. However, strong, near-surface absorption has been observed in polished fused silica at 248 nm, where silica is nominally transparent.[23] At much higher fluences (high enough to yield measurable etching), etch rate versus fluence measurements have yielded much lower effective absorption depths

corresponding to $a \approx 50$ nm.[24] Thus it is reasonable to expect a significant enhancement of laser absorption in the near-surface region under conditions that yield neutral emission.

If laser-induced heating is confined to a submicron surface layer, the room-temperature thermal diffusivity is much too high to account for thermally driven emission 100 μs after the laser pulse. Assuming $a = 150$ nm and $\kappa = 0.007$ cm^2/s,[21] Eq. (2) yields $\alpha \approx 1 \times 10^{-4}$ s$^{1/2}$. The corresponding time scale for cooling ($\alpha^2 \approx 10$ ns) is much too fast for significant emission after the laser pulse. The known thermal diffusivity of bulk fused silica increases only gradually with temperature over the expected temperature range,[21] and this change is in the wrong direction to account for sustained emission. We are forced to require a significantly lower thermal diffusivity in the near surface layer and point out that this would be consistent with a locally high degree of lattice disorder. As noted below, we find that annealing treatments that reduce lattice disorder virtually eliminate neutral emission.

3.2 Role of defects in neutral emission

Effect of mechanical and thermal treatments. Previous measurements of positive ion emission from fused silica during 157-nm irradiation show much more intense emissions from samples subjected to mechanical treatments such as cutting, polishing, abrasion, and indentation.[7] These same mechanical treatments have *little effect* on the neutral intensities. Figure 3 shows the relative intensity of the SiO, Si and O detected during the first 200, 1.5 J/cm^2 laser pulses on previously unexposed sample surfaces after various mechanical and thermal treatments. With the exception of the quenched sample, SiO is consistently the most abundant neutral. The total counts for all three neutral species detected from samples without thermal treatments are quite similar, regardless of whether the samples are tested as-cut, after polishing, after abrading, or after indenting. This insensitivity to treatment is consistent with the suggestion above that pre-existing point defects play a relatively small role in the process of neutral emission.

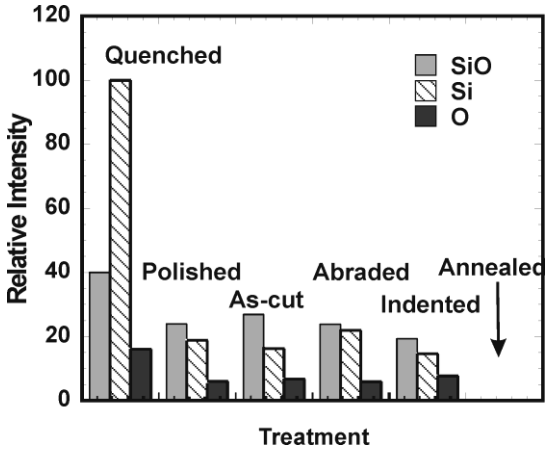

Fig. 3. Total SiO, Si and O counts detected during the first 200 laser pulses at a fluence of 1.5 J/cm^2 from previously unexposed spots on fused silica surfaces after six different thermal and mechanical treatments.

In contrast with mechanical treatments, *thermal* treatments dramatically affect the neutral emission intensities. After an eight-hour anneal in air at 1100 °C, followed by a slow cool-down (1 °C/min), neutral emission from polished samples is virtually eliminated (Fig. 3, right hand bars). This sample is expected to have a much lower density of strained bonds than any of the mechanical treated samples. In contrast, a ten-minute anneal in 1400 °C argon, followed by rapid quenching, doubles the SiO and O intensities and quadruples the Si intensity (Fig. 3, left hand bars). Quenching freezes in the relatively high structural disorder generated at high temperatures and leads to high densities of strained bonds. As discussed below, strained bonds are readily cleaved by the absorption of single 7.9 eV photons, thereby generating defects that yield neutral emission.

Effect of prolonged irradiation. Figure 4 shows the evolution of the neutral SiO, Si, and O intensities from polished fused silica during the first ten thousand pulses at a fluence of 1.8 J/cm^2. During the first 300 pulses on previously unexposed surfaces, the intensity drops about 35% for SiO, 40% for Si, and 25% for O. Over the next 10,000 pulses, the intensity gradually plateaus for all three neutral species. Eventually the intensities of the Si and O signals

slowly begin to rise again. The dark lines in Fig. 4 are least squares fits of a empirical function incorporating the sum of an exponential decay and a linear rise to emphasize the persistence of these emissions.

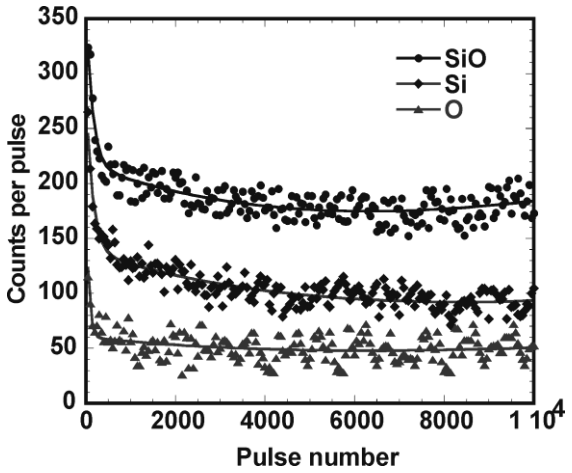

Fig. 4. SiO, Si and O intensities from polished fused silica during prolonged exposure to 157-nm radiation at a fluence of 1.8 J/cm^2 per pulse. The dark lines represent curve fits to the data incorporating the sum of two terms, one describing an exponential decay and the other a linear growth.

This behavior is consistent with simultaneous "clean up" and "induction" processes: laser exposure rapidly destroys pre-existing defects that participate in emission and slowly produces new ones. The size of the initial drop (about 30%) provides a rough indication of the contribution of pre-existing defects to the initial emission intensity (the first data point in Fig. 4). In contrast, previous measurements of the positive ions O^+ and Si^+ under similar conditions show drops of 90% during the initial stages of exposure.[7] As discussed below, we attribute the relatively small influence of pre-existing defects on the neutral atom and molecule intensities to the extraordinarily high efficiency of laser-induced defect production at strained bonds.

Effect of laser fluence. Figure 5 shows a $\log_{10}$-$\log_{10}$ plot of the SiO, Si, and O intensities as a function of fluence on as-cut fused silica. In each case, the signal intensities are remarkably weak functions of fluence (slope ≈ 1). This weak fluence dependence contrasts

dramatically with previous measurements in our laboratory of neutral emissions from other materials at longer laser wavelengths. For instance, the intensities of neutral atoms and molecules during by 248-nm irradiation from MgO,[9] NaCl,[10] $NaNO_3$,[11] Si_3N_4[12] and $CaHPO_4 \cdot 2H_2O$[13] are strongly nonlinear functions of fluence. As implied above, the presence of strained bonds in fused silica (absent in these crystalline materials) raises the efficiency of defect formation by single photon absorption and helps explain this weak fluence dependence.

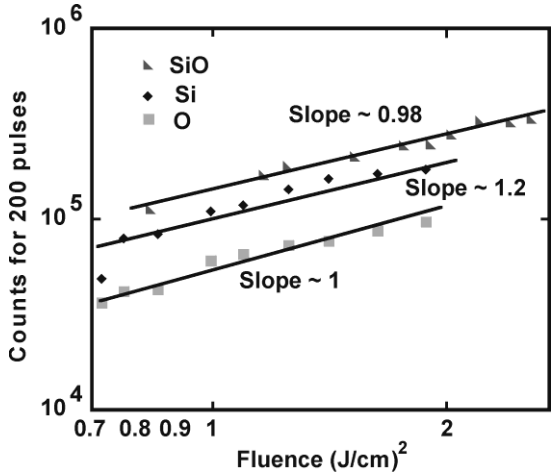

Fig. 5. Emission intensities (total counts for 200 laser pulses) for neutral SiO, Si, and O as a function of fluence from as-cut fused silica.

3.3 Hartree-Fock calculations on candidate defect configurations

To investigate the role of bond cleavage and laser-induced defects on neutral emission, we performed Hartree-Fock calculations on a variety of defect configurations in silica clusters. Small clusters with nearby defects can be unstable, in that the equilibrium (possibly metastable) configuration includes a small neutral atom or molecules. Our procedure was to first to construct a stable cluster containing a surface defect (such as an NBOHC). After computing the equilibrium geometry, the cluster was modified by the addition of a second defect structure. The

equilibrium geometry was then recomputed. If the resulting equilibrium geometry included a small molecule fragment, that structure was identified as a potential source of emission. This identification is tentative in the sense that the instability introduced by the second defect can be greater than that produced by 157-nm irradiation. As described below, the results nevertheless support a possibly dominant mechanism for small molecule emission from fused silica.

A typical silica cluster consisted of four, six-member rings connected in a tetrahedral fashion, with each ring forming a face of the tetrahedron. With the exception of oxygen in NBOHCs and peroxy radicals, all nonbridging oxygen ions were terminated with hydrogen. Candidate defect interactions for neutral O, SiO and Si emission are presented below.

Defects interaction yielding O. Figure 6(a) shows the equilibrium geometry with four six-member rings, with an un-terminated, nonbridging oxygen ion near the top of the cluster. A simplified diagram of the structure, with most of the oxygen atoms removed, is shown in the inset. When the cluster is given a net +1 *e* charge, most of the net positive charge is localized on the oxygen ion, rendering it nearly neutral. Thus it corresponds to a surface NBOHC. The cluster was locally constrained by bridging one of the six member-rings with a silica tetrahedron to form a four-member ring, shown in the lower left corner of the inset. Four-member rings are believed to enhance the absorption of silica at 157 nm.[25]

Removing the linking silica tetrahedron dramatically alters the equilibrium geometry, as shown in Fig. 6(b). In particular, the Si-O bond to the terminal oxygen has been broken and replaced with a bond to a nearby hydroxyl unit; the new bond is indicated by the dotted line in (b). To accelerate convergence, the length of the Si-O bond in the terminal O was fixed at 5 Å. (Successive iterations of the energy minimization routine gradually increased the bond length and presumably would have done so until the interaction between the cluster and the terminal O became negligible.) The final equilibrium geometry incorporates two new rings (formed by the reaction with the hydroxyl unit), two fewer nonbridging oxygen atoms, and a neutral, isolated oxygen atom. This geometry is consistent with the emission of the terminal oxygen as a neutral atom. If the ejected oxygen atom remains physisorbed to the surface, it could be thermally

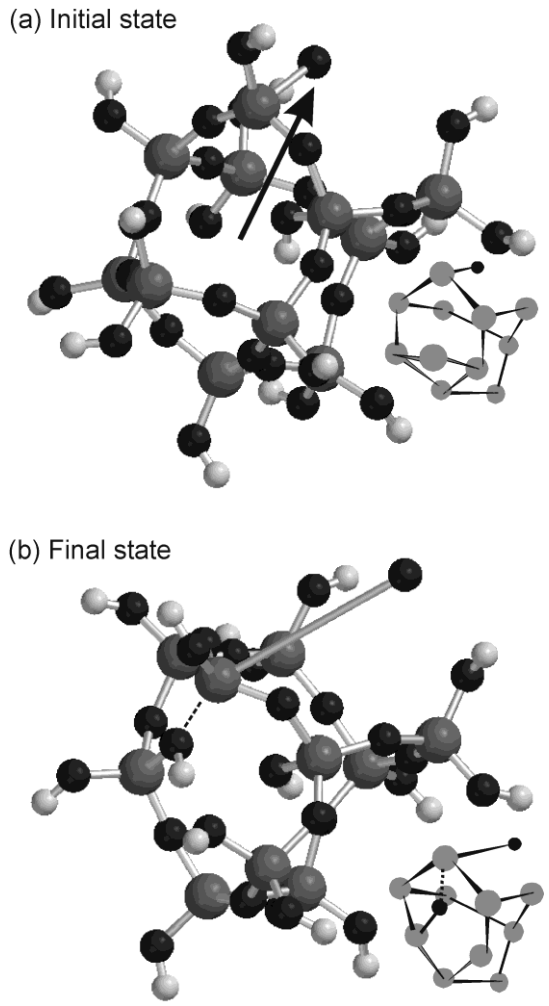

Fig. 6. Hartree-Fock equilibrium geometries for silica clusters with an unterminated, nonbridging oxygen (marked by the arrow): (a) Cluster incorporating a four member ring in the lower left corner. The inset is a simplified diagram of the structure showing only the Si atoms (light colored circles) and important oxygen atoms (dark circles). Some of the silicon atoms have been displaced for clarity. (b) Cluster after the four-member ring is broken by removing a silicate unit. In the subsequent reorganization, the silicon ion with the nonbridging oxygen briefly becomes five-fold coordinated. [The fifth bond is indicated by the dotted line in (b).] Four-fold coordination is restored when the nonbridging oxygen is ejected.

desorbed later. In practice, the reorganization of bonds in the cluster may also involve thermally activated steps. In either case, the emitted oxygen atoms would have thermal velocity distributions appropriate to the surface temperature at the time of emission. Since the defect

reactions leading to emission can require atomic motion or diffusion, they can account for emission long after the laser pulse.

The proposed reaction leading to O emission is analogous to the condensation reaction:

$$\equiv Si(OH) + \equiv SiO\bullet \rightarrow \equiv Si(OH\bullet)Si\equiv + O \quad , \qquad (6)$$

where the ≡ symbol indicates bonding to three nearest neighbor oxygen atoms and • indicates an unpaired electron. The species on the left hand of Eq. (6) side are both present prior to irradiation. Until the strained bond in the cluster of Fig. 6(a) is removed, the reacting species are separated. Emission occurs only after the constraint provided by the strained bond is removed. One can envision similar scenarios that would yield the same result. For instance, it is known that the SiO radical (NBOHC) is produced directly by one- and two-photon absorption processes at 157 nm.[26]

Most bonds cleaved during irradiation presumably reform to restore the lattice to its original structure. In a small minority of cases, the resulting NBOHC and E' centers separate and exist independently for long times. Condensation reactions between NBOHCs and nearby Si atoms [as in Eq. (5)] are also relatively rare, but technologically important. These reactions restructure the lattice to form smaller, more strained rings that increase the local average density (densification). Since strained rings are especially vulnerable to photolysis by single, 157-nm photons,[26,27] bond reorganization during 157-nm irradiation tends to be self-perpetuating, limited primarily by accumulating lattice strain.

Defect interactions yielding SiO. We also explored a number of cluster geometries incorporating an adsorbed Si-O unit that would account for the emission of neutral SiO. The equilibrium geometry of a cluster involving a dangling Si-O unit bonded to it is shown in Fig. 7(a). This cluster is composed of four six-member silicate rings joined in a tetrahedral fashion (no small rings). A simplified diagram of the structure, with most oxygen atoms omitted, is shown in the inset. The net cluster was assigned a +1 *e* charge that is largely localized on the

pendant Si-O unit. The length of the Si-Si bond linking the Si-O to the rest of the cluster is 2.40 Å—

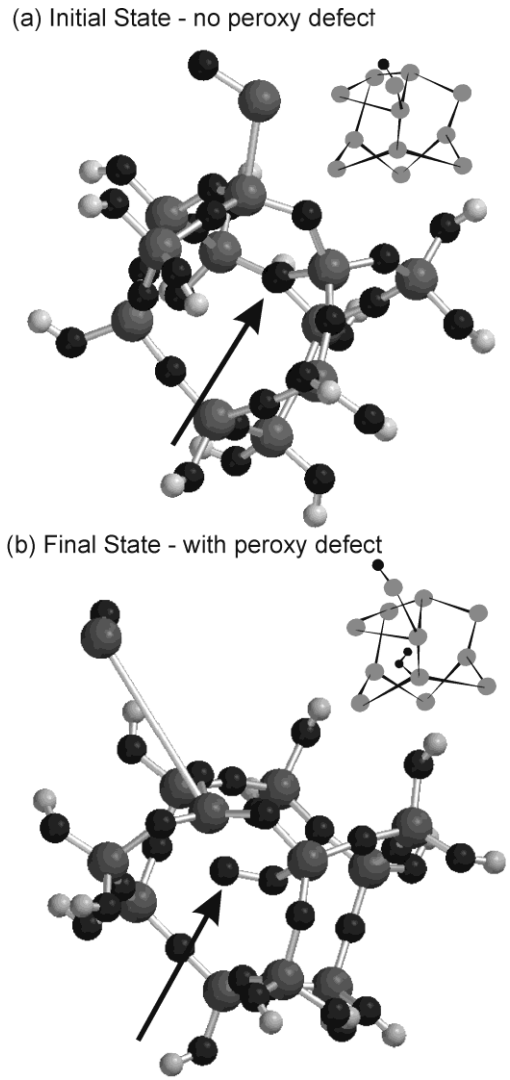

Fig. 7. Equilibrium geometry computed by Hartree-Fock methods for a silica cluster with a pendant Si-O unit: (a) with a hydroxyl unit in the interior of the cluster, and (b) after replacing the hydroxyl unit with a peroxy unit. In the presence of the peroxy unit, the cluster is unstable against neutral SiO emission. The insets in (a) and (c) show simplified diagrams of the cluster structure; all the Si atoms (light colored circles) are shown, but only the most important oxygen atoms (dark circles); some atoms in the insets have been displaced for clarity.

comparable to Si-Si bond lengths in the oxygen deficiency center (I) [ODC(I), also denoted the neutral oxygen vacancy] in crystalline quartz (2.37 Å when calculated with the 6-31G* basis set).[28]

The cluster of Fig. 7(a) is rendered unstable by replacing the central hydroxl radical with a peroxy defect (e.g., ≡Si–O–O•), as shown in Fig. 7(b). Successive iterations of the energy minimization routine lengthened the Si-Si bond until the Si-Si interaction was virtually nil. The Si-Si bond length was then fixed at 5.1 Å to accelerate convergence. The resulting equilibrium geometry is shown in Fig. 7(b). In the final geometry, the positive charge of the final cluster is localized on the peroxy defect (a hole trap), leaving the departing SiO molecule neutral. Thus peroxy defects generated near defective surfaces are likely to induce neutral emission. Again, the time required for defect diffusion or SiO desorption would allow for emission well after the laser pulse, consistent with the long tails in the time-of-flight signals of Fig. 2.

Peroxy defects can be generated by reactions between NBOHC centers and mobile, neutral O produced by the absorption of 157-nm photons.[29] The net reaction can be represented as

$$2\,(\equiv Si–O–Si\equiv) \;\rightarrow\; (\equiv Si–O–O\bullet) \;+\; 3\,(\equiv Si\bullet) \quad . \qquad (7)$$

While simple bond breaking produces NBOHC (≡Si-O•) and E' centers (≡Si•) in equal numbers, peroxy radical production enhances the E' center density at the expense of the NBOHC density. The ratio of E'-centers to NBOHCs is often elevated in silicas that experience high excitation densities,[30] presumably due the formation of peroxy radicals. As noted above, 157-nm radiation at fluences below the breakdown threshold appear to be rich in Si relative to O. It is possible that the O emission deficit is compensated by the accumulation of peroxy radicals in the near surface bulk.

A more complex set of defect interactions would be required to produce the pendant Si-O unit in Fig. 7. A good starting point is the ODC(I), ≡Si–Si≡, which can be formed by the

reaction of two adjacent E' centers.[31] VUV absorption measurements on Suprasil 2 after prolonged 157-nm irradiation under the conditions of this work show unambiguous evidence for the ODC(I).[7] Subsequent reactions between an ODC(I) and nearby E' centers or NBOHCs can produce dangling SiO units such as the one in Fig. 7(a). When E' centers react with nearby Si-O-Si bridging bonds, the bond is broken and the bridging O would normally be removed. Reactions between NBOHCs and nearby Si-O-Si bridging bonds can also break the bond, but the bridging oxygen normally remains. Indicating intact bridging bonds by –, pendant SiO formation can take place by the reactions:

$$\equiv Si–Si\equiv \; + \; 2\,(\equiv Si\bullet\,) \; \rightarrow \; \equiv Si–Si– \; + \; 2\,(\equiv Si–) \qquad (8)$$

$$\equiv Si–Si– \; + \; \equiv Si–O\bullet \; \rightarrow \; \equiv Si–Si–O\bullet \; + \; \equiv Si– \qquad (9)$$

At the surface, the ≡Si–Si–O• species on the right hand side of Eq. (9) would correspond to the pendant Si-O unit in Fig. 7(a). We note that some of the bond breaking required to form the pendant SiO unit can take place *during* the laser pulse by photoexcitation, especially if the bonds are already strained. Defect production *after* the laser pulse—needed to explain emission after the laser pulse—would require reactions similar to those in Eqs. (8) and (9).

At high excitation densities, defect reactions involving broken bonds would produce a wide variety of defects, some of which would participate in other emission processes. For instance, we have proposed that surface ≡Si–Si^+ units and surface ≡Si–O–O^+ units can absorb 157-nm photons to yield Si^+ and O^+ emission, respectively.[7] And as discussed above, the surface NBOHC is the most likely source of atomic O.

Photoelectronic Si emission. We also explored the possibility that neutral emission may be produced by the direct photoexcitation of defect structures. Although the molecular dynamics simulations required to prove that excitation of a given defect structure would yield emission are not yet tractable, we can identify localized bonding-to-antibonding excitations that would favor

emission. Hartree-Fock calculations can also indicate whether these excitations absorb 157-nm photons.

Figure 8(a) shows the equilibrium geometry of a cluster candidate for neutral Si emission upon excitation. The cluster includes an adsorbed Si-O unit, like the Si-O unit in Fig. 7(a), expect that the silicon ion is in the outermost position. The cluster contains smaller, three and four member rings structures as shown in the inset in Fig 8(a). The smaller rings are necessary to prevent reactions between the terminal Si and nearby hydroxyl radicals. The large number of interconnected rings in a larger (more physical, but computationally intractable) cluster would probably provide this constraint without the need for smaller rings. In the ground state, this configuration is stable. The localized charge on the terminal silicon ion is about +1 *e*.

The molecular orbitals determined by the Hartree-Fock procedure show an important, bonding state localized on the terminal Si-O unit deep within the valence band. When ranked in order of energy, this orbital lies 46 orbitals below the highest occupied molecular orbital, denoted the HOMO-46. A surface of constant wave function density for the HOMO-46 is shown in Fig 8(b). Similarly, the orbital just above the lowest unoccupied molecular orbital (the LUMO+1) is localized on this same bond as shown in the surface of constant wavefunction density in Fig 8(c). The node between the terminal silicon and the adjacent O indicates antibonding character, consistent with a weakening of the terminal Si-O bond and eventual emission. Figure 8(c) also shows that the electron density for the LUMO+1 is highly localized on the terminal Si atom. This charge transfer would neutralize most of the initial +1 e charge localized on this same atom—consistent with Si emission as a neutral particle.

The Hartree-Fock energies for the HOMO-46 and LUMO+1 orbitals differ by about 8.1 eV. This difference is expected to be somewhat overestimated due to the tendency of Hartree-Fock calculations to overestimate orbital energies.[32] Given the breadth of defect absorption peaks in fused silica (typical half-widths in the UV: 0.4–1.3 eV)[33], the HOMO-to-LUMO excitation in Fig. 8 is reasonably well situated for the absorption of 7.9 eV photons.

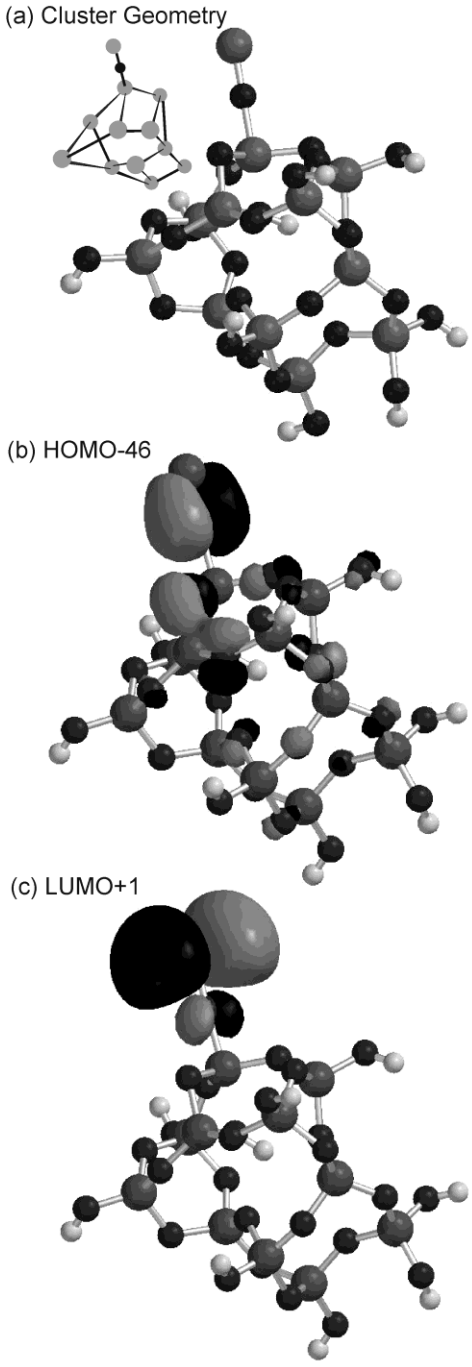

Fig. 8. Hartree-Fock equilibrium geometry for a silica cluster with a pendant O-Si unit: (a) cluster geometry showing the terminal Si atom; (b) surface of constant wave function density for the HOMO-46 state; (c) surface of constant wave function density for the LUMO+1. The node between the terminal Si and the underlying O in (c) indicates that the LUMO+1 orbital has antibonding character. The inset in (a) is a simplified diagram of the cluster structure showing all the silicon atoms (light circles) and one oxygen atom (dark circle); some atoms in the inset have been displaced for clarity.

Careful analysis of the relaxed excited state would be required to confirm that this excitation would actually yield emission. We note that the dramatic increase in Si intensity produced by quenching our samples from high temperatures, shown in Fig. 4, suggests that the production of sites for Si emission is strongly favored by high densities of strained bonds.

Emission due to the photoexcitation of antibonding states would normally be confined to the duration of the laser pulse. Emission after the laser pulse would require defect interactions similar to those described above for the emission of SiO. For example, Hartree-Fock calculations suggest that replacing the pendant Si-O unit in Fig. 7(b) with Si produces a structure that is unstable against the release of neutral Si.

3.4 Role of strained bonds in neutral emission

The structures expected to yield emission (described above) are rather complex. At least two bonds must be broken to produce defects incorporating undercoordinated silicon. An additional defect is required when emission is stimulated by a defect interaction. These factors lead us to expect that emission should be a strong, *nonlinear* function of fluence. In light of the observed *linear* fluence dependence of the neutral intensities, the dominant role of laser-induced defects in emission process presents a dilemma.

As noted above, the resolution of this dilemma lies in the extremely high efficiency of defect production when 157-nm photons are absorbed at strained bonds. It has been shown that absorption of 157-nm photons at strained bonds in fused silica can produce E' centers and nonbridging oxygen hole centers (NBOHCs) by single photon absorption processes.[25] Annealing and quenching treatments dramatically alter the density of strained bonds in silica, and both treatments dramatically alter the intensity of neutral emission. These emissions are apparently limited by the rate of defect production. Yet mechanical treatments that produce defects have almost negligible effects on emission. This may simply reflect the rapid rate of laser-induced defect production at 157 nm. For instance, the quantum efficiency for the production of the

nonbridging oxygen hole center (NBOHC) due to 157-nm absorption at strained bonds is extremely high, on the order of 10^{-4}.[26] At 1 J/cm^2, the number of photons per surface SiO_2 unit photon is about 10^3. Thus 10% of the strained bonds (four and five member rings) would be cleaved during a single laser pulse at 1 J/cm^2. Processes similar to those responsible for laser-induced compaction would produce additional strained bonds, replacing those consumed by emission.

After a few hundred laser pulses at fluences near 1 J/cm^2, the surface is modified to such an extreme degree that further irradiation has little effect on the density of structures that lead to emission. On such modified surfaces, the density of surface defects would not depend strongly on fluence. Assuming that emission requires only one additional, single-photon excitation, or a continuous supply of defects produced by single-photon excitations, the rate of particle release would be proportional to fluence, as observed.

The defect driven mechanisms described above account for the release of neutral atoms and molecules long after the laser pulse. Defects reacting after the laser pulse will be in thermal equilibrium with the surface, which would account for the (apparent) thermal velocity distributions of the emitted neutral particles. Neutral particles ejected as the result of photochemical excitations, as proposed above for Si, would not necessarily have thermal velocities. Direct photochemical emission is typically adiabatic, where the ejected species acquires a kinetic energy equal to the excess energy of the reaction. Photochemical emission would be confined to the duration of the laser pulse. The observation of what appear to be thermal velocity distributions indicates that either (1) photochemical emissions make up a small fraction of the total or (2) photochemical processes produce sorbed species that subsequently leave the surface with thermal velocities.

Effect of OH. The strained bonds responsible for single photon absorption at 7.9 eV in fused silica are strongly affected by the OH content. High-OH silicas, such as the Suprasil 2 (about 1200 ppm OH) employed in this work, have significantly lower single photon absorption cross sections than low-OH silicas.[34] E' and NBOHC production in fused silica is hindered by

the presence of OH^{35}—which is present in Suprasil 2 at a concentration of about 1200 pm. The OH ion promotes lattice relaxation in fused silica as the solid is cooled from the melt,[36] and thus reduces the density of strained bonds. The presence of OH clearly reduces the single-photon absorption in fused silica, and plays an especially prominent role in the damage resistance of high-OH silica at 157 nm.

4. Summary and Conclusions

Neutral Si, O, and SiO are emitted from the surface of fused silica under 157-nm irradiation at fluences well below the threshold for optical breakdown. The intensities are roughly proportional to fluence and are strongly affected by annealing and quenching treatments that alter the density of strained bonds in the silica lattice. Although emission is most intense during the laser pulse, the time-of-flight signals indicate that emission continues for hundreds of microseconds after the pulse. Our modeling of these signals suggests that laser absorption is strongly enhanced near the surface of polished fused silica, consistent with earlier laser calorimetry on a similar material.[23] Hartee-Fock calculations on silica clusters containing defects suggest neutral particles can be emitted when defects beneath the surface react with surface defects to form a more stable structure. In some cases, photoelectronic excitation of antibonding molecular orbitals localized at surface defects may yield emission. The scission of strained bonds by single-photon absorption can produce high densities of defects[26] that participate in both emission scenarios.

Similar bond-breaking and reorganization processes are responsible for the densification of fused silica during prolonged UV radiation at somewhat longer wavelengths.[20,37] In optical applications requiring high resolution and reproducibility, densification can significantly reduce the component lifetimes. Conversely, potentially useful optical structures have been produced by densification at 157-nm.[38] Neutral emission measurements provide a valuable, atomic-level

probe of reactions similar to those responsible for densification, and may constrain molecular dynamics models of the densification process.

In the absence of absorbing impurities and point defects, strained bonds are responsible for much of the absorption of fused silica at 157-nm.[25,39,40] These defects not only provide for single photon absorption, but provide states that enhance defect production by the sequential absorption of two 157-nm photons.[26] The resulting bond cleavage and lattice reorganization is responsible for the emission of neutral atoms and molecules at fluences well below the threshold for optical breakdown, as well as densification. Because bond cleavage and reorganization are important at temperatures well below those required to vaporize fused silica, they help account for the good machinability of fused silica under 157 nm irradiation. An understanding of the details of these processes should contribute to the controlled material removal in technological applications.

An interesting question is the possible dependence of NE intensities on the OH-content of the irradiated fused silica. (The Supersil II studied here is a high OH silica.) The strained bonds that are responsible for single photon absorption at 7.9 eV in fused silica are strongly affected by the OH content. We therefore predict that neutral emission intensities from low-OH silicas will be much higher than the intensities from Suprasil 2. Measurements are in progress to test this prediction.

Finally, we show in Ref. 8 that the observed neutral emission is an essential participant in the formation of negative ions from fused silica during 157-nm exposure.

Acknowledgment

This work was supported by the Department of Energy under Contract Number DE-FG02-04ER-15618.

References

[1] T. H. DiStefano and D. E. Eastman, "The band edge of amorphous SiO_2 by photoinjection and photoconductivity measurements," Solid State Commun. **9,** 2259-2261 (1971).

[2] H. Hosono, Y. Abe, H. Imagawa, H. Imai, and K. Arai, "Experimental evidence for the Si-Si bond model of the 7.6-eV band in SiO_2 glass," Phys. Rev. B **44,** 12043-12045 (1991).

[3] K. Saito and A. J. Ikushima, "Absorption edge in silica glass," Phys. Rev. B **62,** 8584-8587 (2000).

[4] J. Ihlemann, S. Müller, S. Puschmann, S. Schäfer, M. Wei, J. Li, and P. R. Herman, "Fabrication of submicron gratings in fused silica by F_2-laser ablation," Appl. Phys. A **76,** 751-753 (2003).

[5] D. Schäfer, J. Ihlemann, G. Marowsky, and P. R. Herman, "F_2-laser ablation patterning of dielectric layers," Appl. Phys. A **72,** 377-379 (2001).

[6] P. R. Herman, R. S. Marjoribanks, A. Oettl, K. Chen, I. Konovalov, and S. Ness, "Laser shaping of photonic materials: Deep-ultraviolet and ultrafast lasers," Appl. Surf. Sci. **154-155,** 577-586 (2000).

[7] S. R. George, J. A. Leraas, S. C. Langford, and J. T. Dickinson, "Interaction of vacuum ultraviolet excimer laser radiation with fused silica: I. Positive ion emission," J. Appl. Phys. **107,** 033107 (10) (2010).

[8] S. R. George, S. C. Langford, and J. T. Dickinson, "Interaction of vacuum ultraviolet excimer laser radiation with fused silica: III. Negative ion formation," J. Appl. Phys. **107,** 033109 (10) (2010).

[9] D. R. Ermer, S. C. Langford, and J. T. Dickinson, "Interaction of wide bandgap single crystals with 248 nm excimer laser radiation. V. The role of photoelectronic processes in the formation of a fluorescent plume from MgO," J. Appl. Phys. **81,** 1495-1504 (1997).

[10] K. H. Nwe, S. C. Langford, and J. T. Dickinson, "Interaction of wide-band-gap single crystals with 248-nm excimer laser irradiation. IX. Photo-induced atomic desorption from cleaved NaCl(100) surfaces," J. Appl. Phys. **98,** 013506 (2005).

[11] J. J. Shin, D. R. Ermer, S. C. Langford, and J. T. Dickinson, "The role of photoelectronic processes in the formation of a fluorescent plume by 248 nm laser irradiation of single crystal $NaNO_3$," Appl. Phys. A **64,** 7-17 (1997).

[12] T. Akiba, Y. Akimune, N. Hirosaki, and J. T. Dickinson, "Particle emission from Si_3N_4 surface by excimer laser radiation," Journal of Materials Science Letters **14,** 898-900 (1995).

[13] M. L. Dawes, W. Hess, Y. Kawaguchi, S. C. Langford, and J. T. Dickinson, "Laser-induced positive ion and neutral atom/molecule emission from single crystal $CaHPO_4{\cdot}2H_2O$: The role of electron beam induced defects," Appl. Phys. A **69,** S547-S522 (1999).

[14] R. Kelly, "On the dual role of the Knudsen layer and unsteady, adiabatic expansion in pulse sputtering phenomena," J. Chem. Phys. **92,** 5047-5056 (1990).

[15] H. S. Carslaw and J. C. Jaeger, *Conduction of Heat in Solids*, Second ed. (Oxford, London, 1959).

[16] D. W. Marquart, "An algorithm for least-squares estimation of nonlinear parameters," SIAM J. Appl. Math. **11,** 431-441 (1963).

[17] W. H. Press, B. P. Flannery, S. A. Teukolsky, and W. T. Vetterling, *Numerical Recipes in Pascal: The Art of Scientific Computing* (Cambridge University, Cambridge, 1989).

[18] H. Bracht, R. Staskunaite, E. E. Haller, P. Fielitz, G. Borchardt, and D. Grambole, "Silicon diffusion in sol-gel derived isotopically enriched silica glass," J. Appl. Phys. **97,** 046107 (2005).

[19] V. O. Altemose and S. S. C. Tong, "Evaporation from binary glasses by high temperature mass spectrometry," J. Non-Cryst. Solids **38-39,** 587-592 (1980).

[20] L. Huang and J. Kieffer, "Anomalous thermomechanical properties and laser-induced densification of vitreous silica," Appl. Phys. Lett. **89,** 141915 (2006).

[21] Y. S. Touloukian, R. W. Powell, C. Y. Ho, and M. C. Nicolaou, *Thermal Diffusivity*, Vol. 10 (Plenum, New York, 1973).

[22] J. Zhang, P. R. Herman, C. Lauer, K. P. Chen, and M. Wei, in *Laser Applications in Microelectronic and Optoelectronic Manufacturing VI*; *Vol. 4274*, edited by M. C. Gower, H. Helvajian, K. Sugioka, and J. J. Dubowski (SPIE, Belleview, WA, 2001), p. 125-132.

[23] E. Eva and K. Mann, "Nonlinear absorption phenomena in optical materials for the UV-spectral range," Appl. Surf. Sci. **109/110,** 52-57 (1997).

[24] K. Kurosawa, P. R. Herman, and W. Sasaki, "Radiation effects of vacuum ultraviolet lasers on silica glasses," Journal of Photopolymer Science and Technology **11,** 367-372 (1998).

[25] H. Hosono, Y. Ikuta, T. Kinoshita, K. Kajihara, and M. Hirano, "Physical disorder and optical properties in the vacuum ultraviolet region of amorphous SiO_2," Phys. Rev. Lett. **87,** 175501-1-4 (2001).

[26] K. Kajihara, Y. Ikuta, M. Hirano, and H. Hosono, "Power dependence of defect formation in SiO_2 glass by F_2 laser irradiation," Appl. Phys. Lett. **81,** 3164-3166 (2002).

[27] K. Kajihara, L. Skuja, M. Hirano, and H. Hosono, "Formation and decay of nonbridging oxygen hole centers in SiO_2 glasses induced by F_2 laser irradiation: In situ observation using a pump and probe technique," Appl. Phys. Lett. **79,** 1757-1759 (2001).

[28] V. Sulimov, P. V. Shushko, A. H. Edwards, A. L. Shluger, and A. M. Stoneham, "Asymmetry and long-range character of lattice deformation by neutral oxygen vacancy in α-quartz," Phys. Rev. B **66,** 024108 (2002).

[29] K. Kajihara, L. Skuja, M. Hirano, and H. Hosono, "Role of mobile interstitial oxygen atoms in defect processes in oxides: Interconversion between oxygen-associated defects in SiO_2 glass," Phys. Rev. Lett. **92,** 015504 (2004).

[30] S. O. Kucheyev and S. G. Demos, "Optical defects produced in fused silica during laser-induced breakdown," Appl. Phys. Lett. **82,** 3230-3232 (2003).

[31] R. Tohmon, H. Mizuno, Y. Ohki, K. Sasagane, K. Nagasawa, and Y. Hama, "Correlation of 5.0- and 7.6-eV absorption bands in SiO_2 with oxygen vacancy," Phys. Rev. B **39,** 1337-1345 (1989).

[32] W. J. Hehre, J. Uy, P. E. Klunzinger, and L. Lou, *A Brief Guide to Molecular Mechanics and Quantum Mechanical Calculations* (Wavefunction, Irvine, CA, 1998).

[33] L. Skuja, "Optically active oxygen-deficiency-related centers in amorphous silicon dioxide," J. Non-Cryst. Solids **239,** 16-48 (1998).

[34] M. Mizuguchi, L. Skuja, H. Hosono, and T. Ogawa, "F-doped and H_2-impregnated synthetic SiO_2 glasses for 157 nm optics," Journal of Vacuum Science and Technology B: Microelectronics and Nanometer Structures **17,** 3280-3284 (1999).

[35] J. H. Stathis and M. A. Kastner, "Photoinduced paramagnetic defects in amorphous silicon dioxide," Phys. Rev. B **29,** 7079-7081 (1984).

[36] K. M. Davis and M. Tomozawa, "Water diffusion into silica glass: structural changes in silica glass and their effect on water solubility and diffusivity," J. Non-Cryst. Solids **185,** 203-220 (1995).

[37] L. Zheng, J. C. Lambropoulos, and A. Schmid, "Molecular dynamics study of UV-laser-induced densification of fused silica. II. Effects of laser pulse duration, pressure, and temperature, and comparison with pressure-induced densification," J. Non-Cryst. Solids **351,** 3271-3278 (2005).

[38] C. M. Smith and N. F. Borrelli, "Behavior of 157 nm excimer-laser-induced refractive index changes in silica," J. Opt. Sci. Am. B **23,** 1815-1821 (2006).

[39] L. Skuja, K. Kajihara, Y. Ikuta, M. Hirano, and H. Hosono, "Urbach absorption edge of silica: reduction of glassy disorder by fluorine doping," J. Non-Cryst. Solids **345-345,** 328-331 (2004).

[40] S. C. Cheng, S. L. Schiefelbein, L. A. Moore, M. Pierson-Stull, C. M. Smith, and S. Sen, "Use of EELS to study the absorption edge of fused silica," J. Non-Cryst. Solids **352,** 3140-3146 (2006).

CHAPTER THREE

Interaction of vacuum ultraviolet excimer laser radiation with fused silica: III. Negative ion formation

Sharon R. George, S. C. Langford, and J. T. Dickinson*

Department of Physics and Astronomy, Washington State University, Pullman, WA 99164-2814

Abstract

We report mass- and time-resolved measurements of negative ions produced by exposing fused silica to 157-nm radiation at fluences below the threshold for optical breakdown. The principal observed negative ions are O^-, Si^- and SiO^-, in order of decreasing intensity. The peak in the negative ion time-of-flight signals occurs after the peak in the positive ion signal, and before the peak in the corresponding neutral atom or molecule signal. The negative ion intensities are strong functions of the degree of overlap between the positive ion and neutral atom densities. We propose that O^-, Si^- and SiO^- are created *after* the laser pulse, by electron attachment to the these neutral particles, and that the electrons participating in attachment events are trapped in the electrostatic potential of the positive ions.

1. Introduction

Particle emission can be a valuable probe of interactions between optical materials and laser radiation in the near-surface region. Synthetic fused silica is an important UV optical material with a band gap of 8.9 eV.[1] Although this is well above the 7.9 eV photon energy of the F_2 excimer, absorption due to disorder-related states in the band gap renders fused silica unsuitable for most optical applications at this photon energy. In companion papers, we describe measurements of positive ions (Si^+ and O^+)[2] and neutral atoms and molecules (O, Si and SiO)[3] emitted from fused silica during 157-nm laser irradiation at fluences well below the threshold for optical breakdown. We showed that positive ions can be emitted with several eV of kinetic energy from surface defect states by a combination of photoexcitation and photoionization processes. Neutral atoms and molecules are emitted by defect interactions along the surface; these defects are produced principally by the photo-induced cleavage of strained bonds.

In this work, we report mass-selected time-of-flight measurements on O^-, Si^- and SiO^- when fused silica is exposed to pulsed 157 nm radiation. These negative ions corresponding to the three neutral atoms and molecules previously detected from fused silica under comparable conditions.[3] We propose that the negative ions are produced *after* the laser pulse by electron attachment to neutral O and Si and SiO. The electrons participating in attachment processes are trapped in the positive electrostatic potential of emitted positive ions to produce a nearly neutral cloud of positive and negative charge (±charge cloud). The mutual electrostatic attraction between positive and negative charge allows for high electron densities inside the cloud, with much lower electron densities elsewhere. The peak negative ion densities appear where the corresponding neutral particle distribution overlaps the ±charge cloud. For instance, O^- is observed where the distribution of charged particles overlaps the neutral O distribution. The negative ion intensities are strong functions of the degree of overlap.

In previous work, we observed negative ions during the UV irradiation of alkali halides—also at fluences well below the threshold for optical breakdown; these emissions were attributed

to electron attachment to positive alkali *ions*.[4] In the alkali halides, the overlap between the charge cloud and neutral particles emitted from the surface is negligible. Given sufficient electron densities in the charge cloud, however, negative ions can be formed by a two-step process, where electron-ion attachment produces neutral particles, which are then converted to negative ions by a second attachment event. In fused silica, however, the overlap between neutral atoms/molecules and the charge cloud is significant, and negative ions are formed directly by electron attachment to the emitted neutral particles.

2. Experiment

Synthetic, UV grade (high-OH) fused silica rods from Heraus-Amersil (Suprasil 2) were cut into plates using a diamond saw and cleaned in ethanol. To modify the character and density of surface defects, some samples were abraded with 600-grit SiC sandpaper or polished to a 0.3-μm surface finish with alumina or diamond abrasives. Extensive deformation was provided on polished material by producing an array of indentations with a diamond scribe; care was taken to avoid fracture. Silica with low surface defect densities was prepared by annealing polished samples at 1100 °C for eight hours. Surfaces with relatively low densities of mechanically produced defects but relatively high fictive temperatures (high densities of strained bonds) were prepared by heating polished samples to 1400 °C for 10 minutes in a tube furnace and then dropping them into a beaker of room temperature, 3 M nitric acid.

To characterize the negative ion kinetic energies, the quadrupole mass-selected time-of-flight (TOF) signals were fit to functions representing the particle flux of ions with a one-dimensional Gaussian energy distribution with a mean kinetic energy E_0 and standard deviation σ. If these ions are emitted along the surface normal at time $t = 0$, their flux $I(t)$ at a detector mounted a distance d (= 0.28 m) from the sample at time t is given by:

$$I(t) = \frac{N_I m d^2}{\sqrt{2\pi}\,\sigma t^3} \exp\left\{\frac{-\left[E(t) - E_0\right]^2}{2\sigma^2}\right\} \quad , \qquad (1)$$

where N_I is the total number of detected ions and $E(t)$ [$= mv^2/2 = md^2/2t^2$] is the kinetic energy of an ion of mass m.

Samples were mounted on a translation stage directly in front of and normal to the axis of a UTI 100C quadrupole mass spectrometer (QMS). All experiments were performed in a vacuum chamber with a base pressure of about 3×10^{-7} Pa. 20-ns pulses of 157-nm laser radiation were provided by a Lambda Physik LPF200 laser (F_2 excimer) at a pulse repetition rate of 5 Hz. The beam was focused to a 0.16×0.05 cm^2 spot on the sample with a calcium fluoride lens. Ions exiting the mass filter were detected with a Channeltron electron multiplier (CEM) biased for the detection of negative ions and operated in the pulse-counting mode. The output of the detector was amplified, discriminated, and pulse counted over 200-ns intervals with an EG&G PARC 914P multichannel scalar. Unless otherwise noted, the signals presented below represent the average emission accompanying 200 successive pulses on the same spot. The acquisition of positive ion and neutral time-of-flight signals is described in Refs. 2 and 3.

Independent measurements of the positive and negative charge were made by monitoring the current collected by a metal disk mounted 10.5 cm from the sample along the surface normal. The plate was biased –18 V for detection of positive ions and +18 V for detection of electrons and negative ions.

3. Results and Discussion

3.1 Negative Ion Production

Negative ion time-of-flight signals. When the detector of our quadrupole mass spectrometer is biased to detect positive ions, we observe mass-selected time-of-flight signals corresponding to Si^+ and O^+ (28 amu/e and 18 amu/e, respectively).[2] We were surprised to see

mass-selected negative ion signals with the quadrupole detector biased to detect negative ions. Negative ion emission from the surface is not expected due to the positive surface charge that builds up during the laser pulse.[4] The resulting electric fields hinder the escape of negative ions. (Insulating surfaces typically emit more electrons than positive ions during the laser pulse. Many of these electrons return to the surface *after* the laser pulse, so that the net charge emitted per laser pulse is essentially zero.) Nevertheless, significant signals are observed at 16 amu/e (O^-) and 28 amu/e (Si^-), and weaker signals at 44 amu (SiO^-).

Typical O^-, Si^- and SiO^- time-of-flight signals acquired at a fluence of 2.4 J/cm^2 per pulse are shown in Fig. 1. The insets show the corresponding positive ion signals for O^+ and Si^+ acquired at comparable fluences. The O^- signal is typically an order of magnitude more intense than the Si^- signal. Weak signals at 44 amu (SiO^-) are also observed at the highest fluences employed in this work. We emphasize that these signals are generated at fluences well below the threshold for plume formation, where our mass resolution is typically ±2 amu.

In many systems, weak signals at mass 44 (here attributed to SiO^-) can be produced by interactions with CO_2—a common vacuum system contaminant. However, CO_2 has a negative electron affinity –0.6 eV[5] and therefore does not form a stable negative ion. The electron affinities of neutral O, Si, and SiO are +1.46 eV,[6] +1.38 eV,[7] and +0.038 eV (calculated)[8], respectively. The small positive electron affinity of SiO may contribute to the weakness of the SiO^- signal.

The dark lines in Fig. 1 show least-squares curve fits of Eq. (1) to the negative ion time-of-flight signals. [Equation (1) also provides reasonable fits to the positive ion time-of-flight signals acquired under comparable conditions.[2]] The mean kinetic energy of the O^- energy distribution derived from these fits is 2.0 ± 0.5 eV, with a corresponding full-width at half-maximum of about 0.7 eV. The Si^- energy distribution has a mean kinetic energy of 2.4 ± 0.5 eV and a full-width at half-maximum of about 3.8 eV. Although the uncertainties in the curve fit parameters derived from the weak SiO^- signals are large, the kinetic energy distribution appears to peak near 3.5 eV; the corresponding full width at half-maximum is nearly 6 eV. The mean

kinetic energies of each observed negative ion is well below the mean kinetic energies of the observed positive ions: 8-9 for Si^+ and 4 eV for O^+.[2]

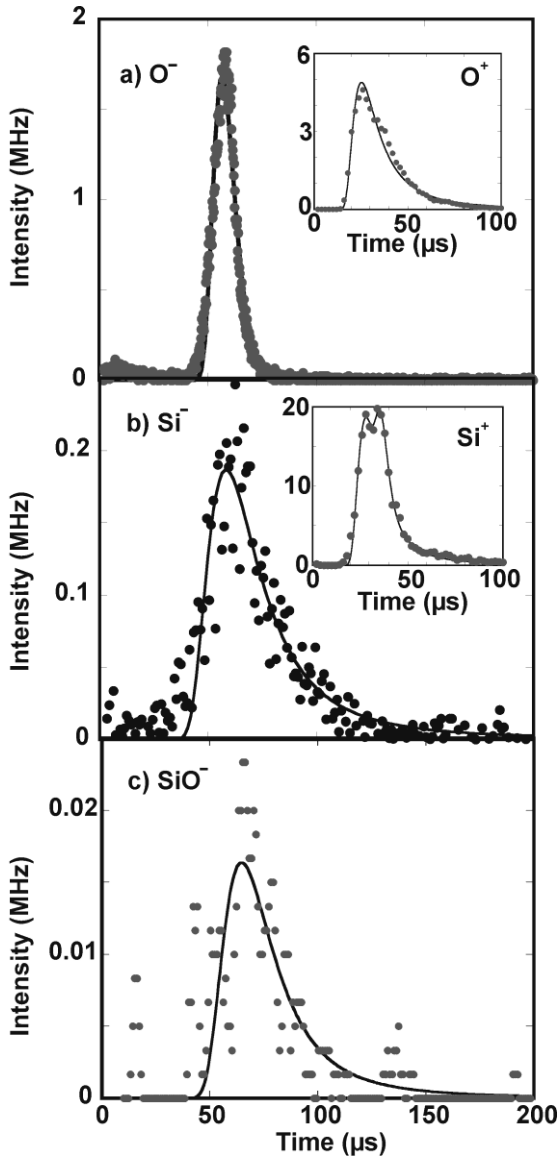

Fig. 1. Time-of-flight signals corresponding to (a) O^- (b) Si^- and (c) SiO^- during exposure of as-cut fused silica to 157-nm radiation at a fluence of 2.4 J/cm^2 per pulse. The insets show the positive ion counterparts for O and Si acquired under comparable conditions.

In a previous study of alkali halides exposed to pulsed 248-nm radiation, we showed that negative ions are formed by electron attachment to previously emitted particles.[4] Here, the

electrons that are available for attachment processes are confined to a localized cloud of positive ions (principally O^+ and Si^+) and negative charge (principally electrons), where the electrons are electrostatically coupled to the positive ions.[4,9-11] We propose that the negative ions observed when fused silica is exposed to 157-nm radiation are formed when electrons traveling with a similar ±charge cloud attach to neutral atoms and molecules from the surface. In this case, the spatial overlap between this ±charge cloud and the neutral particles is a critical issue,[4] addressed below.

Factors influencing intensity. Mechanical and thermal treatments have important effects on the negative ion intensities. Figure 2 shows the relative intensities of the O^- signals from treated fused silica surfaces at a fluence of 1.6 J/cm^2 per pulse. Treatments expected to increase the density of surface defects (relative to the as-cut material), such as abrading and indenting, increase the O^- intensity. Conversely, treatments expected to decrease the density of surface defects (relative to the as-cut material), such as polishing and annealing, decrease the O^- intensity. Annealing in particular virtually eliminates the O^- signal. These treatments have similar, but weaker, effects on the positive ion intensities measured under comparable conditions.[2]

In previous work on the same material under comparable conditions of 157-nm laser exposure, we have shown that the above mechanical treatments have strong effects on the positive ion intensities[2] but almost *no* effect on the emission of neutral atoms and molecules.[3] In contrast, quenching dramatically increases the neutral emissions from polished samples,[3] but has little effect on the emission of positive ions. Although quenching does increase the O^- intensity from polished silica, as shown in Fig. 2, this increase is much smaller than the increase in neutral O intensity. As discussed below, the proposed mechanism for negative ion formation leads us to expect especially strong correlations between the negative and positive ion intensities. The correlation between negative ion and neutral intensities should be weaker, as observed.

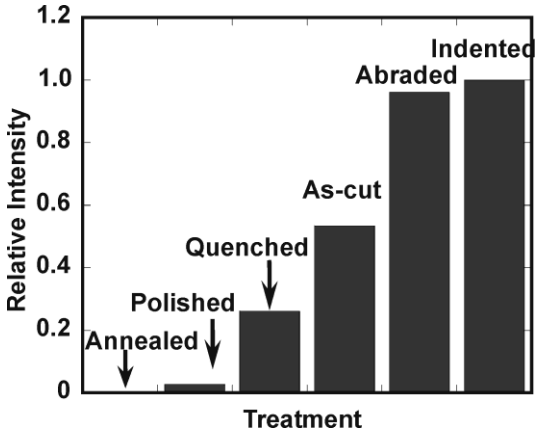

Fig. 2. Total O^- intensities from fused silica with six different surface treatments at a fluence of 1.6 J/cm^2 per pulse.

The negative ion intensities decrease gradually during prolonged irradiation, as shown in Fig. 3 for O^- from as-cut silica at 2.5 J/cm^2. Nevertheless, negative ion emission continues at low levels for thousands of pulses at this fluence, as shown in the inset of Fig. 3. After 8000 pulses, the negative ion intensity has dropped to 2% of the initial intensity. Similar, but much smaller, clean-up effects are observed in the neutral[3] and positive ion[2] intensities under comparable conditions. For instance, similar exposures typically reduce the positive ion intensities to 10% of their initial values. Neutral intensities are reduced even less, plateauing at about 70% of their initial values. Again, this pattern is consistent with the expected strong correlation between the negative and positive ion intensities.

Angular distribution of ion emission. We were initially surprised to observe significant negative ion signals under the conditions of this work, and doubly surprised at their apparent intensity. For instance, the O^- ion signal in Fig. 1(a) corresponds to about 30 counts per laser pulse, whereas the corresponding O^+ signal corresponds to about 120 counts per pulse. Given the difficulty of producing negative ions, we expected the positive ions to outnumber the negative ions by some orders of magnitude. The situation is ameliorated somewhat by the relative intensity of the Si^+ signal—about 300 counts per pulse under these conditions.

Nevertheless, it appears that our mass-selected time-of-flight signals under-represent the positive ion intensities relative to the negative ion intensities.

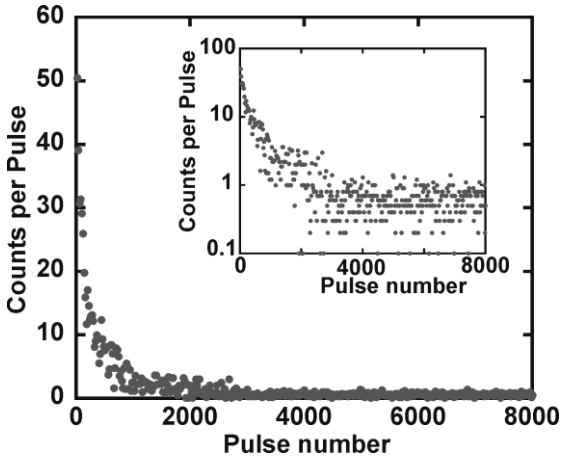

Fig. 3. O^- intensity as a function of laser exposure (total number of laser pulses) from as-cut fused silica during prolonged exposure to 157-nm radiation at a fluence of 2.5 J/cm^2. The inset shows the same data on a semi-log plot.

Figure 4 shows the normalized angular distributions for Si^+ and O^- ion from as-cut fused silica between 0° and 40° as measured from the surface normal. (Si^+ is the most abundant positive ion, and O^- is the most abundant negative ion.) The Si^+ distribution is broad, roughly $\cos^3\theta$. We note that ions ejected as the result of electronic transitions are often emitted along the bonding direction.[12] In the case of crystalline ionic materials, the corresponding ion angular distribution is often sharply peaked in the direction normal to the surface, as in MgO.[13] The relatively broad angular distribution for Si^+ is consistent the broad distribution in bond angles on the amorphous silica surface.

The O^- ion angular distribution, however, is sharply peaked in the direction normal to the surface. The angular distribution is roughly $(\cos\theta)^{236}$. This narrow angular distribution is *not* consistent with emission from an amorphous surface. As discussed below, we believe that these negative ions are formed by gas phase electron attachment to neutral oxygen atoms. This sharp

angular distribution suggests that O^- production is highly constrained, perhaps to a small region directly above the center of the laser spot.

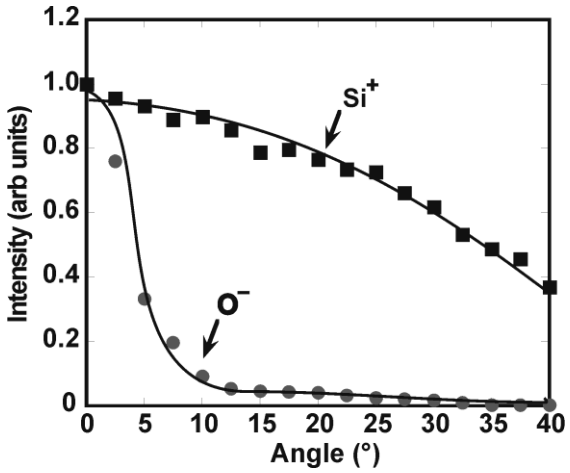

Fig. 4. Si^+ and O^- intensities from as-cut fused measured at different angles from the surface normal at a fluence of 2.2 J/cm^2. The dark lines show curve fits to functions of the form $\cos^N(\theta)$, where $N = 3$ for Si^+ and $N = 236$ for O^-.

Since the O^- angular distribution is sharply peaked in the direction toward our detectors, a relatively high fraction of the emitted O^- is detected. As viewed from the laser spot, the aperture of our mass filter subtends an angle of 1.1° with respect to the surface normal. If the angular distributions are axially symmetric about the surface normal, the geometrical collection efficiency for O^- is about 4%. The corresponding geometrical collection efficiency for Si^+ is about 0.07%. Thus the Si^+ counts outnumber the O^- counts by over two orders of magnitude—consistent with the expected difficulty of producing O^-. We note that the net charge removed from the sample per laser pulse must be near zero. Since Si^+ is the most intense positive ion and O^- is the most intense negative, we expect that that the great majority of negative charge is removed from the sample as electrons.

Total ±charge measurements. Electron attachment requires high electron densities. As mentioned above, the number of electrons emitted from the surface *during* the laser pulse can far exceed the number of positive ions. However, most of these electrons will return to the surface

soon after the laser pulse. To maintain charge neutrality, the total number of electrons that permanently escape the insulating surface will (to a good approximation) equal the number of emitted positive ions. Since typical electron velocities are much higher than typical positive ion velocities, the fastest electrons outrun the positive ions and leave behind a region of positive potential that traps the remaining electrons. The end result is a nearly neutral (but slightly positive) cloud of positive ions and electrons traveling away from the surface. The electrons weave rapidly back and forth through the central positive region at high velocities. We refer to the resulting cloud of charged particles as a ±charge cloud. It behaves much like an expanding ball of low-density plasma moving away from the surface.[14,15]

The dominant contribution to the negative charge in a nearly neutral ±charge cloud is typically made by electrons. The large excess of positive ions (principally Si^+) over negative ions (principally O^-) inferred from the angular distribution measurements support the hypothesis that electrons greatly outnumber the negative ions. Further evidence for the nature of the negative charge in the ±charge cloud is provided by measuring the positive and negative charge signals (fluxes) with a CEM mounted behind a pair of grids 6.3 cm from the surface during irradiation at a fluence of 560 mJ/cm^2. The outer grid was grounded to ensure that the incoming ±charge cloud was not affected by the voltages applied to the CEM and the inner grid. The positive charge signal was measured with both the grids grounded; a +10 V bias was applied to the inner grid for the negative charge measurements. The resulting signals, normalized to a common intensity at time t=8 μs after the laser pulse, are shown in Fig. 5..

The positive charge signal in Fig. 5(a) shows a simple peak about 8.2 μs after the laser pulse. The most intense positive ion identified in previous work is Si^+.[2] These Si^+ signals display two peaks, with mean kinetic energies of 8.2 and 8.6 eV, respectively. The peak in the positive charge signal at 8.2 μs corresponds closely to these Si^+ signals: at kinetic energies of 8.2–8.6 eV, Si^+ travels 6.1–6.3 cm in 8.2 μs.

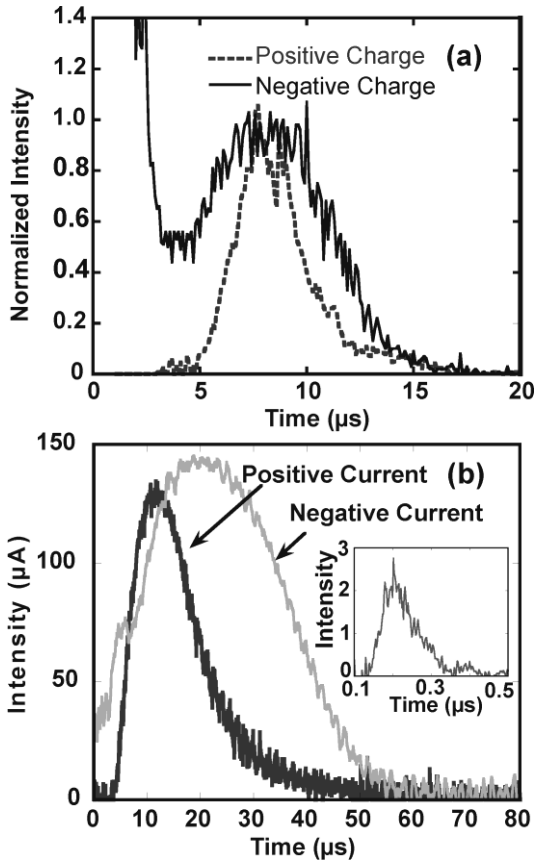

Fig. 5. (a) Positive and negative charge time-of-flight signals detected from polished fused silica with an appropriately biased CEM, mounted 6.3 cm from the sample surface behind two grids, at a fluence of 560 mJ/cm^2. (b) Current delivered to a bare metal plate, mounted 12.5 cm from the sample, from polished fused silica at a fluence of 2.3 J/cm^2; the positive and negative signals were detected with plate biases of –18 V and +18 V, respectively. The inset shows the signal due to fast electrons, detected with an electron multiplier mounted at the same position as the plate.

The negative charge signal in Fig. 5(a) is extremely intense at times less than 3 μs. This signal is an artifact due to photoelectrons emitted from the grid structures during the laser pulse. Significant here is the peak in the negative charge signal near 8 μs, which coincides nicely with the positive charge peak. If negative ions made up a significant fraction of this negative charge, we would expect a component of negative charge that behaves like more the O^- signal in Fig. 1(a). A peak due to 2.0 eV O^- would appear at 12.5 μs in Fig. 5(a)—well *after* the positive charge peak. This supports our expectation that the electrons provide almost all the negative charge in the ±charge cloud itself.

The slow negative charge peak in Fig. 5(a) is broader than the positive charge peak, consistent with electrons weaving back and forth through the positive potential of the positive charge. These electrons turn around *outside* the region of dense positive charge, and comprise the negative portion of the plasma Debye sheath.[16] The position and width of the slower negative charge in Fig. 5(a) are consistent with large numbers of high velocity electrons weaving back and forth through the net positive charge cloud. This motion makes it difficult to infer the actual electron density as a function of time.

To estimate the magnitude of the positive and negative charge in the ±charge cloud, a bare (unshielded) metal plate was mounted 12.5 cm from the sample surface. The plate was biased +18 V for the detection of negative charge and –18 V for the detection of positive charge. The resulting charge signals appear in Fig. 5(b). The time-behavior of the positive charge signal is consistent with the charge measurements above and with the mass-selected time-of-flight measurements for Si^+ and O^+ in Fig. 1(a).[2] For instance, the positive current in Fig. 5(b) peaks near 12 μs, which corresponds to a peak ion time-of-flight of 32 μs (measured 28 cm from the sample), shown in inset of Fig. 1(a). These measurements indicate that the positive ions move with nearly constant velocities—consistent with nearly ballistic (straight-line) trajectories.

Since the positive ion trajectories are almost ballistic, the collector is expected to collect all the positive ions with trajectories that intersect the plate. The plate subtended an angle of ±10° with respect to the surface normal; given the $\cos^3\theta$ angular distribution from Fig. 4, this plate would collect about 4% of the positive ions. Thus the total collected positive charge of about 2 nC corresponds to a total emitted charge of about 50 nC. Assuming that the ±charge cloud is nearly neutral,[17] this same value is a reasonable estimate for the total negative charge (predominately electrons) in the cloud.

The negative current signal in Fig. 5(b) is more complex. Some negative charge reaches the plate within microseconds of the laser pulse. Fast time-scale measurements (shown in the inset) made with a CEM mounted at the same position show that the first negative charge reaches the plate about 200 ns after the laser pulse. This charge travels directly from the sample to the

plate at typical electron velocities. At later times, a shoulder on the negative current signal appears near the onset of the positive current signal. As in Fig. 5(a), we attribute this shoulder to electrons coupled to the positive ions, weaving back and forth at high velocities through the net positive charge cloud. These electrons turn around just outside the edge of the positive ion distribution, so that the electron density there is relatively high. The electrons in this region (the Debye sheath) shield the interior of the charge cloud from applied electric fields.[16]

The back-and-forth motion of the electrons through the charge cloud (and the absence of nearby metal structures that would collect this charge elsewhere) allows for the detection of electrons from remote parts of the charge cloud long after the main body of positive ions has passed the detection plate. Thus the negative charge signal in Fig. 5(b) remains intense for tens of microseconds after the peak in the positive charge signal. The total negative charge collected at this fluence is over 4 nC. It is unlikely that we have collected all the negative charge under these conditions, but the complicated electron trajectories do not allow for a quantitative assessment. The difficulty of charge collection from plasmas using Langmuir-type collectors is reviewed in Ref. 18.

Electrons traveling in the plasma-like ±charge cloud are available for attachment with any neutral particles that occupy the same region of space. Since the electrons are electrostatically coupled to the positive ions, and since the positive ions have relatively simple trajectories, we use the positive ion distribution as a proxy for the electron distribution. A good estimate of the overlap between the charge cloud and the neutrals can be obtained by plotting the time-of-flight signals for the positive ions and the neutral particles at the same position. To do this, we must account for the different behavior of ions and neutral particles in our mass filter. The (ionized) neutral particles pass through the mass filter with 15 eV kinetic energy, while positive ions pass through the filter with whatever kinetic energy they have when they enter the mass filter. To obtain the signal as it would have been measured at the quadrupole ionizer, we subtract the time required for each particle to pass through the mass filter. In the case of the positive ions, this time depends on the ion kinetic energy.

Figure 6 shows neutral and positive ion time-of-flight signals projected to the position of the center of quadrupole ionizer, 10.5 cm from the sample surface. The normalized positive ion signal in Fig. 6 shows substantial overlap with the normalized neutral O and neutral Si signals at the quadrupole ionizer. Figure 6 also shows the normalized O^- time-of-flight signal projected to the same position. The O^- signal appears where the positive ions and the neutral O show the highest degree of overlap. Because the electrons are constrained to move with the positive ions in the ±charge cloud, this is consistent with the production of O^- by electron attachment to neutral O. The weaker overlap between the positive ions and the slower neutral Si particles accounts for the weakness of the Si^- signal relative to O^-. Finally, the overlap between the positive ions and the neutral SiO distribution is almost negligible. As noted above, the SiO^- signal is quite weak and observed only at the highest fluences employed in this work.

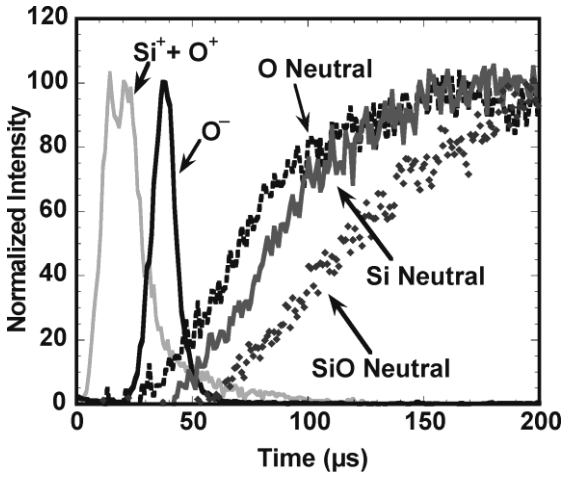

Fig. 6. Projected time-of-flight signals for Si^+, O^+, O^-, and neutral O, Si and SiO from fused silica at a position 10.5 cm from the sample. Each signal is normalized to a common peak intensity. The original signals were acquired at fluences near 2.2 J/cm^2.

We propose that negative ions are produced where the positive ion and neutral signals overlap: electrons moving with the positive ions (in the ±charge cloud) attach to neutral atoms in the region of overlap, where both electron and neutral densities are significant. Only the fastest neutral particles appear in the overlap region. Conversely, only the slowest ions appear in the

overlap region. Thus the negative ion kinetic energies are well above the average neutral particle kinetic energies, and well below the average positive ion kinetic energies. Below, we provide a more quantitative account of O^- production in terms of the expected attachment rate and particle densities.

3.2 Electron attachment

As noted above, the emission of negative ions directly from the surface during laser exposure is not expected due to the net positive surface charge that develops during the laser pulse.[4] Because of its high intensity, we focus our discussion on O^- production. During electron irradiation, most surfaces charge negative and negative ions (including O^-) are often detected. For instance, O^- is produced during the electron irradiation of oxidized silicon.[18,19] Negative oxygen ions can also be produced by dissociative electron attachment to molecular O_2; in crossed beam experiments with 8 eV electrons, Chantry *et al*. observed 2.2 eV O^- ions produced by dissociative attachment.[20] O^- is similarly produced when O_2 molecules are adsorbed onto metal surfaces and exposed to energetic electrons.[21,22]

Negative atomic ions can also be produced in the gas phase by electron attachment to neutral atoms.[23] At low particle densities, electron-neutral attachment is mostly radiative: the excess kinetic energy of the attaching electron is carried away as electromagnetic radiation. In the case of atomic oxygen, however, radiative attachment is hindered by its exceptionally low polarizability. Under the conditions of this work, O^- production is dominated by collisional attachment, where the excess kinetic energy of the attached electron is carried away by a second electron. This process also readily allows for momentum conservation. For O^- production, collisional attachment can be described in terms of the reaction:

$$O° + e^- + e^- \rightarrow O^- + e^- \quad . \qquad (2)$$

This reaction produces O^- at a rate proportional to the product of the neutral O density, [O°], and the square of the electron density, $[e^-]^2$:

$$\frac{d[O^-]}{dt} \propto [O°][e^-]^2 \quad . \tag{3}$$

Measurements over the range of fluences probed in this work indicate that the functional forms of the particle distributions in space and time are weak functions of fluence. Therefore we expect the total intensities to obey a relation similar to Eq. (3). That is, we expect the total O^- intensity to be proportional to the product of the O° intensity and the square of the electron intensity, where we equate the electron intensity to the positive ion intensity. Although the absolute intensities are difficult to determine, the same trend should appear in the fluence dependences of the particle intensities. Figure 7(a) shows the fluence dependence of the O^- intensity from as-cut silica on a log-log scale. The O^- intensity varies roughly with the 5^{th} power of fluence, while the O° intensity in Fig. 7(b) is roughly proportional to the 1^{st} power of fluence. The intensity of the most intense positive ion (Si^+) is proportional to the $1.7^{th} \approx 2^{nd}$ power of fluence under comparable conditions.[2] To a reasonable approximation, the fluence dependence of the O^- intensity is proportional to product of the fluence dependence of the O° intensity and the square of the fluence dependence of the Si^+ intensity: $5 = 1 + 2^2$. Thus the fluence dependences of the particle intensities are consistent with negative ion production by collisional electron attachment.

O^- production is fastest when and where the product in Eq. (3) is maximized. This requires substantial spatial and temporal overlap between the electron and the neutral particle densities. Since we believe the electrons are traveling with the positive ions in a nearly neutral ±charge cloud, we represent the electron distribution by the positive ion distribution. Only the slowest ions will overlap the neutral particle distribution, so we assume that the electrons

available for attachment travel with the heavier (and therefore slower) Si^+ ions. Thus we require spatial overlap between Si^+ and neutral O.

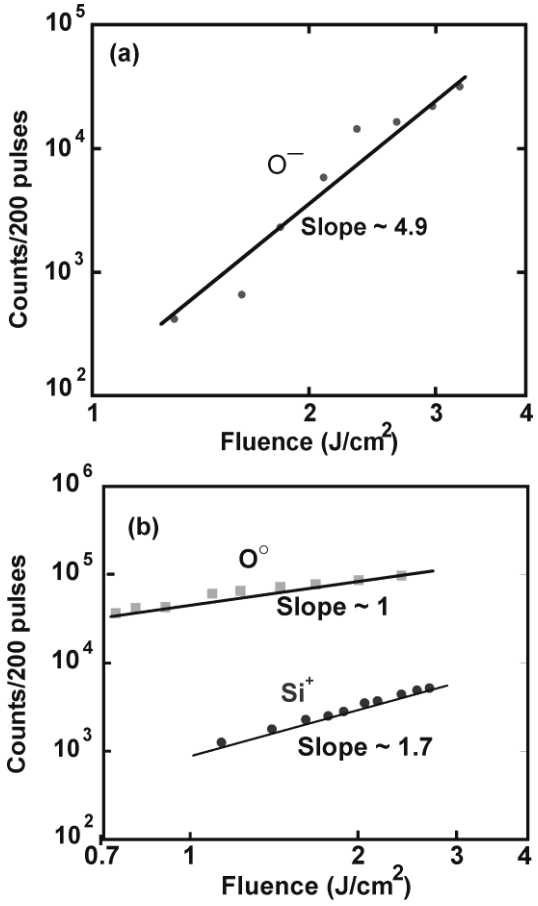

Fig. 7. (a) Fluence dependence of the O^- intensity from as-cut fused silica, plotted on a log-log scale. (b) Fluence dependences of the most intense positive ion (Si^+) and neutral O intensities from as-cut fused silica.

To assess the degree of overlap between the ±charge cloud and the atomic O, we transformed the equations describing our experimental time-of-flight distributions to spatial particle density functions. For instance, the energy distribution of the positive ions is well described by a Gaussian function in energy. It is convenient to express the energy distribution as a derivative of a cumulative energy distribution function, $n_G(E)$, giving the total number of ions with kinetic energies less than E:

$$\frac{dn_G}{dE} = \frac{N_I}{\sqrt{2\pi}\sigma} \exp\left(-\frac{(E - E_0)^2}{2\sigma^2} \right), \tag{4}$$

where $E=mv^2/2$ (where v is the ion kinetic energy) and N_I is the total number of ions emitted. The ion time-of-flight measurements yield the ion *flux* at the CEM, *I(t)* in Eq. (1). The ion flux is readily expressed as the time derivative of $n_G[E(t)]$. For a delta function source of ions (in both space and time), the ion energy measured a distance d from the source is $E = (m/2)(d/t)^2$, and

$$I_G(t) = \frac{dn_G}{dt} = \frac{dn_G}{dE}\frac{dE}{dt} = \frac{N_I}{\sqrt{2\pi}\sigma}\left|\frac{-md^2}{t^3}\right| \exp\left[-\frac{(E - E_0)^2}{2\sigma^2} \right] \quad , \tag{5}$$

where we take the absolute value to ensure a positive flux, despite the fact that increasing the kinetic energy decreases the time of flight. The mean kinetic energy E_0 and the standard deviation σ of the energy distribution were determined by fitting *I(t)* to the measured ion time-of-flight signals. The mean kinetic energies for the two observed Si^+ peaks are 8.2 and 8.6 eV, respectively, with $\sigma = 2.5$ eV for both peaks.[2]

Although the Si^+ angular distribution is rather broad ($\approx \cos^3\theta$), simple point-source models severely overestimate the early ion densities as the ions diverge away from the source. Physically, the divergence at short times is avoided because the source is not point-like: ions are generated over the entire area of the laser spot. To avoid this divergence, we treat the ion trajectories in one-dimension only, as if ions were generated uniformly over the laser spot and travel along the surface normal. Neither assumption holds in the strict sense, but they allow for well behaved analytic solutions. For a one-dimensional model, we replace d in Eq. (5) with x, the position coordinate along the surface normal. The number of ions per unit distance along the surface normal is given by the derivative of $n_G[E(x)]$ with respect to x. Dividing this by the area of the laser spot $A = 0.008$ cm^2 yields the corresponding three-dimension ion density:

$$\frac{dn_G}{dV_S} = \frac{1}{A}\frac{dn_G}{dE}\frac{dE}{dx} = \frac{N_I\, m\, x}{\sqrt{2\pi}\,\sigma A t^2}\exp\left\{\frac{-\left[\left(\frac{mx^2}{2t^2}\right) - E_0\right]^2}{2\sigma^2}\right\} \quad . \tag{6}$$

where $\Delta V_S \approx \Delta x \Delta y \Delta z$ corresponds to a differential volume in three-space.

To describe the distribution of neutral O as a function of time after the laser pulse, we use the Maxwell-Boltzmann distribution for effusive particles. In a coordinate system with the laser spot at the origin and the sample surface normal directed along the *x*-axis, the Maxwell-Boltzmann *velocity* distribution for effusive particles is given by:

$$\frac{n_{MB}(v_x, v_y, v_z)}{dV_V} = \frac{2N_O x}{\pi t}\left(\frac{m}{kT}\right)^2 \exp\left[\frac{-m(v_x^2 + v_y^2 + v_z^2)}{2kT}\right] \tag{7}$$

where $n_{MB}(v_x,v_y,v_z)$ is the cumulative velocity distribution and $\Delta V_V \approx \Delta v_x \Delta v_y \Delta v_z$ is a volume in velocity space centered on (v_x,v_y,v_z); N_O is the total number of particles emitted, and T is the effective temperature of the Maxwell-Boltzmann distribution. The corresponding density distribution is given by transforming the velocity space volume to a real space volume $\Delta V_S \approx \Delta x \Delta y \Delta z$. For a delta-function source at the origin in space and time, $v_x = x/t$, $v_y = y/t$, and $v_z = z/t$. This is related to the velocity distribution by the Jacobian of the coordinate transformation between velocity and position, or $(dv_x/dx)(dv_y/dy)(dv_x/dx) = t^{-3}$.

$$\frac{n_{MB}(x,y,z)}{dV_S} = \frac{n_{MB}(v_x, v_y, v_z)}{dV_V}\det\left|\frac{\partial V_{Vi}}{\partial V_{Sj}}\right| = \frac{2N_O x}{\pi t^4}\left(\frac{m}{kT}\right)^2 \exp\left[\frac{-m(v_x^2 + v_y^2 + v_z^2)}{2kT}\right] \tag{8}$$

At the position of our detector (the quadrupole ionizer, where $x >> y, z$) $v_y \approx v_z \approx 0$. In the spirit of a one-dimensional model, we make the same assumption for the neutral particle density near the laser spot. Then

$$\frac{n_{MB}(x,y,z)}{dV_S} = \frac{2N_O x}{\pi t^4}\left(\frac{m}{kT}\right)^2 \exp\left[\frac{-mx^2}{2kTt^2}\right] \quad . \tag{9}$$

This expression was incorporated into a more complex model of the neutral emission from fused silica in Ref. 3, where we showed that neutral emission continued for many microseconds after the laser pulse. However, only the fastest neutral particles emitted during the laser pulses will overlap the ±charge cloud described above. These can be described by fitting the leading edge of the O time-of-flight signal in Fig. 6 to Eq. (9), which yields T = 1400 K.

The overlap between the ±charge cloud, the fast neutral O, and the resulting O^- can be assessed by plotting spatial density functions for each species: Eq. (6) for positive and negative ions and Eq. (9) for neutral particles. Figure 8(a) shows the three density distributions plotted as a function of distance x from the sample at time t = 100 ns after the laser pulse. The peak in the projected O^- density at this time coincides convincingly with the region of maximum overlap for neutral O and Si^+.

A more quantitative picture of how the attachment rate varies with position is given by plotting the product $[O]\times[e^-]^2$, again at time t = 100 ns after the laser pulse, shown in Fig. 8(b). Given the approximations in our model, the position and shape of the $[O]\times[e^-]^2$ function corresponds well with the projected spatial O^- density at the same time, shown by the dashed line in Fig. 8(b). In particular, this product accounts for the observed narrowness of the O^- time-of-flight peak relative to the positive ion peaks. The good agreement between the transformed O^- density and the projected attachment rate supports our contention that O^- is produced by collisional attachment to neutral O atoms.

The functional dependence of the attachment rate on the neutral and ion densities ($[O]\times[e^-]^2$) implies that the negative ion intensities will depend more strongly on factors that increase the electron density than on factors that increase the neutral intensity. As noted above, treatments that increase the positive ion intensities (abrading, indenting) increase the negative ion intensities more than treatments that increase the neutral intensities (quenching).

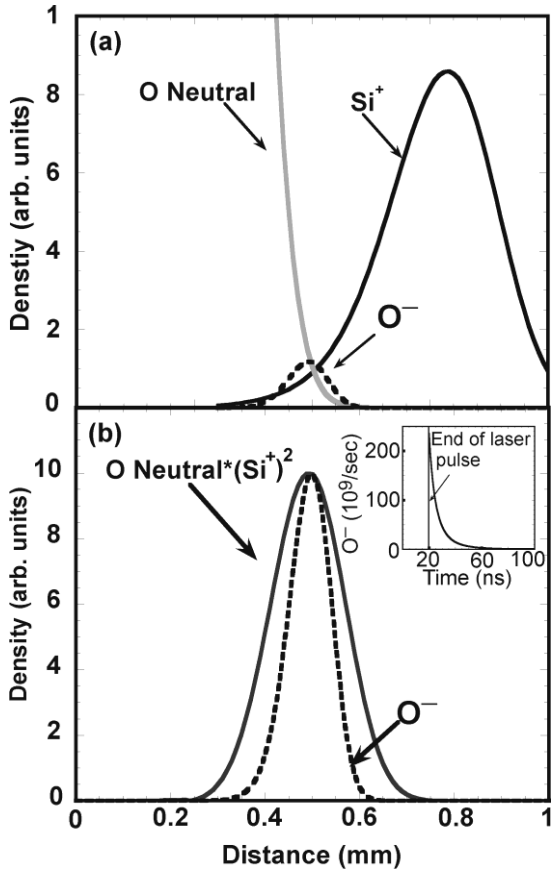

Fig. 8. (a) Projections of the fast neutral O° density ([O°], gray line), the square of the Si^+ ion density ($[Si^+]^2$, dark line), and the O^- density ($[O^-]$, dashed line) as a function of distance from the sample surface at time t = 100 ns after the laser pulse. (b) Projected O^- density (dashed line) and relative attachment rate (dark line, proportional to $[O]\times[Si^+]^2$) at time t = 100 ns after the laser pulse, normalized to a common peak magnitude. The original signals were acquired at fluences near 2.4 J/cm^2. The inset in (b) shows the integral of Eq. (10) over $0 < x < \infty$ as a function of time, which corresponds to the total number of O^- ions produced per unit time.

This functional dependence accounts for some of the difference between the angular distributions of the negative and positive ion signals in Fig. 4. Negative ion formation varies with the *square* of the positive ion density, and the square of a peaked spatial distribution is normally narrower than the original spatial distribution. However, the O^- distribution is much

narrower than one would expect on the basis of this effect alone. We suspect that the small net positive charge of the ±charge cloud helps prevent the radial expansion of the O^- distribution.

Soon and Kunc have estimated the collisional attachment rate for neutral oxygen to be $\sigma_{Attach} \approx 10^{-30}$ cm^6/s at electron temperatures between 1000 and 8000 K.[24] A quantitative estimate of the local change in O^- density per unit time can be derived by the product $[O]\times[e^-]^2$ and this cross section. Thus we expect

$$\frac{d[O^-]}{dt} = \sigma_{Attach}\frac{dn_{MB}}{dV_S}\left(\frac{dn_G}{dV_S}\right)^2 = \frac{\sigma_{Attach}N_O N_I^2 x^3}{2\pi^2 A^2 \sigma^2 t^8}\left(\frac{m^2}{kT}\right)^2 \exp\left[\frac{-mx^2}{2kTt^2}\right]\exp\left\{\frac{-\left[\left(\frac{mx^2}{2t^2}\right)-E_0\right]^2}{\sigma^2}\right\} \quad (10)$$

where all the parameters except the number of oxygen atoms emitted during the laser pulse, N_O, the total number of positive ions N_I, and the area of the laser spot A, are taken directly from curve fits. By calibrating our quadrupole, we estimate that 10^{11} O atoms are emitted per pulse under these conditions. Of these, we expect that roughly 10% are emitted during the laser pulse, so $N_O \approx 10^{10}$. Above we estimate the total positive charge in the ±charge to be about 50 nC, which corresponds to $N_I \approx 3 \times 10^{11}$.

The total number of O^- ions produced per unit time is given by the integral of Eq. (10) over the volume where the particle densities are significant. Since we have assumed that ion motion is principally normal to the surface, this volume is bounded in two dimensions by the area of the laser spot. In the inset of Fig. 8(b), we show the integral of Eq. 10 over $0 < x < \infty$ as a function of time, which corresponds to the total number of O^- ions produced per unit time. Negative ion production is essentially complete 100 ns after the laser pulse.

Integrating Eq. (10) a second time over time yields the total number of ions per laser pulse. Equation (10) is not well behaved in the limit as $t \rightarrow 0$, where the assumption of a delta function source in time breaks down. Emission takes place on time scales comparable to the

duration of the laser pulse, about 20 ns. Integrating over times 20 ns < t < ∞, the expression predicts the production of 1700 negative ions per laser pulse.

As noted above, we detect about 120 O^- per laser pulse under these conditions, and (correcting for angular distribution) we expect that a total of 3000 O^- are actually produced. In view of the uncertainties involved, the agreement is fortuitous. A more complete description of negative ion production would require a careful account of the laser beam profile. The laser employed in this work has a Gaussian beam profile, and the maximum fluence at the center of the laser spot is significantly higher than the average fluence over the nominal area. Since negative ion production is a nonlinear function of fluence, the increased production in high fluence regions would (much) more than compensate for the decreased production in lower fluence regions.

4. Summary and Conclusions

O^- and Si^- are observed when fused silica is exposed to 157-nm radiation—even at fluences well below the threshold for optical breakdown. At the highest fluences employed in this work, we also observe SiO^-. Since the surface charges positively during the laser pulse, it is quite unlikely that these negative ions are emitted directly from the sample. We attribute negative ion formation to electron attachment to neutral atoms and molecules well after emission. The participating electrons are strongly coupled to positive charge emitted during the laser pulse to form a plasma-like cloud of positive and negative charge. This coupling allows for high electron densities where the charge cloud and the neutral particles overlap. The weakness of the accompanying SiO^- signal is consistent with the poor overlap between the distribution of the slower moving neutral SiO molecules and the faster ±charge cloud.

Even at fluences well below the threshold for breakdown, the electron densities in ±charge clouds produced by UV laser radiation are often sufficient to form negative ions by electron attachment.[4] At higher particles densities, attachment processes can control the decay of

electron and positive ion densities as a function of time. The evolution of charge particle densities can have important implications in applications of laser ablation to thin film deposition and chemical analysis. Yet many of the relevant processes of particle generation and interactions are more easily isolated and characterized under less extreme conditions. These processes must be understood before we can reliably predict the effects of changes in process variables in applications of laser ablation to the synthesis and analysis of novel materials and structures.

Acknowledgment

This work was supported by the Department of Energy under Contract Number DE-FG02-04ER-15618.

References

[1] T. H. DiStefano and D. E. Eastman, "The band edge of amorphous SiO_2 by photoinjection and photoconductivity measurements," Solid State Commun. **9,** 2259-2261 (1971).

[2] S. R. George, J. A. Leraas, S. C. Langford, and J. T. Dickinson, "Interaction of vacuum ultraviolet excimer laser radiation with fused silica: I. Positive ion emission," J. Appl. Phys. **107,** 033107 (10) (2010).

[3] S. R. George, S. C. Langford, and J. T. Dickinson, "Interaction of vacuum ultraviolet excimer laser radiation with fused silica: II. Neutral atom and molecule emission," J. Appl. Phys. **107,** 033108 (10) (2010).

[4] K. Kimura, S. C. Langford, and J. T. Dickinson, "Interaction of wide-band-gap single crystals with 248-nm excimer laser radiation. XII. The emission of negative atomic ions from alkali halides," J. Appl. Phys. **102,** 114904 (2007).

[5] R. N. Compton, P. W. Reinhardt, and C. D. Cooper, "Collisional ionization of Na, K, and Cs by CO_2, COS, and CS_2: Molecular electron affinities," J. Chem. Phys. **63,** 3821-3827 (1975).

[6] D. M. Neumark, K. R. Lykke, T. Andersen, and W. C. Lineberger, "Laser photodetachment measurement of the electron affinity of atomic oxygen," Phys. Rev. A **32,** 1890-1892 (1985).

[7] H. Hotop and W. C. Lineberger, "Binding energies in atomic negative ions: II," Journal of Physical and Chemical Reference Data **14,** 731-750 (1985).

[8] G. L. Gutsev, P. Jena, and R. J. Bartlett, "Two thermodynamically stable states in SiO2 and PN2," Phys. Rev. A **58,** 4972-4974 (1998).

[9] S. C. Langford, L. C. Jensen, J. T. Dickinson, and L. R. Pederson, "Negative charge emission due to excimer laser bombardment of sodium trisilicate glass," J. Appl. Phys. **68,** 4253-4257 (1990).

[10] R. L. Webb, L. C. Jensen, S. C. Langford, and J. T. Dickinson, "Interactions of wide band-gap single crystals with 248-nm excimer laser radiation. I. MgO," J. Appl. Phys. **74,** 2323-2337 (1993).

[11] R. L. Webb, L. C. Jensen, S. C. Langford, and J. T. Dickinson, "Interactions of wide band-gap single crystals with 248-nm excimer laser radiation. II. NaCl," J. Appl. Phys. **74,** 2338-2346 (1993).

[12] T. E. Madey, "Electron- and photon-stimulated desorption: Probes of structure and bonding at surfaces," Science **234,** 316-322 (1986).

[13] J. T. Dickinson, S. C. Langford, J. J. Shin, and D. L. Doering, "Positive ion emission from excimer laser excited MgO surfaces," Phys. Rev. Lett. **73,** 2630-2633 (1994).

[14] D. R. Ermer, S. C. Langford, and J. T. Dickinson, "Interaction of wide bandgap single crystals with 248 nm excimer laser radiation. V. The role of photoelectronic processes in the formation of a fluorescent plume from MgO," J. Appl. Phys. **81,** 1495-1504 (1997).

[15] J. J. Shin, D. R. Ermer, S. C. Langford, and J. T. Dickinson, "The role of photoelectronic processes in the formation of a fluorescent plume by 248 nm laser irradiation of single crystal $NaNO_3$," Appl. Phys. A **64,** 7-17 (1997).

[16] H. Hora, *Physics of Laser Driven Plasmas* (John Wiley, New York, 1981).

[17] D. R. Ermer, J.-J. Shin, S. C. Langford, K. W. Hipps, and J. T. Dickinson, "Interaction of wide bandgap single crystals with 248 nm excimer laser radiation. IV. Positive ion emission from MgO and $NaNO_3$," J. Appl. Phys. **80,** 6452-6466 (1996).

[18] A.-M. Lanzillotto, T. E. Madey, and R. A. Baragiola, "Negative-ion desorption from insulators by electron excitation of core levels," Phys. Rev. Lett. **67,** 232-235 (1991).

[19] M. Bernheim and G. Rousse, "Surface potential control on thin oxide films with respect to electron stimulated desorption studies," Journal de Physique III **5,** 1407-1424 (1995).

[20] P. J. Chantry and G. J. Schulz, "Kinetic-energy distributions of negative ions formed by dissociative electron attachment and the measurement of the electron affinity of oxygen," Phys. Rev. **156,** 134-141 (1967).

[21] L. Sanche, "Dissociative attachment in electron scattering from condensed O_2 and CO," Phys. Rev. Lett. **53,** 1638-1641 (1984).

[22] H. Sambe, D. E. Ramaker, L. Parenteau, and L. Sanche, "Image-charge effects in electron-stimulated desorption: O^- from O_2 condensed on Ar films grown on Pt," Phys. Rev. Lett. **59,** 236-239 (1987).

[23] J. Stevefelt, J. Boulmer, and J.-F. Delpech, "Collisional-radiative recombination in cold plasmas," Phys. Rev. A **12,** 1246-1251 (1975).

[24] W. H. Soon and J. A. Kunc, "Kinetics and continuum emission of negative atomic ions in partially ionized plasmas," Phys. Rev. A **43,** 723-734 (1991).

CHAPTER FOUR

Interactions between fluorocarbon polymers and 157-nm excimer laser radiation: I. Emission of $(CF_2)_N$ fragments from polytetrafluoroethylene

Sharon R. George, S. C. Langford and J. T. Dickinson

Abstract

We report time- and mass-resolved measurements on neutral particles emitted from polytetrafluoroethylene (PTFE) during exposure to 157-nm laser radiation at fluences where etching is observed. We observe neutral $(CF_2)_N$ radicals for all N up to the limit of our mass filter (N = 6). These radicals are emitted directly from the surface in substantial quantities. The mean kinetic energies of the fastest $(CF_2)_N$ radicals are about 0.6 eV for each of the detected masses. These kinetic energies are independent of fluence, suggesting that they travel from the surface to the detector without collision. These high kinetic energies are consistent with photochemical scission of the polymer backbone, where a fraction of the excitation energy is delivered to the fragment as kinetic energy. That said, most of the radicals detected under these conditions are slower. Immediately after the laser pulses, the great majority of these slower particles are incorporated into an expanding body of gas that undergoes hydrodynamic flow. We describe a simple but illustrative model to describe the motion of these slower fragments.

1. Introduction

Polytetrafluoroethylene (PTFE) is a chemically stable, biocompatible polymer with a low surface energy, low coefficient of friction, and high resistivity. Although these properties are desired in many applications, its use is often hindered by its poor machinability using conventional techniques. Precision etching of PTFE has been demonstrated using 157-nm excimer lasers.[1-3] High quality thin films have also been deposited by laser ablation deposition at 157 nm.[4-6] These results have been attributed in part to the photodecomposition of PTFE at 157-nm,[6,7] as opposed to the thermal decomposition that takes place at longer excimer wavelengths.[8-12] That said, the evidence for photochemical decomposition at 157 nm has not been entirely unequivocal.[13]

In this work, we show that the primary neutral products of ablation of PTFE at 157 nm are $(CF_2)_N$ fragments.[14,15] In contrast, the dominant product of laser ablation during 248-nm excimer laser ablation has been shown to be the monomer, C_2F_4.[10,11] Monomer production is consistent with the thermal depolymerization (unzipping) of the polymer chain,[16][Madosky, 1994; Welsh, 1996 #3936} while $(CF_2)_N$ fragments are consistent with random photochemical scission of the polymer chain. The fastest of the fragments at each mass have kinetic energies of about 0.6 ± 0.2 eV, independent of fluence. These energies are well above typical thermal energies, and again support a photochemical emission mechanism.

That said, the great majority of $(CF_2)_N$ fragments detected in this work are slower, consistent with a brief period of hydrodynamic flow immediately after the laser pulse. Hydrodynamic flow is also consistent with estimates of the particle density immediately after the laser pulse. Unfortunately, analytic expressions for the particle densities detected after the transition from hydrodynamic flow to free flight in vacuum are not available. We have proposed a somewhat oversimplified model for these particle densities.[15] With a empirical patch to account for particles that undergo the transition to free flight before the main body, the model

describes our time-of-flight signals reasonably well, with parameters that remain physically plausible up to the highest fluences employed in this work (1.5 J/cm^2).

2. Experiment

The PTFE targets employed in this work were 1-mm thick sheets supplied by Goodfellow Corporation (Oakdale, Pennsylvania, USA). Experiments were conducted in vacuum chambers at background pressure of 3×10^{-7} Pa. Pulsed 157-nm radiation was provided by a Lambda Physik LPF200 F_2 excimer laser operating at a pulse repetition rate of 5 Hz and pulse width of 20 ns at fluences from 0.4 to 1.5 J/cm^2. The laser beam was directed at the sample through a calcium fluoride lens with a 50 cm focal length. Without aperture, the beam profile was roughly rectangular, with a Gaussian intensity distribution across the narrow dimension of the rectangle.

Mass-resolved time-of-flight signals were acquired with a UTI 100C quadrupole mass spectrometer (QMS). Neutral molecules passed through an electron impact ionizer operating at a electron kinetic energy of 70 eV.

Depth of etch pits were determined using a profilometer on samples irradiated at different fluences with 50 laser pulses.

3. Results

A histogram of the intensities of signals observed during the laser ablation of PTFE by 157 nm laser radiation is plotted in Fig. 1. These fragments are detected as positive ions after electron-impact ionization (70 eV electrons) in the quadrupole ionizer. Published data on the fragmentation of PTFE by electron impact indicates that most of these species can be produced by fragmentation in the quadrupole ionizer.[17] Ionization most often involves the removal of an electron or the removal of an F^- ion.

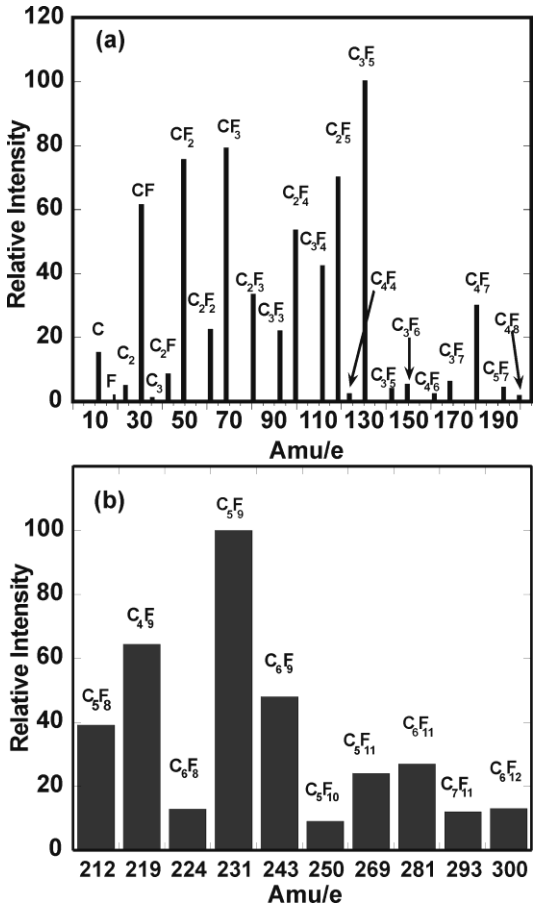

Fig. 1. Histogram of relative intensities of mass fragments detected during 157-nm ablation (a) between 0 and 200 amu and (b) between 200 and 300 amu at a fluence per pulse of 1.4 J/cm^2. The intensities have been adjusted to correct for the decreasing ion transmission through the mass filter with increasing mass.

To identify species produced by 157 nm laser irradiation, careful comparisons were made of the particle time-of-flight signals. Molecules emitted by laser ablation are designated parent species, as these are the source of all the other observed species, denoted cracking fragments. Cracking fragments are produced as the parents pass through the ionizer. Both cracking fragments and parents (now ions) are accelerated to a kinetic energy of 15 eV as they enter the mass filter. Due to their lower mass, cracking fragments will arrive at the detector before the parents by a small, well-defined time that depends on their mass ratios. Since the various parent species generally pass through the quadrupole ionizer at different times, they can usually be identified by their distinct arrival times at the detector.

In this manner, we had identified the following parent molecules: CF_2, C_2F_4, C_3F_6, C_4F_8, C_5F_{10}, and C_6F_{12}—all radicals of the form $(CF_2)_N$. Since mass filter is effective only at masses less than about 300 amu (corresponding to $N = 6$), more massive species may be present but not detected. The great majority of the signals at the corresponding masses can be attributed to laser ablation. Conversely, the majority of the signals at masses corresponding to the other radicals in Fig. 1 are produced in the ionizer due to fragmentation by electron impact. The dominance of neutral $(CF_2)_N$ fragments among the observed products is consistent with more-or-less random scission of C-C bonds along the PTFE backbone. As thermal bond scission in PTFE yields mostly monomer fragments (C_2F_4),[16,18,19] the observation of $(CF_2)_N$ fragments is strong evidence for another production mechanism—most likely photochemical scission of the C-C bonds.[6,7,15]

These small, highly reactive $(CF_2)_N$ radicals may also promote polymerization of fluoroethylene oligomers in thin films deposited by laser ablation, increasing film quality. We note, however, that these radicals are quite volatile and easily vaporized from heated substrates.[20]

Matientzo *et al.* observed a similar pattern of fragmentation using IR laser-assisted mass spectroscopy of PTFE that had been damaged by exposure to VUV radiation from a helium plasma source.[18] They detected negative ions of the form $C_NF^-_{(2N+1)}$, consistent with random scission of the C-C bonds, followed by reactions with F^- to form negative ions.

Electron-impact fragmentation in some cases distort the relative intensities of the observed signals. For instance, The intensity of the cracking fraction C_4F_7 in Fig. 1 is several times more intense than the intensity of the expected parent, C_4F_8. That said, the arrival time of the parent should not be affected by this loss of intensity. In Fig. 2, we show time-of-flight signals for each of the identified parents in this work. Importantly, the differences between the peak arrival times are much greater than the 10-20 μs differences expected for fragments with the indicated masses produced in the ionizer at the same time. At the very least, most of the signal at each mass is due to a unique product of laser ablation.

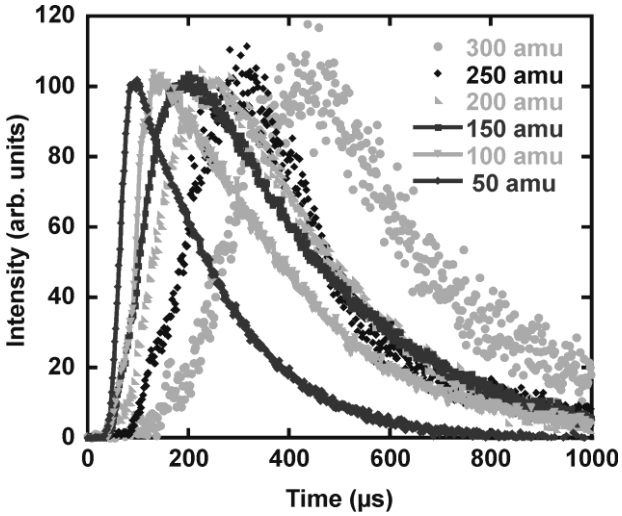

Fig. 2. Normalized time-of-flight signals for the six $(CF_2)_N$ fragments emitted directly from the surface during 157-nm ablation at a fluence per pulse of 1.1 J/cm^2.

We note that the expected optical properties of fluoroethylene oligomers are inconsistent with significant interactions with 157 nm *after* emission. Calculations by Robin suggest that PTFE oligomers with molecular weights less than about 2400 amu do not absorb significantly at 157 nm.[21] The ablation plume should be transparent at 7.9 eV. This would seem to rule out significant bond scission after emission—at least for fragments with masses under about 2400 amu. We expect that the large majority of the light particles that make up our TOF signals come directly from the sample; they are not produced in the ablation plume.

Importantly, the leading edge of the time-of-flight signals for each of the parent $(CF_2)_N$ species does not shift with laser fluence—often despite significant shifts in the peak arrival times. Figure 3 shows time-of-flight signals acquired at 50 amu (CF_2), 100 amu (C_2F_4) and 150 amu (C_3F_6) at three different fluences for each species. The CF_2 signals generated at fluences from 0.8–1.5 J/cm^2 are all quite similar, despite marked differences in intensity (shown below). Although, the time-of-flight peaks for C_2F_4 shift consistently with fluence, the leading edges shift hardly at all. In the case of C_3F_6, close inspection shows that the leading edge changes some with fluence, but not in a consistent fashion.

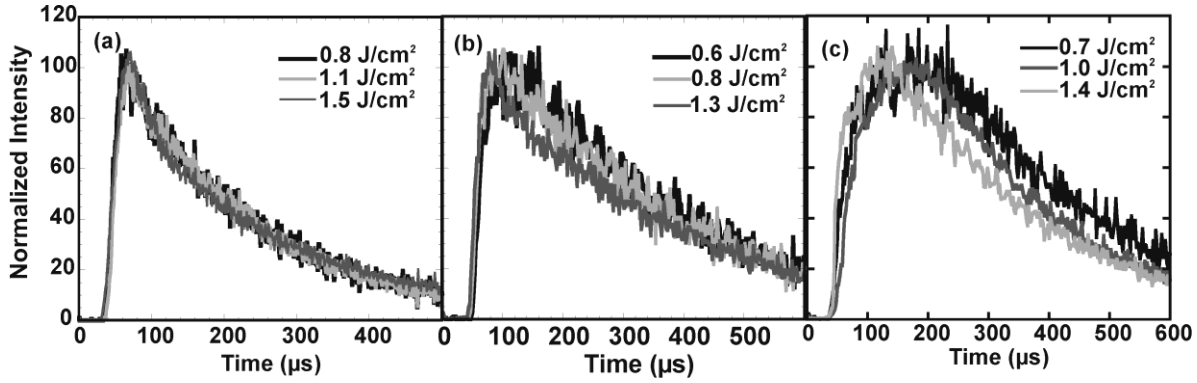

Fig. 3. Time-of-flight signals acquired at (a) 50 amu—CF_2, (b) 100 amu—C_2F_4, and (c) 150 amu—C_3F_6 at the indicated fluences.

The behavior of the fastest products is significant because the velocity of products emitted in thermal equilibrium with a surface consistently increase with temperature, which in turn increases with laser fluence. Further, collisions between atoms and molecules *after* emission also accelerate the fastest particles.[22-24] As few as four collisions per particle can have dramatic effects on the time-of-flight signal.[22] The relatively consistent time-of-flight (and thus velocity) of the fastest products at each mass implies that they have traveled from the sample to the quadrupole ionizer virtually without collision. Further, these fastest particles were not in thermal equilibrium with the surface at the time of emission.

The required lack of collisions is especially remarkable given this high particle densities expected in the ablation plume. Over this range of fluences, the etch rates inferred from post-ablation topography measurements range from 20 nm/pulse at 0.4 J/cm^2 to over 400 nm/pulse at 1 J/cm^2. If even 20 nm of PTFE material were ejected as 0.6 eV monomer units (100 amu) at a constant rate during a 20 ns laser pulse with velocities directed normal to the surface (1000 m/s), the particle density at the end of the pulse would exceed 10^{19} particles/cm^3. Even with an unrealistically low, room temperature thermal dispersion in velocities (relative velocities near 200 m/s), the corresponding collision rate would exceed 1 ns^{-1}.

At these high densities and collision rates, hydrodynamic conditions prevail, and the great majority of the particles will behave collectively as gas undergoing adiabatic expansion. Further,

the amorphous, coiling structure of PTFE suggests that the initial particle velocities would actually be randomly directed, rather than directed normal to the surface. The average velocity of the resulting cloud will be zero, but the expansion velocity can approach the speed of sound in the gas. We then attribute the leading edge of the TOF signal to particles emitted from the surface near the beginning of the laser pulse, whose velocities happen to be directed (to a good approximation) along the surface normal, toward our detectors.

If this scenario applies to our experiment, we would expect the fast particles to make up a substantial fraction of the total TOF signal at low fluences, where particles originating from the surface make up a large fraction of the total. The distinction between the fast and slow particles is most clear at moderate masses, due to the reduced particle velocities at higher masses. (These lower velocities also result in lower particle fluxes at the detector—resulting in a trade-off between resolution and signal intensity.) Figure 4 shows time-of-flight signals for C_3F_6 acquired at fluences of 0.4 and 1.0 J/cm^2. At 0.4 J/cm^2, the structure along the leading edge forms a distinct peak; whereas at 1.0 J/cm^2, it is merely a prominent shoulder. Consistent with measurements made at higher fluences, the structures along the leading edges of these signals both peak near 100 μs. The fast peak in Fig. 4 is followed by a slow feature that peaks near 230 μs, which we attribute particles experiencing multiple collisions on the way to the detector.

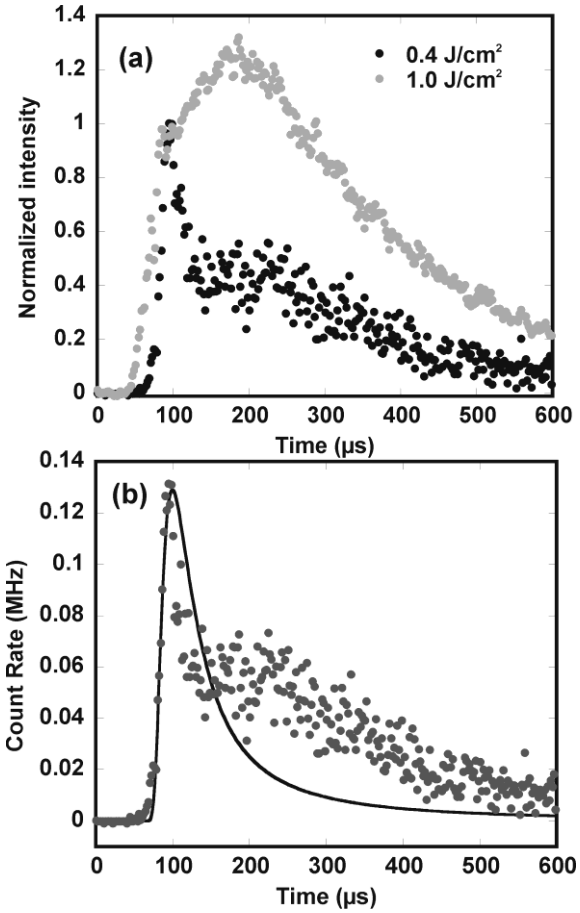

Fig. 4. Time-of-flight signals for C_3F_6 (150 amu) (a) acquired at fluences of 0.4 and 1.0 J/cm^2, normalized so that the structures along the leading edges have the same height; and (b) the signal acquired at a fluence of 0.4 J/cm2, showing a fit of Eq. (1) to the signal for times less than 150 μs (dark line).

The fast peak in Fig. 4 is well isolated and suitable for robust characterization by curve fitting techniques. If the particles were emitted in thermal equilibrium with the surface, the effusive Maxwell-Boltzmann distribution would provide an appropriate model.[25] Curve fits to this model yield effective surface temperatures near 8000 K. This degree of surface heating is unlikely. If we assume that the fast peak is composed of molecules with a 1-D Gaussian distribution in energy, we expect a time-of-flight signal with the form:

$$I(t) = \frac{m d_I N_0}{\sqrt{2\pi}\sigma (t - t_Q)^2} \exp\left[\frac{-1}{2\sigma^2} \left(E_0 - \frac{m d^2}{2(t - t_Q)^2} \right)^2 \right], \quad (1)$$

where m is the particle mass, d_I is the distance between the sample to the middle of the quadrupole ionizer (10.5 cm), t is the arrival time at the detector, and t_Q is the time required for the ionized particle to pass through the mass filter. The adjusted parameters are N_0, the number of detected particles, E_0, the mean particle kinetic energy, and σ, the standard deviation of the particle energy distribution. The fit of Eq. (1) to the fast peak in Fig. 4 (using data for times $t <$ 150 μs) is shown as the dark line in Fig. 4. The best-fit value for the mean kinetic energy, E_0, is 0.6 ± 0.2 eV. This kinetic energy is well above typical thermal energies, and is consistent with a photochemical origin.

To test the ability of Eq. (1) to describe for the fast particles at higher fluences, we must account for the slower particles as well. Analytic expressions are preferred for the computational efficiency, although they are limited and approximate. A major class of analytic solutions to the hydrodynamic equations are self-similar: the functional form of the density distribution is unchanged during evolution.[26-28] Of these, the simplest are Gaussian. The Gaussian density distribution satisfies the hydrodynamic equations for the case of an adiabatically expanding gases with uniform (but changing) temperature; further, evolution maintains the Gaussian form.[26,27] Gaussian distributions suffer the defect of extending to infinity, which we ignore. They also neglect the important transition to free flight, as the cloud expands and collisions become increasingly rare. Although the transition to free flight is not appropriately described, the function itself can be smoothly transformed into the full range Maxwell-Boltzmann distribution, which describes particles in free flight. As we will show, the result will require a patch (another function) to adequately describe the data.

Self-similar solutions evolve so as to maintain a constant ratio between the x-coordinate of a moving patch of gas and a characteristic dimension of the distribution remains constant. In

the case of a Gaussian distribution, this characteristic dimension can be interpreted as a standard deviation. Thus $[x(t)/\sigma_x(t)]^2$ remains constant as the flow evolves. To obtain the distribution as a function of (x,y,z), we replace x(t) with the x-coordinate at which measurement is made. The resulting density distribution in 3-D is then[26]

$$\rho(\vec{x},t) = \frac{\rho_0}{(2\pi)^{3/2}\sigma_X\sigma_Y\sigma_Z} \cdot \exp\left[-\frac{x^2}{2\sigma_X^2} - \frac{y^2}{2\sigma_Y^2} - \frac{z^2}{2\sigma_Z^2}\right] \tag{2}$$

where σ_x, σ_y, and σ_z are functions of time and ρ_0 is the initial density. For an ideal gas with specific heat ratio γ, the (uniform but changing) temperature evolves according to the relation:[26]

$$T = T_0\left(\frac{\sigma_{X0}\sigma_{Y0}\sigma_{Z0}}{\sigma_X\sigma_Y\sigma_Z}\right)^{\gamma\text{-}1} \tag{3}$$

A solution for the density versus time can be obtained by numerically integrating the relations:

$$\sigma_X\left(\frac{d^2\sigma_X}{dt^2}\right) = \sigma_Y\left(\frac{d^2\sigma_Y}{dt^2}\right) = \sigma_Z\left(\frac{d^2\sigma_Z}{dt^2}\right) = \frac{kT_0}{m}\left(\frac{\sigma_{X0}\sigma_{Y0}\sigma_{Z0}}{\sigma_X\sigma_Y\sigma_Z}\right)^{\gamma-1} \quad , \tag{4}$$

where σ_{x0}, σ_{y0}, and σ_{z0} are the initial standard deviations.

However, our particles are detected some 10.5 cm away from the sample, long after the transition to free flight. In this regard, we note that the functional form of Eq. (2) is identical to that of the full-range Maxwell-Boltzmann distribution, obtained by setting $\sigma_x = \sigma_y = \sigma_z = {}_t (kT/m)^{1/2}$. Physically, a transition from the $\sigma(t)$ in Eq. (4) to $(kT/m)^{1/2}$ would require that the entire gas cloud makes the transition to free flight at the same instant, which it does not. But it is likely that the densest regions of the expanding gas cloud, closest to the surface, transit rapidly to free flight; here the density gradients are small and would approach the threshold for free flight

almost simultaneously. Thus there is hope that the full range Maxwell-Boltmann would provide an approximate account for a significant portion of the gas cloud. Further, we require that $_t$ $(kT/m)^{1/2}$ at the time of detection is much greater than σ_x, σ_y, and σ_z at the time of transition to free flight—which is reasonable for detectors mounted well away from the sample. Finally, the flow velocities of particles at the time of transition must be small relative to their thermal velocities.

If we measure the density at a point x along the x-axis (so that $y = z = 0$),

$$\rho(x, y = 0, z = 0, t) = \frac{\rho_0}{t^3}\left(\frac{m}{2\pi kT}\right)^{3/2} \exp\left[-\frac{mx^2}{2kTt^2}\right] \quad . \tag{5}$$

From Eq. (3), we identify the temperature T in Eq. (5) with the temperature at the transition to free flight, and not the temperature of the surface. Finally, we must include an experimental detail. Although the signal we detect is proportional to the particle density at the ionizer, the particle is not detected until a time t_Q later, after the particle passes through the mass filter. This time is determined uniquely by the particle mass and the time of detection. The corresponding signal is then

$$\rho(x, y = 0, z = 0, t) = \frac{\alpha\rho_0}{(t - t_Q)^3}\left(\frac{m}{2\pi kT}\right)^{3/2} \exp\left[-\frac{mx^2}{2kT(t - t_Q)^2}\right] \quad , \tag{6}$$

where α is a constant that accounts for the ionization, mass filter, and detection efficiencies.

Equation (6) incorporates two adjustable parameters, ρ_0 and T, and provides a good description of the TOF of the slowest particles in this work—the tails of the TOF signals. To account for particles with intermediate arrival times, we added a second Gaussian density distribution [Eq. (1)] with E_0 fixed to zero. This adds two adjustable parameters, another magnitude N and standard deviation σ. Physically, this second Gaussian provides an entirely empirical account for particles that make transition to free flight well before the main body of

gas. This would also include particles that undergo a small number of collisions before transitioning to free flight, and thus are never experience hydrodynamic flow. These particles form a Knudsen layer, where the collision rate is high enough to modify the velocity distributions, but insufficient for hydrodynamic flow.[22]

Figure 5 displays TOF signals acquired for three particles, CF_2, C_3F_6, and C_6F_{12}, a fluence of 0.8 J/cm^2, with the corresponding curve fits. The seven parameter fit allows for reasonable fits over the entire range of probed masses. Further, the model satisfies two physical expectations associated with the proposed emission mechanism and subsequent TOF evolution. The mean kinetic energy of the fast peak is essentially the same for each fragment mass: 0.6 ± 0.2 eV. This same kinetic energy applied to TOF measurements over the entire range of fluences employed in this work. Furthermore, at a given fluence, the effective temperature (at the transition to free flight) was about the same for all the parent molecules. For instance, the curve-fit temperatures from the TOF signals in Fig. 5 were 830 ± 20 K. As the fluence was increased from 0.7 to 1.5 J/cm^2, the curve fit temperatures smoothly increased from about 800 to 1500 K. As the fluence is increased, more thermal energy is deposited into the emitted fragments.

The gradual increase in temperature with fluence is consistent with the weak dependence of temperature on gas cloud volume implied by Eq. (3) and typical values for the heat capacity ration. (For instance, $\gamma \sim 1.24$ for ethylene at 1 atm and15 °C). [29] Thus the cooling associated with adiabatic expansion will not be able to offset the increased energy supplied to the emission products at higher fluences.

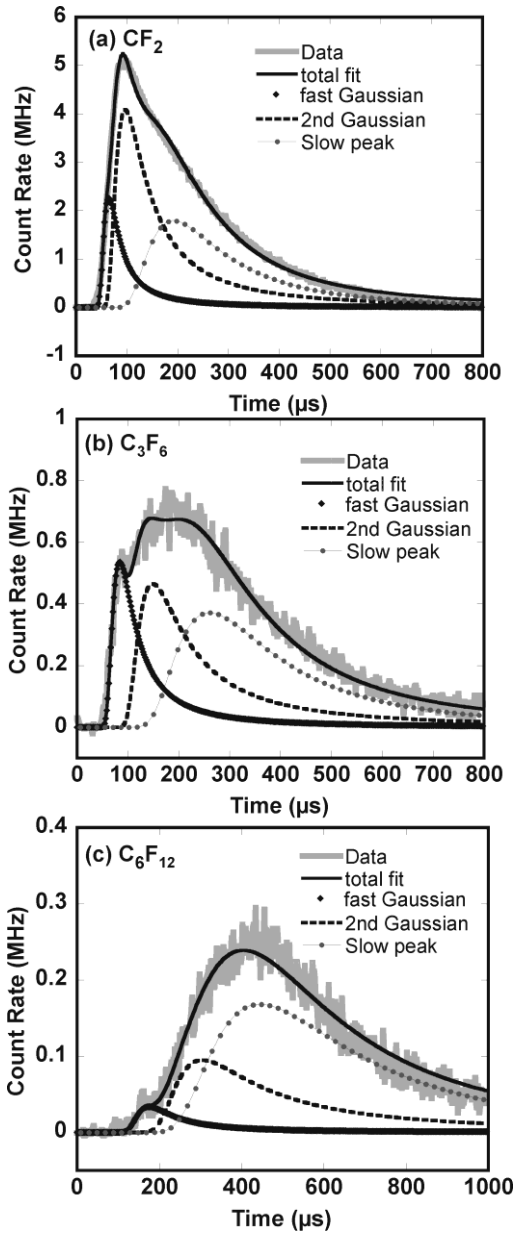

Fig. 5. Time-of-flight signals for (a) CF_2—50 amu, (b) C_3F_6—150 amu, and (c) C_6F_{12}—300 amu acquired at a fluence of 0.8 J/cm^2. The dark lines through the data show least squares curve fits of the data incorporating a fast Gaussian energy distribution [Eq. (1)], a slower Gaussian energy distribution with zero mean kinetic energy, and an even slower full-range Maxwell Boltzmann distribution [Eq. (6)].

The intensity of the fast peak in Fig. 5(c) (300 amu) is much lower than the intensities of the lighter particles—50 amu in Fig. 5(a) and 150 amu in Fig. 5(b). The fast peak intensity

drops markedly as the particle mass increases above 150 amu. We attribute this to the relatively low thermal velocities of the heavier particles. [Thermal velocities scale as $(kT/m)^{1/2}$, where m is the particle mass.] Thus heavier particles emitted early in the laser pulse are often overtaken by lighter particles emitted later. The resulting collisions reduce the number of particles in the heavy particle fast peaks.

When interpreted with care, the fluence dependence of the emission intensities often carries information on the process by which the particles were created. For instance, we expect the signal intensities described above to systematically under-represent the total emission intensities, due to adiabatic expansion perpendicular to the line-of-sight path to the quadrupole ionizer. The intensities associated with the fast particles (that do not undergo collision) should provide a much better indication of the emission mechanism—at least for those particles emitted early in the laser pulse.

In Fig. 6, we plot the area of the fast component (determined from the curve fits) for TOF signals for CF_2, C_2F_4, and C_3F_6. In each case, the fluence dependence of the fast component is about 1.7^{th} order. We cite evidence below to the effect that the energy of a single 7.9 eV photon is sufficient to break C-C bonds in the PTFE structure. The observed fluence dependence is consistent with the expectation that the production of small PTFE fragments requires that the chain be broken at two points—*except* when scission occurs close to the chain end. Chain end scission of intact chains would probably not produce the detected species, assuming that the chains are terminated with $-CF_3$. But it is reasonable to expect that some chains are broken in the material that remain even after each laser pulse. Some of chain-end CF_2 radicals would then be available for emission during the next laser pulse. We suggest that the combination of single- and double-scission events could account for the observed 1.7^{th} order fluence dependence.

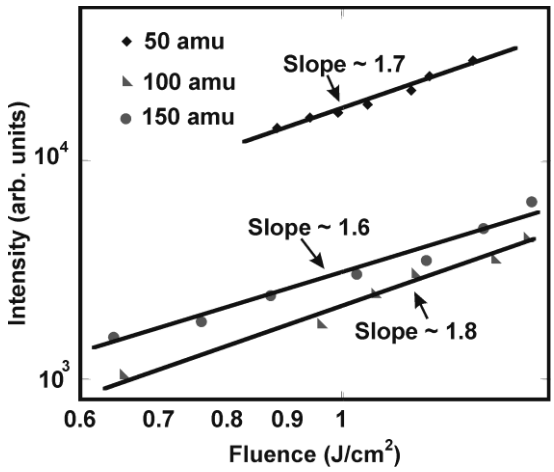

Fig. 6. Fluence dependence of the fast peak areas (determined from curve fits) for CF_2—50 amu, C_2F_4—100 amu, and C_3F_6—150 amu.

4. Discussion

The ability of 157-nm excimer lasers to etch clean structures in PTFE has been tentatively attributed to the photochemical scission of C-C bonds in the polymer chain.[6,7] At longer excimer wavelengths (with the possible exception of 193 nm), chain scission is primarily thermal,[8,11] and thermal damage to small structures is an issue.

Band structure calculations verify that 157 nm (7.9 eV) photons are sufficient to produce bandgap excitations in PTFE.[30,31] Recent calculations suggest that absorption at 7.9 eV is mediated by C-C sigma bonds along the polymer chain.[31] Nagayama *et al*. has shown that VUV absorption at 7.9 eV is strongest when the VUV light is polarized along the direction parallel to the PTFE chains, consistent with absorption into C-C sigma states.[32] Although these calculations do not prove that 7.9 eV excitations can cleave C-C bonds, the localization of excitations on these bonds would provide a mechanism for photoelectronic cleavage. Since thermal decomposition of PTFE yields (almost exclusively) the monomer (C_2F_4),[16,19] the production of $(CF_2)_N$ fragments rules out a thermal mechanism for ablation

Missing mass. As mentioned above, the etch rates inferred from measurements after ablation ranged from about 20 nm/pulse at 0.4 J/cm^2 to 400 nm per pulse near 1 J/cm^2. The

material removal rate at 1 J/cm^2 corresponds to about 10^{-10} g/pulse. If all this material was removed as small fragments, the resulting signal intensities would saturate our instruments at even lower mass removal rates. We have recently shown that about 90% of the mass removed under the conditions of this work appears as heavy fragments, with masses well above the upper limit of our quadrupole mass filter. Moreover, the trajectories of these heavier fragments are directed well away from the surface normal and do not reach our detector. These heavier fragments are the subject of Chapter five of this thesis.

5. Conclusions

Quadrupole time- and mass-resolved measurements of neutral particles emitted during the laser ablation of PTFE at 157 nm shows intense signals due to $(CF_2)_N$ fragments, where N ranges from $N = 1$ to the upper limit of our mass filter, $N = 6$. The observation of intense emissions at masses other than the monomer rule out thermally-activated depolymerization of the polymer chain as an important source of material removal. The high kinetic energies (about 0.6 eV) and fluence dependence (typically 1.7th order) of the faster fragments are consistent with emission due to photochemical scission of C-C bonds. These observations provide strong support to previous arguments for the photochemical etching of PTFE at 157 nm.[6,7]

Photochemical bond scission at 157 nm (but not at 248 nm and longer excimer wavelengths) would account for lack of thermal damage in microstructures produced by laser ablation at 157 nm.[4-6] Highly reactive $(CF_2)_N$ radicals may also promote polymerization of fluoroethylene oligomers in thin films deposited by laser ablation. However, it is likely that any radicals responsible for polymerization are somewhat larger than those directly observed in this work, as the light radicals are quite volatile at room temperature.[20] We have recently found evidence for much heavier radical fragments, discussed in Chapter five.

Acknowledgment

This work was supported by the U.S. Department of Energy under Grant DE-FG02-04ER-15618. We thank Leonid Zhigilei, University of Virginia, for helpful discussions

References

[1] J. Cashmore, M. Gower, P. Gruenewald, D. Karnakis, and M. Whitfeild, in *High-resolution micromachining using short wavelength and shortpulse lasers*, Chiba, Japan, 1993, p. I-292-I-293.

[2] M. Fiebig, M. Kauf, J. Fair, H. Endert, M. Rahe, and D. Basting, "New aspects of micromachining and microlithography using 157-nm excimer laser radiation," Appl. Phys. A **69,** S305 (1999).

[3] P. R. Herman, K. P. Chen, M. Wei, J. Zhang, J. Ihlemann, D. Schafer, G. Marowsky, P. Oesterlin, and B. Burghardt, "F_2-lasers: High-resolution micromachining system for shaping photonic components," Conference on Lasers and Electro-Optics**,** 574-577 (2001).

[4] Y. Ueno, T. Fujii, and F. Kannari, "Deposition of flouropolymer thin films by vacuum-ultraviolet laser ablation," Appl. Phys. Lett. **65,** 1370-1372 (1994).

[5] T. Fujii, S. Inoue, and F. Kannari, "Deposition of flouropolymer thin films containing semiconductor microcystallites by VUV laser ablation," Appl. Surf. Sci. **96-98,** 621-624 (1996).

[6] N. Huber, J. Heitz, and D. Bauerle, "Polytetrafluoroethylene (PTFE) films prepared by F2-Laser deposition," Eur. J. Appl. Phys. **29,** 231-238 (2005).

[7] A. Costela, I. Garcia-Moreno, F. Florido, and J. M. Figuera, "Laser ablation of polymeric material at 157 nm," J. Appl. Phys. **77,** 2343-2350 (1995).

[8] P. M. Goodwin and C. E. Otis, "Ultraviolet photoablation of p-tetrafluoroethylene: Rotational energy distributions of the CF radical and time-resolved mass spectra," J. Appl. Phys. **69,** 2584-2588 (1991).

[9] G. B. Blanchet and S. I. Shah, "Deposition of polytetrafluoroethylene films by laser ablation," Appl. Phys. Lett. **62,** 1026-1028 (1993).

[10] J. T. Dickinson, J.-J. Shin, W. Jiang, and M. G. Norton, "Neutral and ion emissions accompanying pulsed excimer laser irradiation of polytetrafluoroethylene," J. Appl. Phys. **74,** 4729-4736 (1993).

[11] G. B. Blanchet and C. R. Fincher, Jr., "Laser induced unzipping: A thermal route to polymer ablation," Appl. Phys. Lett. **65,** 1311-1313 (1994).

[12] G. B. Blanchet and C. R. Fincher, Jr., "Laser ablation: Selective unzipping of addition polymers," Appl. Phys. Lett. **68,** 929-931 (1996).

[13] T. Katoh and Y. Zang, "Synchrotron radiation ablative photodecomposition and production of crystalline fluoropolymer thin films," Appl. Phys. Lett. **68,** 865-867 (1996).

[14] S. R. George, J. A. Leraas, S. C. Langford, and J. T. Dickinson, "Interaction of 157-nm excimer laser radiation with fluorocarbon polymers," Appl. Surf. Sci. **255,** 9558-9561 (2009).

[15] S. R. John, S. C. Langford, and J. T. Dickinson, "Ablation mechanism of PTFE under 157 nm irradiation," Appl. Phys. A **92,** 981-985 (2008).

[16] S. L. Madorsky, *Thermal Degradation of Organic Polymers* (Interscience Publishers, New York, 1964).

[17] S. R. Heller and G. W. A. Mile, *EPA/NIH Mass Spectral Data Base* (U.S. Dept. of Commerce, NBS, Washington, DC 1978).

[18] L. J. Matienzo, J. A. Zimmerman, and F. D. Egitto, "Surface modification of fluoropolymers with vacuum ultraviolet irradiation," Journal of Vacuum Science and Technology A: Vacuum, Surfaces, and Films **12,** 2662-2671 (1994).

[19] W. J. Welsh, in *Physical Properties of Polymers*, edited by J. E. Mark (American Institute of Physics, Woodbury, New York, USA, 1996), p. 605-614.

[20] H. H. Anderson, "Boiling points and boiling point numbers of perfluoroalkanes and perfluoroalkenes," J. Chem. Engin. Data **10,** 156–159 (1965).

[21] M. B. Robin, *Higher Excited States of Polyatomic Molecules*, Vol. 2 (Academic Press, New York, 1977).

[22] R. Kelly and R. W. Dreyfus, "On the effect of Knudsen-layer formation on studies of vaporization, sputtering, and desorption," Surf. Sci. **198,** 263-276 (1988).

[23] R. Kelly, "On the dual role of the Knudsen layer and unsteady, adiabatic expansion in pulse sputtering phenomena," J. Chem. Phys. **92,** 5047-5056 (1990).

[24] R. Kelly and A. Miotello, "Pulsed-laser sputtering of atoms and molecules. Part I. Basic solutions for gas-dynamic effects," Applied Physics B **57,** 145-158 (1993).

[25] M. L. Dawes, W. Hess, Y. Kawaguchi, S. C. Langford, and J. T. Dickinson, "Laser-induced positive ion and neutral atom/molecule emission from single crystal $CaHPO_4{\cdot}2H_2O$: The role of electron beam induced defects," Appl. Phys. A **69,** S547-S522 (1999).

[26] J. Dawson, P. Kaw, and B. Green, "Optical absorption and expansion of laser-produced plasmas," Phys. Fluids **12,** 875-882 (1969).

[27] G. J. Pert, "Self-similar flows with uniform velocity gradient and their use in modelling the free expansion of polytropic gases," J. Fluid Mech. **100,** 257-277 (1980).

[28] H. Hora, *Physics of Laser Driven Plasmas* (John Wiley, New York, 1981).

[29] W. F. L. Dick and A. G. M. Hedley, in *Thermodynamic functions of gases—Volume 2—Air, acetylene, ethylene, propane and argon*, edited by F. Din (Butterworths, London, 1962), p. pp. 88-114.

[30] K. Seki, H. Tanaka, T. Ohta, Y. Aoki, A. Imamura, H. Fujimoto, H. Yamamoto, and H. Inokuchi, "Electronic structure of poly(tetrafluoroethylene) studied by UPS, VUV absorption, and band calculations," Phys. Scripta **41,** 167-171 (1990).

[31] M. Ono, H. Yamane, H. Fukagawa, S. Kera, D. Yoshimura, K. K. Okudaira, E. Morikawa, K. Seki, and N. Uenoa, "UPS study of VUV-photodegradation of polytetrafluoroethylene (PTFE) ultrathin film by using synchrotron radiation," Nucl. Instrum. Meth. Phys. Res. B **236,** 377-382 (2005).

[32] K. Nagayama, T. Miyamae, R. Mitsumoto, H. Ishii, Y. Ouchi, and K. Seki, "Polarized VUV absorption and reflection spectra of oriented films of poly(tetrafluoroethylene) $(CF_2)_n$ and its model compound," J. Electron Spectrosc. Relat. Phenom. **78,** 407-410 (1996).

CHAPTER FIVE

Interactions between fluorocarbon polymers and 157-nm excimer laser radiation. II. Off-normal trajectories of heavy molecules during ablation of PTFE

Sharon R. George, S. C. Langford and J. T. Dickinson

Abstract

We report observations of particle emission from PTFE due to ablation with a 157-nm excimer laser. Polymer fragments with masses less than 300 amu are characterized by quadrupole-mass-selected, time-of-flight measurements. Heavier particles are collected on silicon substrates. Surprisingly, the trajectories of the heaviest fragments are preferentially directed at large angles away from the surface normal—often nearly parallel to the substrate surface. We attribute this behavior to density and pressure gradients associated with the Gaussian intensity profile of the laser beam. High number densities of lighter fragments are produced near the center of the laser spot, where the laser intensity is highest. Low number densities of heavier fragments are produced along the edge of the laser spot, where the intensities are lower. Since pressure is proportional to number density, high pressures develop near the center that accelerate the surrounding heavier particles to the side. The explanation is supported by numerical solutions to the hydrodynamic equations. Further, off normal trajectories are not observed when a uniform beam profile is employed. We suggest possible applications to the deposition of PTFE films.

1. Introduction

Polytetrafluoroethylene (PTFE) is well suited for many applications because of its excellent chemical stability, low surface energy, low coefficient of friction, and good electrical insulation. Unfortunately, PTFE surfaces and films are difficult to pattern by conventional techniques. The ability of F_2 excimer lasers (157-nm) to produce fine structures with minimal thermal damage[1-3] alleviates this difficulty for some high value applications.

The presence of heavy and light particles in the cloud of emitted particles gives rise to some unique behavior in the way it expands. The cloud in this case is a mixture of neutral fragments ranging from 50 amu to 2000 amu. We observe heavy fragments preferentially emitted in paths away from the surface and almost parallel to the surface while the lighter fragments are more forward directed. In this article we propose that this behavior is due to pressure gradients created due to the distribution of masses from the center of the laser spot toward the edges due to the Gaussian profile of the laser beam. These pressure gradients cause the heavy particles to be accelerated in the directions away from the surface normal. Hydrodynamic calculations on 2-component plumes in 2-dimensions were performed to test the validity of our hypothesis.

The presence of heavy fragments emitted during laser ablation is very advantageous to thin film growth by pulsed laser deposition as it eliminates the need for the substrate to be heated to drive polymerization reactions. We have been able to successfully deposit high quality films at room temperature on silicon wafers placed above and below the samples. Moreover our calculations show that it may be possible to deposit larger uniform thin-films by using two laser beams to create pressure gradients in the plume.

2. Experiment

The PTFE targets employed in this work were 1-mm thick sheets supplied by Goodfellow Corporation (Oakdale, Pennsylvania, USA). Experiments were conducted in vacuum chambers at background pressure of 3×10^{-7} Pa. Pulsed 157-nm radiation was provided by a Lambda Physik LPF200 F_2 excimer laser operating at a pulse repetition rate of 5 Hz and pulse width of 20 ns. The laser beam was directed at the sample through a 50 cm focal length lens. The fluences employed ranged from 0.5 to 0.8 J/cm^2 (per pulse). The laser beam profile was roughly rectangular, with a Gaussian intensity distribution across the narrow dimension of the rectangle.

Mass-resolved time-of-flight signals were acquired with a UTI 100C quadrupole mass spectrometer (QMS). Neutral molecules passed through an electron impact ionizer operating at a electron kinetic energy of 70 eV. Neutral emission measurements were performed using two mass filters placed above and in front of the surface as shown in Fig 1. We refer to the plane parallel to the long dimension of the laser spot as the xz-plane and the plane parallel to the shorter dimension as the xy-plane. To measure the emission at different angles in the xy-plane, the samples were tilted so as to only detect the emission at a given angle. Care was taken to keep the average fluence constant when the laser spot size on the sample changed due to the tilt. Also, in the measurements shown below, the signal intensities were corrected to account for the difference in sensitivity of the two detectors.

To perform differential scanning calorimetry (DSC) measurements on PTFE films of about 4 mg in weight were deposited in aluminum pans. The pans were weighed before and after the measurements were done. The heating and cooling rates used were 10° C/min. The samples were heated to 400° C and kept at that temperature for 5 min before cooling them

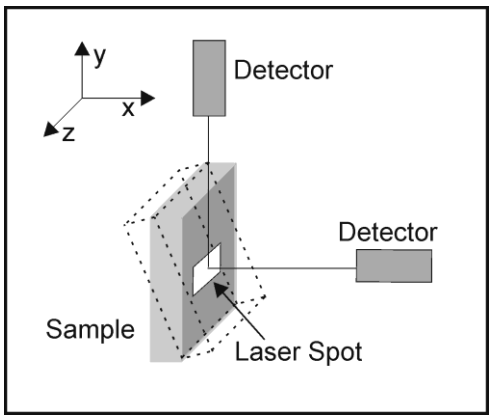

Fig 1 A schematic of the geometry for the time-of-flight measurements of particles emitted along the surface normal and particles emitted at an angle at 70° from the surface normal in the *xy*-plane (plane perpendicular to the long dimension of the laser spot).

3. Results and Discussion

Effect of beam profile. Profilometry measurements of PTFE surfaces exposed to 157-nm excimer laser radiation show etch rates as high as 400 nm/pulse at fluences near 1 J/cm^2.[4] Material is removed principally by photoelectronic scission of C–C bonds and yields fragments of the form $(CF_2)_N$ for $N = 1\ldots6$.[5] When the Gaussian beam of an F_2 excimer laser [6] is simply focused on to the sample, substantial emission intensities display trajectories well away from the surface normal, in the plane perpendicular to the narrow dimension of the laser spot.

Figure 1 shows mass-selected TOF signals acquired at 300 amu (C_6F_{12}). In Fig. 1(a), the Gaussian laser beam was simply focused onto the sample; whereas in Fig. 1(b), the beam was apertured to yield an essentially flat-top intensity profile. In each case, we compare the signal detected along the sample normal (normal direction) with signals detected at 70° from the sample normal (off-normal direction). The laser beam energy was adjusted in each case so that the average fluence at the sample was 820 mJ/cm^2 per pulse. When the beam profile is Gaussian, the signal measured at 70° is *several times* more intense than the signal along the normal of the sample, despite the relatively small change in laser spot size. This was *not* expected. In most

material-laser systems at high etch rates, the particle trajectories in vacuum tend to be strongly forward directed.[7]

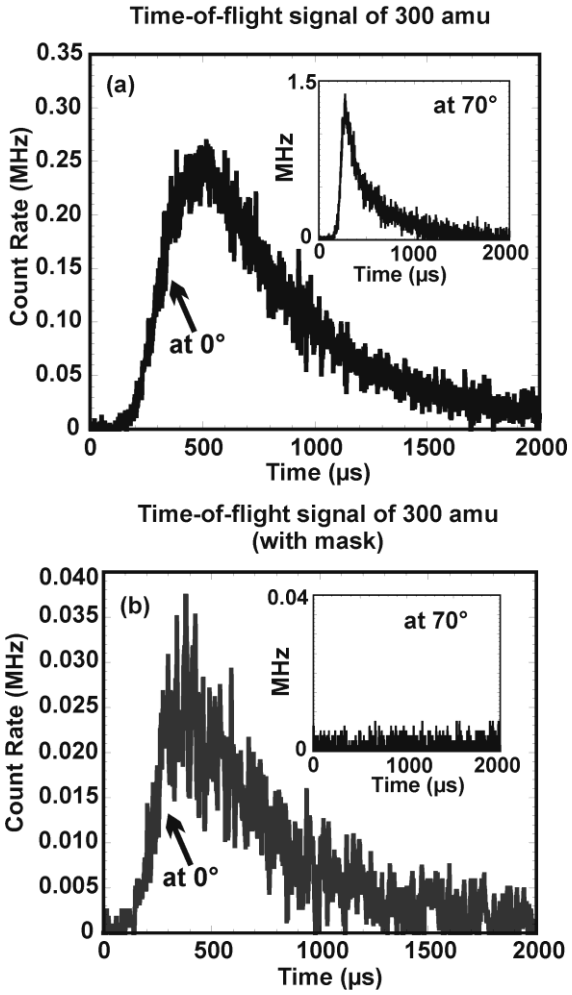

Fig. 2. Mass selected time-of-flight signals of 300 amu acquired at a fluence of 820 mJ/cm^2, measured 0° and 70° from the surface normal, (a) using the entire laser beam (Gaussian beam profile) (b) using only the most intense region of the beam (effectively a flat topped beam profile).

In Fig. 2(b), we show similar measurements made in the presence of a beam aperture. The aperture allows only the most intense portion of the beam to reach the sample; this significantly reduces the total laser energy incident on the surface, but results in a nearly uniform (flat-top) intensity profile. In this case, significant signals are observed along the normal

direction, but virtually nothing is observed 70° from the surface normal. This behavior is consistent with our expectation that emission be strongly forward directed.

Strong, off-normal emissions are also produced by the Gaussian beam at the other masses detected in this work, up to the 300 amu mass limit of our quadrupole mass spectrometer. Figure 3 shows mass-selected TOF signals acquired at masses corresponding to CF_2, C_2F_4, C_3F_6, C_4F_8, C_5F_{10} and C_6F_{12} using the un-apertured, Gaussian beam at a fluence of 820 mJ/cm^2. For each mass, we compare the signals detected with the sample surface perpendicular to the axis of the mass filter (along the surface normal), with signals detected with the sample tilted 70° from the axis of the mass filter (black curves). To better compare the TOF behavior of the normal and off-normal signals, they are normalized and replotted in the insets.

Significant off-normal emissions are observed at each mass. More importantly, the off-normal emissions dominate the total emission intensities as the particle mass approaches 300 amu—despite only a modest increase in total laser energy on the sample. To add insult to injury, the TOF peak appears much sooner for the off-normal signals at the highest masses. At 300 amu, the TOF peak for off-normal emission appears at 270 μs, while the TOF of the signal for the normal emission appears to peak at 550 μs. This difference is consistent with kinetic energies four times higher in the off normal emission. Not only is emission at 300 amu more intense in the off normal direction, these particles have been accelerated to substantial kinetic energies. Importantly, the TOF peaks for off-normal emission at masses greater than 150 amu appear at nearly the same position (about 250 μs), suggesting that a substantial number of particles at each mass are entrained in a body of gas which has been accelerated as one body to velocities near 400 m/s.

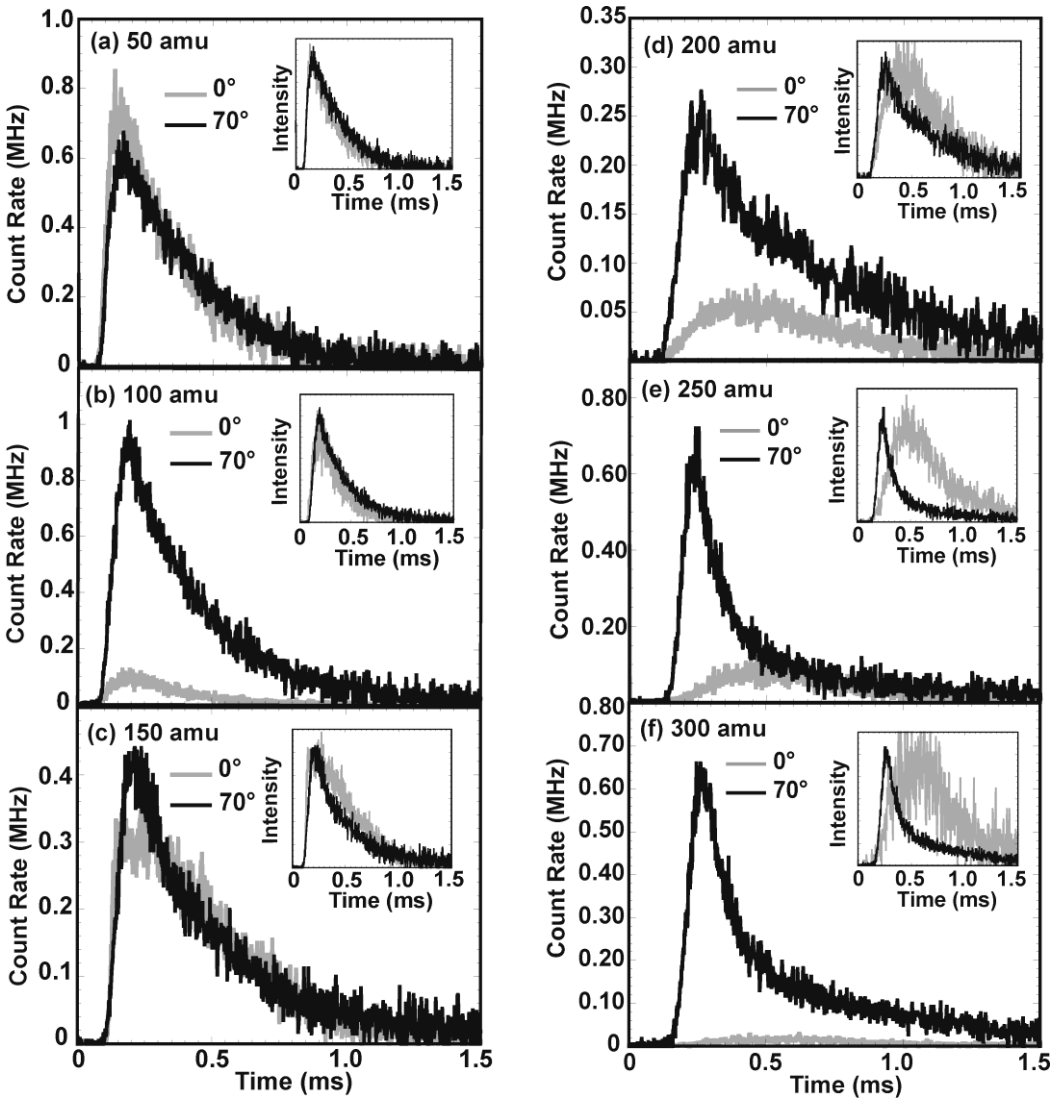

Fig. 3. Mass selected time-of-flight signals of neutral fragments measured along the surface normal (gray curves) and 70° off-normal in the plane perpendicular to the long dimension of the laser spot. The signals represent a sum of 200 pulses at a fluence of 820 mJ/cm^2.

Figure 4 shows the ratio of emission intensity at 70° to the intensity at 0° for the fragments observed between 50 and 300 amu at a fluence of 820 mJ/cm^2. For masses above 100 amu, this ratio increases monotonically with mass. Thus the mechanism responsible for off-normal trajectories is most effective for the heavier particles.

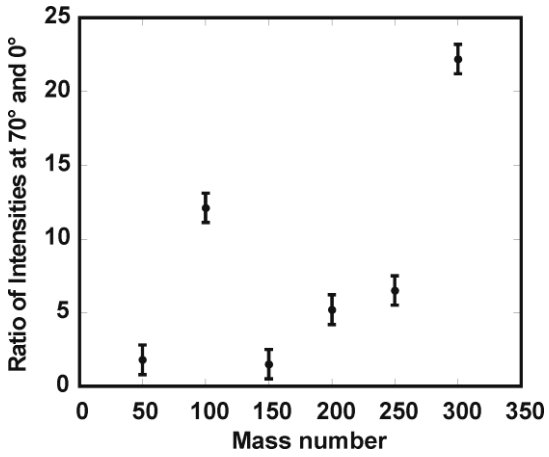

Fig. 4. Ratios of the off-normal signal intensities to the normal signal intensities, measured in the plane perpendicular to the long dimension of the laser spot. Measurements were made at a fluence of to the intensity along the surface normal versus mass number of the neutral fragments measured at a fluence of 820 mJ/cm^2.

The data point for 100 amu in Fig. 4 is anomalously high. This represents the monomer, C_2F_4, which can be produced by photochemical bond scission. It is also the dominant product of thermal decomposition.[8,9] We show below that perhaps 90% of the mass removed during ablation is removed as massive particles that are not resolved by our mass filter. Further, virtually all of these massive particles have off-normal trajectories. If some of these chains are emitted at temperature sufficient to support thermal depolymerization, that would produce an excess of particles at 100 amu in the off normal direction.

Measurements of emission intensity versus angle show a strong dependence on laser fluence. Figure 5 shows the signal intensity observed at different angles, measured relative to the surface normal, at fluences of 520 and 680 mJ/cm^2. Again, the laser beam energy was adjusted to maintain a constant fluence at the sample as the sample was tilted away from the normal inclination. At 520 mJ/cm^2, the most intense emissions are observed at angles near 30° with respect to the surface normal. At 680 mJ/cm2, the most intense emissions are observed near 60°. (The peak in the total energy delivered to the sample, at the largest spot sizes, occurs near 45° in each case.)

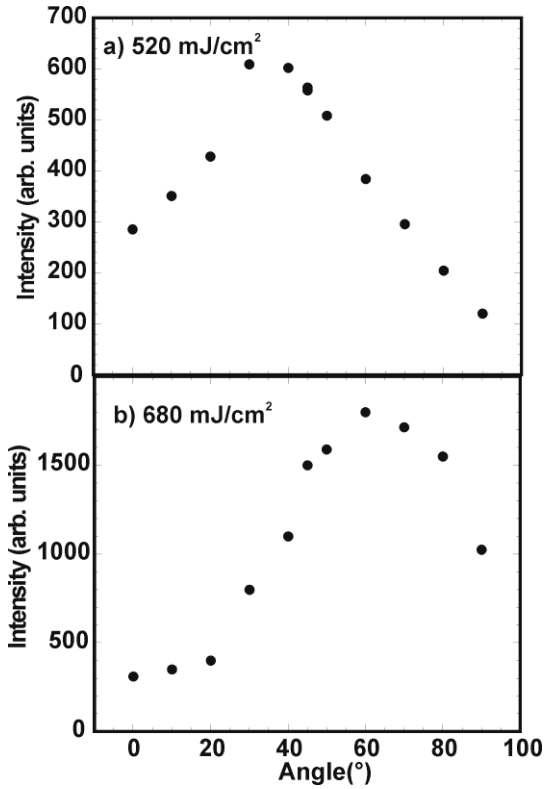

Fig. 5. Intensity of 300 amu signal measured as a function of angle from the surface normal at two laser fluences.

The variation in the direction of peak emission intensities with fluence is consistent with gas dynamics effects, which become more important as the amount of material removed per pulse increases. Increasing the fluence increases the particle densities and pressure gradients in the expanding cloud of gas. These would be responsible for the lateral (off-normal) acceleration experienced especially by the heavier fragments.

Deposition of larger fragments. As noted above, the mass spectrometer employed in this work is not able to resolve particles with masses greater than 300 amu. These fragments are gaseous molecules that are not likely to condense at room temperature. [10] Larger fragments can be collected on substrates mounted close to the laser spot.

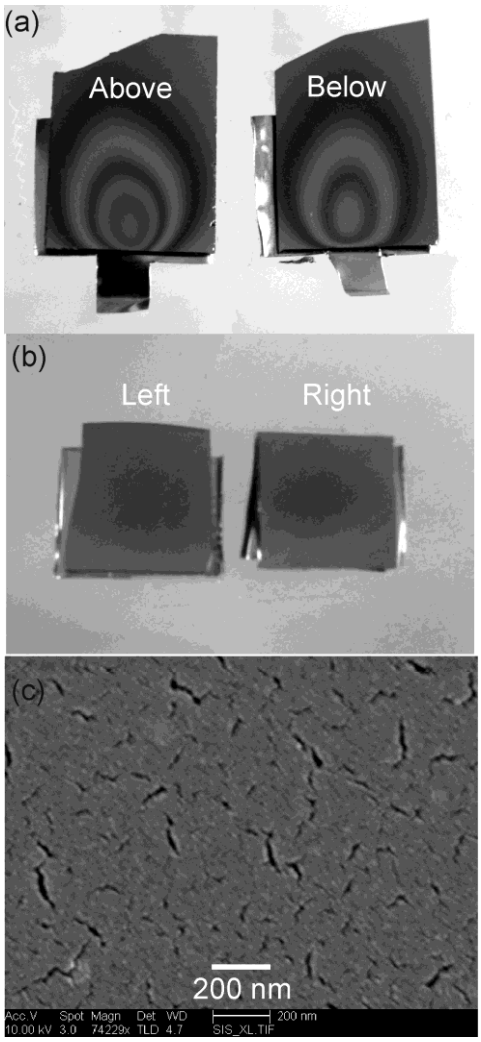

Fig. 6. PTFE films deposited on silicon wafers placed roughly 5 mm from the laser spot, with the plane of the wafer oriented parallel to (a) the long dimension of the laser spot and (b) the short dimension of the laser spot. (c) A scanning electron micrograph of a film deposited on a silicon wafer placed below the laser spot, parallel to the long dimension of the laser spot.

Figure 6 shows visible light images of silicon waters mounted about 5 mm from the laser spot during exposure to about 3000 pulses at a fluence of 900 mJ/cm^2. The wafers in Fig. 6(a) were mounted with the plane of the wafer parallel to the long dimension of the laser spot. These would be oriented so as to collecte the off-normal emissions described above. Significantly, these wafers display clearly visible thin films. The visible light interference fringes are

consistent with maximum thicknesses of about 700 nm. The wafers in Fig. 6(b) which were mounted with the plane of the wafer parallel to the short dimension of the laser spot show no interference fringes, consistent with film thicknesses less than 100 nm.

We note that $(CF_2)_N$ fragments with $N \leq 6$ are volatile at room temperature. [10] Unless these fragments polymerized on contact, they would not be collected. To promote polymerization and crystallization, PTFE films are usually deposited on heated substrates and subsequently annealed at temperatures near 400 °C. [11] Thus the films in Fig. 5(a) are likely formed by much heavier fragments. The film appears to be uniform and dense, with no signs of particulates.

Estimates of the molecular weight of the fragments incorporated into these films were made by differential scanning calorimetry (DSC). Amorphous polymers undergo partial crystallization at temperatures that depend on molecular weight.[12] Figure 7(a) shows a DSC thermograph acquired using a PTFE film deposited directly on to the sample holder—an aluminum pan. As the sample is heated to 400 °C, no distinct feature is observed. This could well be due to volatile components with a range of masses that vaporize gradually as the sample is heated. This is consistent with the sample mass after thermal cycling, which indicated a 94% mass loss.

As the sample was cooled, a small but distinct crystallization peak was observed at 278° C. On a subsequent DSC thermal cycle on the material that remained (shown in Fig. 7(b)) we now see a distinct crystalline melting point at 278 °C as the sample is heated. This crystalline melting point is related to the molecular weight by Flory's equation.[12]:

$$\frac{1}{Tm} - \frac{1}{Tm^0} = \left[\frac{R}{\Delta H_u}\right]\left[\frac{2}{\overline{X}_n}\right] \quad , \tag{1}$$

where T_m is the crystalline melting point in kelvin, $T_m°$ is the melting point of pure CF_2 (600 K), R is the gas constant (2.0 cal/mole/degree), ΔH_u is the heat of fusion per mole of CF_2 units (685

calories) and $\overline{X}_n$ is the number average of CF_2 units. Since the molecular weight of a CF_2 unit is 50 amu, the number average molecular weight (M_n) of the polymer is $M_n = 50\,\overline{X}_n$. Then

$$M_n = \frac{200}{685[\frac{1}{Tm} - \frac{1}{600}]} \tag{2}$$

With T_m = 278 K, the corresponding molecular weight of the residual film is ~ 2000 amu. Since most of the light fragments evaporated during the first heating cycle, we expect that polymerization was minimal. Therefore 2000 amu is most likely a rough upper bound on the mass of the particles deposited on the film during laser ablation.

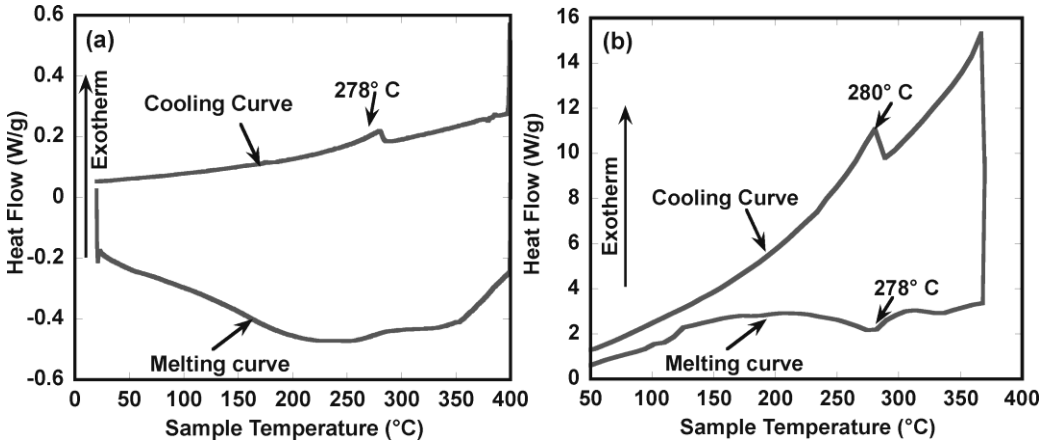

Fig. 7. (a) DSC thermograph of a PTFE thin films deposited on aluminum pans placed 0.5 cm below the laser spot. The heating and cooling rates were 10 °C/min. No distinct melting point is observed but a small crystallization peak is observed and a 94% mass loss was observed other the thermal cycle. (b) DSC thermograph of the residual film showing a distinct melting temperature at 278° C.

Although it is not clear what might limit the fragment size during laser ablation, one possibility is the geometric structure of entanglements in the polymer. In a crude sense, entanglements in amorphous polymers function like cross-links in cross-link polymers: the material between entanglements is tied to the rest of the network by the entanglements. That said, entanglements are not chemical links, but more like tangles. If the polymer chain is broken

into fragments, the chains will disentangle, leaving the fragments free. To remove a given polymer fragment from bulk material, the material between two entanglements must be cleaved twice. In amorphous PTFE, the average chain length between entanglements has a molecular weight of about 4660 amu.[13] With two cleaves between fragments, the average fragment length will be about 2300 amu. (Smaller fragments are readily produced.) This upper limit on the average mass of ablated fragments is somewhat speculative. However, it is consistent with the conjecture that the removal of polymeric material during laser ablation requires a minimum density of cleaved bonds.[14]

We suggest that photochemical bond breaking in PTFE during 157-nm irradiation has cleaved the polymer into $(CF_2)_N$ fragments with masses ranging from 50 amu to 2000 amu.[5]. The average size of the fragments will likely depend on the local laser fluence during exposure: massive fragments are produced at lower laser energy densities, where the number of chain scission per unit volume is low, and light fragments are produced at higher laser energy densities, where the number of chain scission events per unit volume is high. For example, if all the photons available at a fluence of 1 J/cm^2 were randomly distributed within a volume given by the etch depth (400 nm) and the laser spot size (0.065×0.16 cm^2), and if every photon cleaved the polymer chain, the average fragment size would be 100 amu. Fluences above 1.5 J/cm^2 would be required to produce average fragment sizes of 50 amu, and fluences below 0.5 J/cm^2 would produce average fragment sizes greater than 200 amu.

The energy density associated with a Gaussian laser beam is distributed in a non-uniform fashion across the laser spot, with higher energy densities in the center of the spot and lower densities in the wings. Thus we anticipate that lighter fragments are produced near the center of the laser spot, where the density of cleaved bonds is highest, and heavier fragments toward the edges of the laser spot, where the density of cleaved bonds in lower. We believe this non-uniform distribution of particle sizes plays an important role in the evolution of off-normal emission.

3.1 Hydrodynamic simulations.

To account for the intense off-normal emission of heavier PTFE fragments, we propose that light fragments generated near the middle of the laser spot form a high pressure region of expanding gas that drives the heavier fragments to the side. To test the viability of this thesis, we modeled this expansion with a conventional 2-D gas dynamics algorithm previously used to describe plume expansion in vacuum.[15] The algorithm solves a system of three coupled differential equations that account for the conservation of mass, momentum and energy:

$$\frac{\partial}{\partial t}\begin{Bmatrix}\rho \\ \rho\vec{v} \\ \rho e+\frac{1}{2}\rho v^2\end{Bmatrix}=-\nabla\cdot\begin{Bmatrix}\rho\vec{v} \\ P+\rho\vec{v}\cdot\vec{v} \\ \vec{v}(\rho e+\frac{1}{2}\rho v^2+P)\end{Bmatrix}, \tag{3}$$

where ρ is the mass density of the particles in a cell, $\vec{v}$ is their vector velocity, *e* is their internal energy per unit mass, and *P* is the pressure. The pressure was calculated from an ideal gas equation of state:

$$P=(\gamma-1)\rho e=\rho_N k_B T \tag{4}$$

where γ is the ratio of specific heats and ρ_N is the number density of particles in a given cell. For simplicity, we use the ideal gas value, γ = 5/3 (an upper bound). The mass, momentum, and energy distributions were solved for points on a square, 100 × 100 point grid, representing a 10 × 10 cm^2 area in real space. This model was numerically implemented using finite differences in Cartesian coordinates and the Rusanov scheme in time.[15]

The simplest system we have found that reproduced the strong off normal emission for heavy fragments involved a two-component gas, with light fragments originating from the center

of the laser spot and heavy fragments from the edges of the laser spot. In the results presented below, the peak density of the light fragments was set to 10^{19} cm^{-3}; assuming 100 amu fragments, this corresponds roughly with our etch rates estimates. The light fragments are represented by a Gaussian distribution in density and temperature, with a half width of 3 grid points in each direction. (These dimensions correspond to the most intense 0.016×0.09 cm^2 region of the 0.065×0.18 cm^2 laser spot.) The heavier fragments are represented by a two Gaussian distribution, one centered 2 grid points above and the other two grid points below the center of the laser spot. The peak heavy-particle density was half the peak light-particles density: 0.5×10^{19} cm^{-3}. For both light and heavy particles, the initial peak temperatures were set to 6600 K (corresponding to 0.6 eV) and the initial vector velocities were set to zero. Although the light-particle density was greater than the heavy-particle density, the light particles made up only a tenth of the total emitted mass: most of the ablated material is removed as heavy fragments.

We neglect interactions between the laser and the ejected material. PTFE oligomers with masses less than about 15,000 amu are not expected to absorb significantly at 157 nm.[16] This is well above the 2000 amu upper bound on average mass determined by DSC. Indirect heating by inverse bremsstrahlung electron heating is also expected to be negligible, in part due to the short wavelength of the VUV photons (absorption is proportional to λ^{-3}) and in part due to the relatively low electron densities among the emitted particles.

Density profiles for both light and heavy particles are shown in Fig. 8 at times corresponding to 0, 5 and 10 μs after the laser pulse. While the expansion of the light fragments is mainly forward directed, the expansion of the heavier fragments is almost parallel to the surface. This trend in the expansion is due to the pressure gradients associated with the particle distribution. The heavy fragments are squeezed in between the surface and the light fragments. The heavy-particle density profile in Fig 8(a) at t=10 μs immediately opposite the laser spot is almost flat. If a substrate were placed in front of the laser spot, the resulting deposition should be almost uniform in the central regions. It is possible that exceptionally uniform thin films can

be produced over relatively larger areas if the above conditions are created in the plume. Greater control over the particle masses in each region could presumably be obtained by overlapping two or more laser beams with uniform intensity profiles. Others have proposed that multiple plumes can be used to achieve thin-films over larger coverage areas.[15]

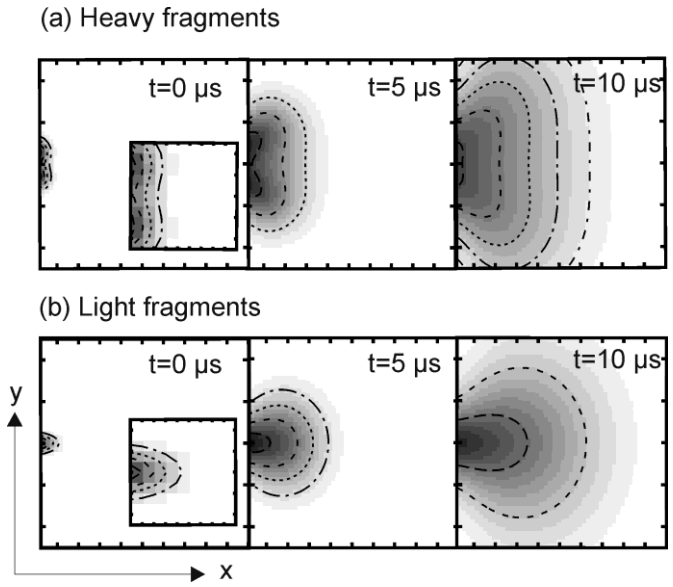

Fig. 8. Calculated density profiles for (a) heavy and (b) light fragments at time 0, 5 and 10 μs after the laser pulse. The edges of each box are 50 grid points long, equivalent to 2.5 cm. The insets for $t = 0$ show the initial densities on an expanded scale; the edges of the inset box correspond to a distance of 0.5 cm.

The effect of pressure gradients is more clearly seen in plots of the particle acceleration vectors at the end of the laser pulse. This acceleration a is given by:

$$a = -\frac{1}{\rho}\nabla P \,. \tag{5}$$

Figure 9(a) shows the heavy-particle densities and accelerations that would apply in the absence of the light particles. Figure 9(b) shows the light-particle densities and accelerations that would apply in the absence of the heavy particles. In both cases, these initial accelerations are mostly

forward directed. Figure 9(c) shows the total particle densities and accelerations as a function of space in the presence of both particles. With both particles, the magnitude of the accelerations are generally greater. Further, the acceleration of particles lying near the sides of the laser spot (principally slow, heavy fragments) is almost parallel to the surface. The model suggests that a distribution of particle sizes is required for off-normal acceleration.

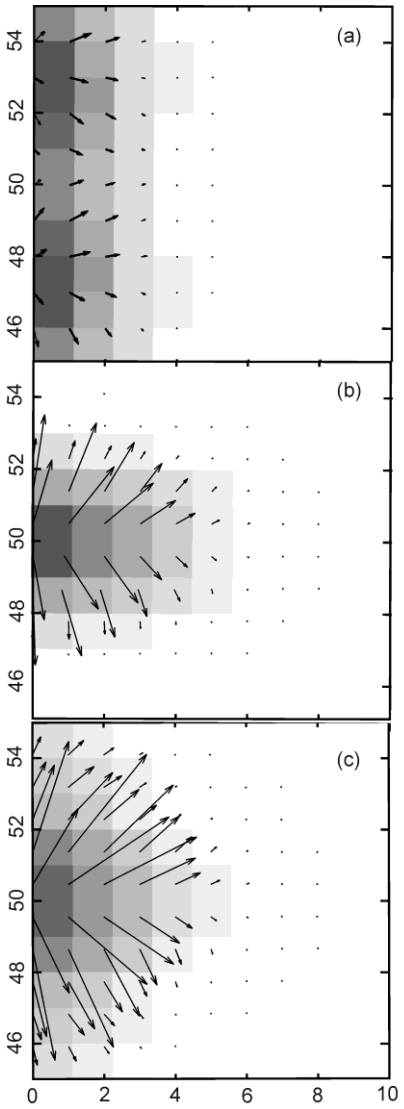

Fig. 9 Calculated density plots and acceleration vectors immediately after the laser pulse for (a) the heavy fragments alone; (b) the light fragments alone; and (c) a superposition of both light and heavy particles.

Varying the ratio between light and heavy particles significantly affects the heavy-particle trajectories. Figure 10 shows heavy-particle density profiles at time t = 10 μs after the laser pulse for 0.1×10^{19} cm^{-3}, while the light particle density is raised from 0.1×10^{19} cm^{-3} to 0.5×10^{19} cm^{-3} to 1×10^{19} cm^{-3} . As the light-particle fraction increases, the heavy-particles are increasingly directed away from the surface normal. As we increase the fluence the light-particle densities increase faster than the heavy-particle densities. These calculations are consistent with what we observe experimentally where as we raise the fluence we see heavy-particles being pushed further away from the normal (Fig. 5) .

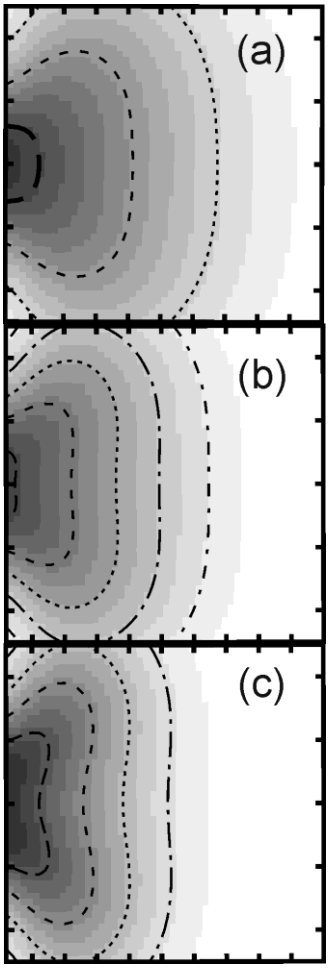

Fig. 10. Calculated heavy-particle density distributions at t =10 μs after the laser pulse, where the heavy-particle density is fixed at 0.1×10^{19} cm^{-3}. The light-particle densities increase from (a) 0.1×10^{19} cm^{-3} to (b) 0.2×10^{19} cm^{-3} to (c) 1×10^{19} cm^{-3}.

Off-normal trajectories also require that the light and heavy particles have contrasting spatial distributions. Figure 11 show calculated heavy-particle density distributions for t = 10 μs after the laser pulse with two different initial heavy-particle distributions. In each case, the initial peak heavy particle density is 10% of the initial peak light particle density. With initial the heavy and light particle densities overlap strongly, the heavy particle densities are principally forward directed. When the initial heavy-particle distribution extends well above and below the initial light particle distribution, the heavy particles develop strong off-normal trajectories.

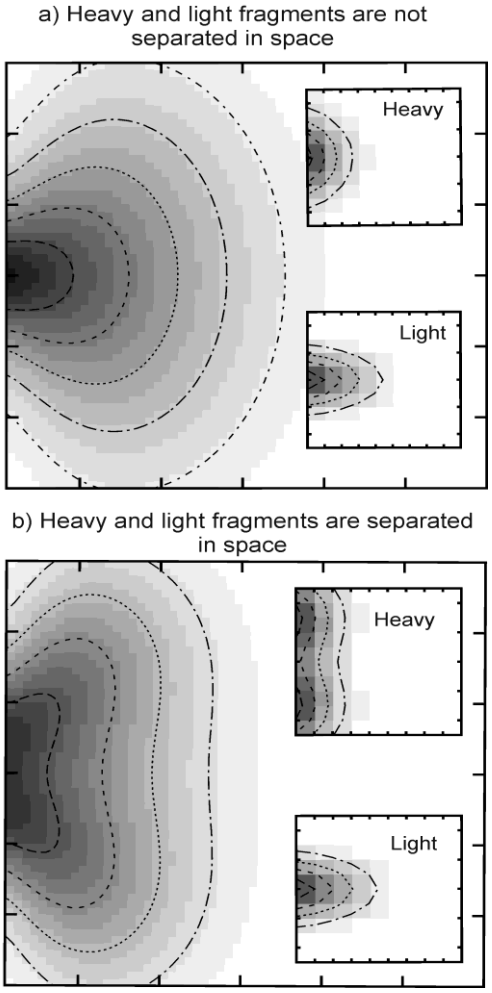

Fig.11 Calculated heavy-particle density distributions at t = 10 μs after the laser pulse corresponding to two with different initial heavy-particle distributions. The initial density distributions are shown on expanded scales in the insets. In (a) the two particle distributions overlap strongly in space. In (b), the two distributions are well separated.

Homogeneous mixtures of heavy and light particles do not allow for strong off-normal trajectories. This is consistent with the virtual lack of off-normal emission in Fig. 1(b), acquired using a flat-topped beam intensity profile. A uniform intensity yields homogeneous particle distributions. In this case, the particle distributions are forward directed at all masses. In contrast, the expected inhomogeneous particle density distributions produced by the Gaussian beam allow from strong off-normal emissions, especially for particles with high masses.

4. Summary and Applications

Ablation of PTFE under 157-nm yields primarily $(CF_2)_N$ fragments ranging from 50 amu to 2000 amu. The photochemical bond breaking in PTFE at random point along the main chain gives rise to these fragments [5] We suggest that the number of chain scission events affects the size of the fragments; massive fragments are produced when there are fewer chain scission events and lighter fragments when there are many chain scissions. The broad range of emitted masses during 157-nm ablation of PTFE is unique and unlike laser ablation for other materials where the ablation products are made up of only a few masses.

The presence of light and heavy fragments in emitted fragments during ablation gives rise to some unique and unusual behavior in the way it expands. We have shown in this article that heavy fragments are emitted away from the surface normal, almost parallel to the surface. We propose that this behavior is due to pressure gradients created within the cloud of emitted fragments due to which heavy fragments are accelerated away from the surface normal. These pressure gradients arise due to the Gaussian beam profile of the F_2 excimer laser. The higher density of photons in the center of the laser spot would result in many chain scission events in this region and therefore produce lighter mass fragments. Conversely, fragment size increases as we move away from the center of the laser spot. The gradient in the intensity of the beam is more pronounced along the shorter dimension of the laser spot and with more fragments in the

center than at the edges this creates a pressure gradient along this direction resulting in heavier fragment being pushed off to the sides along this direction.

2-dimensional hydrodynamic calculations of plumes with two components (high pressure light fragments and low pressure heavy fragments) support our contention. From our calculations we have found that a separation in space of the two components is required for this kind of behavior. The separation gives rise to a pressure gradient which in turn provides the forces required to accelerate the heavy particle away from the normal and almost parallel to the surface. Our calculations also show that when there is no separation of the heavy and light fragments and we have a homogeneous mixture of the two in the emitted fragments, this behavior is not observed. This is again consistent with what we observe experimentally when we used a uniform laser beam. These calculations also reveal that by creating the above conditions in the plume one can obtain high quality uniform thin-films of PTFE over large areas. Also, as we have shown off-normal deposition (as opposed to the conventional on-normal deposition) also might be attractive for pulsed laser deposition applications.

Acknowledgment

This work was supported by the U.S. Department of Energy under Grant DE-FG02-04ER-15618.

References

[1] J. Cashmore, M. Gower, P. Gruenewald, D. Karnakis, and M. Whitfeild, in *High-resolution micromachining using short wavelength and shortpulse lasers*, Chiba, Japan, 1993, p. I-292-I-293.

[2] M. Fiebig, M. Kauf, J. Fair, H. Endert, M. Rahe, and D. Basting, "New aspects of micromachining and microlithography using 157-nm excimer laser radiation," Appl. Phys. A **69,** S305 (1999).

[3] P. R. Herman, K. P. Chen, M. Wei, J. Zhang, J. Ihlemann, D. Schafer, G. Marowsky, P. Oesterlin, and B. Burghardt, "F_2-lasers: High-resolution micromachining system for shaping photonic components," Conference on Lasers and Electro-Optics**,** 574-577 (2001).

[4] A. Costela, I. Garcia-Moreno, F. Florido, and J. M. Figuera, "Laser ablation of polymeric material at 157 nm," J. Appl. Phys. **77,** 2343-2350 (1995).

[5] S. R. George, J. A. Leraas, S. C. Langford, and J. T. Dickinson, "Interaction of 157-nm excimer laser radiation with fluorocarbon polymers," Appl. Surf. Sci. **255,** 9558-9561 (2009).

[6] K. Mann, in *Excimer Laser Technology*, edited by D. Basting and G. Marowsky (Springer, Berlin, 2005), p. 106-117.

[7] R. Kelly, "On the dual role of the Knudsen layer and unsteady, adiabatic expansion in pulse sputtering phenomena," J. Chem. Phys. **92,** 5047-5056 (1990).

[8] S. L. Madorsky, *Thermal Degradation of Organic Polymers* (Interscience Publishers, New York, 1964).

[9] W. J. Welsh, in *Physical Properties of Polymers*, edited by J. E. Mark (American Institute of Physics, Woodbury, New York, USA, 1996), p. 605-614.

[10] H. H. Anderson, "Boiling points and boiling point numbers of perfluoroalkanes and perfluoroalkenes," J. Chem. Engin. Data **10,** 156–159 (1965).

[11] N. Huber, J. Heitz, and D. Bauerle, "Polytetrafluoroethylene (PTFE) films prepared by F2-Laser deposition," Eur. J. Appl. Phys. **29,** 231-238 (2005).

[12] P. J. Flory, *Principles of Polymer Chemistry* (Cornell University, Ithaca, New York, 1953).

[13] L. J. Fetters, D. J. Lohse, and R. H. Colby, in *Physical Properties of Polymers Handbook*, edited by J. E. Mark (American Institute of Physics, Woodbury, NY USA, 1996), p. 335-340.

[14] E. Rebollar, G. Bounos, M. Oujja, C. Domingo, S. Georgiou, and M. Castillejo, "Influence of polymer molecular weight on the chemical modifications induced by UV laser ablation," J. Phys. Chem. B **110,** 14215-14220 (2006).

[15] J. N. Leboeuf, K. R. Chen, J. M. Donato, D. B. Geohegan, C. L. Liu, and A. A. Puretzky, "Modeling of plume dynamics in laser ablation processes for thin film deposition of materials," Phys. Plasmas **3,** 2203 (1996).

[16] K. Seki, H. Tanaka, T. Ohta, Y. Aoki, A. Imamura, H. Fujimoto, H. Yamamoto, and H. Inokuchi, "Electronic structure of poly(tetrafluoroethylene) studied by UPS, VUV absorption, and band calculations," Phys. Scripta **41,** 167-171 (1990).

CHAPTER SIX

Transient absorption in CaF_2 under 157-nm laser irradiation

Sharon R. George, S. C. Langford and J. T. Dickinson

Abstract

We report transient changes in VUV and UV transmission in single crystal calcium fluoride during intermittent exposure to 157-nm excimer laser radiation at fluences near 1 J/cm^2. The amplitudes of the transient changes peak near 153 nm, 220 nm and 375 nm. We attribute these changes to the production and decay of the substitutional hydrogen ion (H_S^-), interstitial (anti-site) Ca^+, and the F-center in CaF_2. 157-nm excimer radiation also produces persistent coloration in the crystal at 160, 375, and 560 nm. Persistent absorption at 560 nm is due to metallic calcium nanoparticles that form under the conditions of this work. The persistent darkening at 160 nm and 550 nm are related, implying that the 160 nm absorption is also due to metallic calcium nanoparticles. This would be a manifestation of the VUV surface plasmon peak in metallic calcium. The possible use of transient VUV and UV transmission measurements as a probe of hydrogen and lattice disorder are discussed.

1. Introduction

CaF_2 is an ionic crystal with a band gap of 11.8 eV. This wide band gap contributes to the damage resistance of this material, which is much greater than fused silica at wavelengths less than 200 nm. That said, the optical properties of CaF_2 can be degraded by two-photon process at 157 nm that generate defects, including vacancy-interstitial pairs. F-center aggregation can lead to the production of metallic Ca nanoparticles.[1] On occasion, transient absorption features have been observed during 157-nm[1] and 193-nm[2] excimer laser radiation.

In previous work, we have reported measurements of transient changes in transmission due to the production and decay of defects produced by femtosecond laser radiation in the alkali halides and soda lime glass.[3-5]

In this work, we report transient VUV and UV transmission measurements during 157-nm irradiation in CaF_2 with absorption peaks at 153 nm, 220 nm and 375 nm. The absorption near 153-nm is consistent with absorption due to the substitutional hydride ion, H_s^-. Consistent with this identification, this absorption is strengthened by high temperature annealing in hydrogen gas. We attribute the absorption near 220 nm to the interstitial (anti-site) Ca^+ ion (Ca_I^+), and the absorption near 375 nm to the F-center. Absorption at these wavelengths gradually increases during 157-nm irradiation at fluences above 1 J/cm2. When irradiation is terminated, the absorption gradually disappears. However subsequent irradiation quickly restores the absorption to its previous maximum value.

We propose that charge transfer to and from substitutional H_s^- and Ca_I^+ centers can rapidly change the absorption intensities at 153 and 220 nm. This charge transfer is facilitated in the presence of ionizable electron traps, including the F and M centers, which are produce during 157-nm irradiation. The growth of absorption during irradiation is reasonably described by assuming that absorbing centers are produced at a constant rate during irradiation, and that they are destroyed by recombination processes both during and after irradiation. For the F-center

we propose that aggregation of F-centers to form M-centers leads to loss of absorption at 375 nm and the dissociation of the M-center when irradiation is restored re-induces absorption.

We also see persistent changes in the absorption spectrum due to 157-nm irradiation at 160 nm and 560 nm which we attribute to formation of Ca nanoparticles or colloids as they are sometimes called. These particles are formed due to aggregation of F-centers that result in Ca rich regions in the crystal and leads to the formation of Ca nonopaticles. The transient absorption features are superimposed on these permanent changes in transmission.

2. Experiment

VUV grade CaF_2 from Korth Kristalle GmbH was cleaved in air along the (111) plane into 1-mm thick, 1-cm diameter disks. The samples were used either as cleaved or after polishing in methanol with 5 μm SiC abrasive. Some cleaved samples were also annealed in H_2, O_2, or air at 500 °C for 2 hrs. Experiments were carried out at pressures less than 1×10^{-6} Pa. Twenty nanosecond pulses of 157-nm radiation were provided by a Lambda Physik LPF 200 F_2 excimer laser. Unless otherwise mentioned the laser was operated at a repetition rate of 10 Hz.

VUV spectra were obtained using a 302 McPherson UHV VUV spectrophotometer equipped with a Hamamatsu deuterium lamp. Transmission at a given wavelength was monitored as a function of time by setting the spectrophotometer to pass a fixed range (~ 2 nm of wavelengths) and monitoring the output with photomultiplier tube.

3. Results

Persistent transmission changes during irradiation. During prolonged exposure to 157-nm excimer laser radiation, the VUV and UV transmission of CaF_2 gradually drops over a wide range of wavelengths, as shown for cleaved CaF_2 at 157 nm in Fig. 1. The transmission was monitored once per second during exposure at a fluence of 2.1 J/cm^2 per pulse at pulse

repetition rate of 10 Hz. The transmission at 157 nm falls in a near-linear fashion over the entire 10,800 pulse duration of exposure. Under these conditions, the transmission will continue to fall in a linear fashion, at constant slope, even after 100,000 pulses of continuous irradiation. Measurements at other fluences show that the slope of the linear drop increases in a nonlinear fashion with fluence. When laser exposure is terminated, the transmission partially recovers.

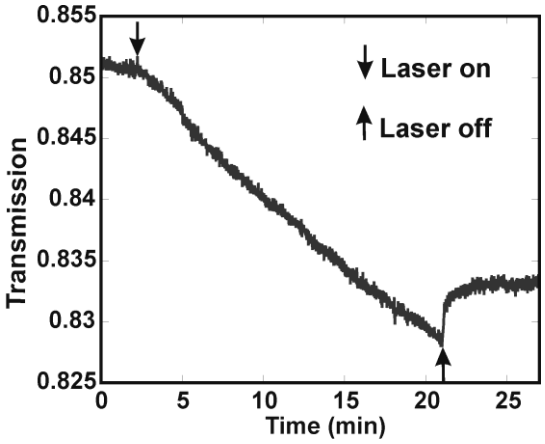

Fig. 1. Transmission of CaF_2 at 153 nm, measured once per second during 157 nm irradiation at 10 Hz and a fluence of 2.2 J/cm^2.

The UV VIS absorption spectrum of CaF_2 *after* exposure to about 100,000 pulses at 2.1 J/cm^2 is shown in Fig. 2, along with the spectrum acquired in an unexposed region of the same sample. The apparent absorption edge near 120 nm in both spectra is not due to the band edge, which is expected near 103 nm. The broad peak centered near 560 nm is attributed to calcium metal nanoparticles.[6-8] The shoulder on the short wavelength side of this peak, near 375 nm, is attributed to F-centers. We attribute most of the absorption in the unexposed region to Rayleigh scattering from surface irregularities, which scales as λ^{-4}. When this spectrum is subtracted from the spectrum of the colored material, a major feature appears near 160 nm in the VUV (shown in the inset).

To our knowledge, all the previously reported CaF_2 absorption features in the VUV region are attributed to impurities. Although the H_S^- center absorbs in this regions, we show

below that this absorption saturates during prolonged exposure. In contrast, the intensity of the persistent feature at 160 nm grows continuously throughout the longest exposures employed in this work. We cannot attribute the persistent 160-nm absorption to H_S^- centers.

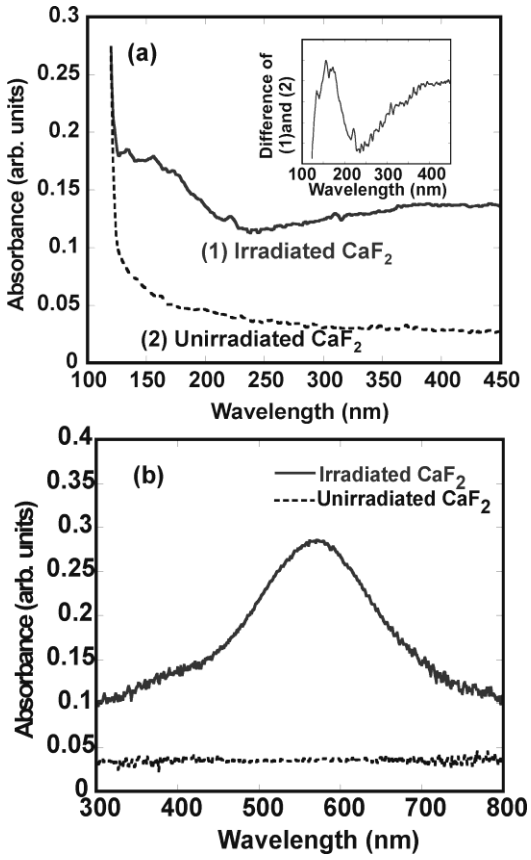

Fig. 2. (a) VUV absorption spectra of cleaved, unirradiated CaF_2 after exposure to about 100,000, 157-nm laser pulses at a fluence of 2.1 J/cm^2. The difference between the two spectra is shown in the inset. (b) UV-VIS absorption spectrum of a different cleaved CaF_2 also exposed to about 100,000 pulses of 157-nm excimer laser radiation at 2.1 J/cm^2 per pulse.

In previous work, we predicted that metallic calcium nanoparticles absorb in the 120-200 nm region due to the presence of a VUV surface plasmon.[9] Calcium metal is unusual in that it displays two bulk and two surface plasmons.[10] Mie scattering associated with the other plasmon (near 560 nm) has been relatively well characterized.[6-8,11-15] The absorption peak of calcium

nanoparticles with radii of about 6 nm is expected near 560 nm.[12] As the colloid radii grow, the absorption shifts to longer wavelengths.

If the absorption at 160 nm is due to calcium nanoparticles, the transmission at 160 nm and 560 nm will behave in the same way during prolonged 157-nm exposure. Unfortunately, the intensity of our D_2 lamp is insufficient for measurements at 560 nm. Transmission measurements were performed at the nearby wavelength of 490 nm. Figures 3(a) and 3(b) compare the transmissions at 153 and 490 nm during prolonged irradiation. The transmission at both wavelengths drops linearly with fluence. Significantly, the recovery of transmission at 490 nm when the laser is turned off is very small, consistent with absorption due to scattering due to nanoparticles, as opposed to less stable defects, including F-centers. The transmission at 490 nm wavelength appears to be a suitable proxy for transmission at 560 nm as a probe of the colloid density.

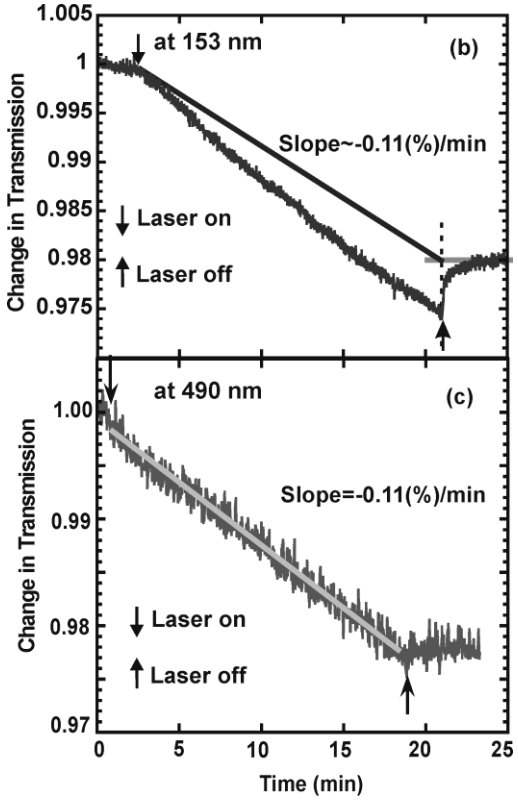

Fig. 3. (a) Transmission of cleaved CaF_2 at 153 nm and (c) 490 nm during a 12,000 pulse exposure at the same fluence.

The absorption spectra of Fig. 2 leads us to expect similar transmission drops at each wavelength, and this is observed—*if* the recovered portion of transmission drop is removed from the trend at 153 nm. The persistent portion of the transmission drop at 153 nm is indicated by the dark line in Fig. 3(a). The continuous drop in transmission shows the same trend at both wavelengths. We therefore suggest that persistent absorption around 153 nm is due to Mie scattering from calcium metal nanoparticles associated with the VUV surface plasmon. On close inspection of the two curves, the percentage drop in transmission over 10,800 pulses is roughly the same at both wavelengths – this is a coincidence as we do not expect the same amount of absorption due to the two plasmons.

The VUV and UV-VIS spectra of Figs. 2(a) and 2(b) display significant differences in the region of overlapping wavelengths. In the UV-VIS spectrum, the absorption increases markedly between 300 and 450 nm; while in the VUV spectrum, the absorption in this region is relatively flat. This suggests that the colloid sizes and/or densities are significantly lower during the acquisition of the VUV spectrum. Interestingly, Bennewitz *et al*. found that nanoparticles produced by exposing CaF_2 to 2.0-2.5 keV electrons grow significantly after exposure stops and shrink reversibly when electron exposure is resumed.[16] This effect was attributed to the absorption of electrons by the nanoparticles,[16] which promotes fluorine transport into the nanoparticles and reduces their size.

We have shown that low-fluence F_2 excimer laser radiation has a similar effect on nanoparticles produced by electron irradiation.[9] Exposing material colored by 2 keV electrons to 10 mJ/cm^2 pulses of 157-nm radiation at 20 Hz (average flux at sample 200 mW/cm^2) for 30 minutes reduces the colloid absorption at 532 nm by almost half. This treatment presumably heats nanoparticles by absorption into the VUV surface plasmon band, resulting in shrinkage. During the acquisition of the VUV spectrum in Fig. 2, the sample was continuously exposed to VUV radiation from the D_2 lamp, including radiation into the 160-nm band. This may have been sufficient to shrink or suppress colloid growth. We show

Transient changes in transmission. Along with these persistent changes we also observe transient changes in absorption. Figure 4(a) shows transmission measurements for a cleaved, previously unexposed, sample at 153 nm. The sample was exposed to 2.1 J/cm^2 pulses at a pulse repetition rate of 10 Hz. Three minute periods of 157-nm exposure were alternated with three minute periods without exposure. Again, the transmission was monitored at one-second intervals. The transmission drops when the laser is turned on and partially recovers when it is turned off. These transient changes are superimposed on a steadily decreasing, persistent drop. As noted above, we attribute the persistent drop in transmission at 153 nm to absorption into the VUV calcium metal colloid band near 160 nm. Below, we focus on the transient portion of the transmission drop—the part that recovers after laser exposure.

The amplitude of the transient transmission drop accompanying the resumption of laser exposure at 153 nm starts small and increases until it reaches a steady state. Under these conditions, the amplitudes of the drop and recoveries become fairly consistent after total exposures of about 12,000 pulses. The inset in Fig. 4(a) shows a superposition of two transmission signals acquired during laser on-off cycles—one starting after a total exposure of about 14000 pulses and the other starting 5,000 pulses later. To remove the effect of persistent transmission change, the signals have been displaced vertically. The strong overlap indicates that the transient changes during laser on/off cycles are quite consistent from one cycle to the next. The total exposure required to attain cycle-to-cycle consistency decreases as the fluence increases.

To characterize the transient changes, we measure three transmission values associated with a laser on/off cycle as shown in Fig. 4(b). We refer to the transmission immediately prior to the onset of exposure as the initial transmission, T_i. We designate the transmission value immediately after the fast drop accompanying the onset of exposure as the re-induced transmission, T_{RA}; this fast drop is usually spread over about forty pulses, or four seconds at a pulse repetition rate of 10 Hz. After the fast drop, the transmission continues to drop slowly—but this gradual change contributes mainly to the persistent changes described above. The

transmission immediately before laser exposure is terminated is designed the final transmission, T_f. Finally, the transmission partially recovers over a time Δt to the recovered value of transmission, T_r. At 153 and 220 nm this recovery is virtually complete after Δt = 180 s. Given sufficient exposures, the differences $T_i - T_{RA}$ and $T_r - T_f$ measured at 153 and 220 nm are reproducible from cycle to cycle.

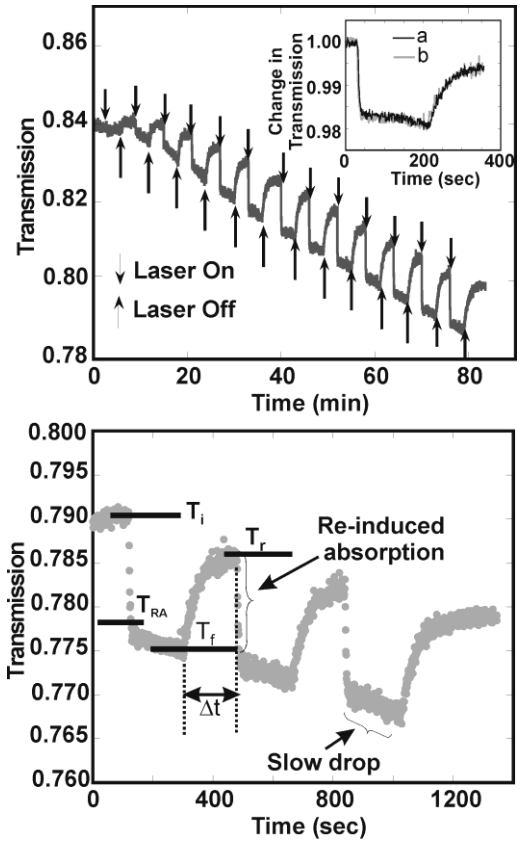

Fig. 4. (a) Changes in transmission at 153 nm measured once per second while cycling the laser on and off at a fluence of 2.1 J/cm^2. In the inset, two transmission cycles are superimposed by shifting them both to the same initial intensity: one starting after a total exposure of about 14,000 pulses and the other starting 5,000 pulses later. (b) Three laser on-laser off cycles at the same fluence and repetition rate and defines four parameters used to characterize the transient changes: T_i is the transmission immediately prior to the onset of an exposure cycle, T_{RA} is the transmission immediately after the fast initial drop, T_F is the transmission at the end of an exposure cycle, and T_r is the transmission after time Δt, when recovery is virtually complete.

Figure 5 shows a plot of $T_i - T_{RA}$ values measured at a fluence of 2 J/cm^2. Measurements were made at 2-5 nm intervals between 120 and 450 nm. The transient absorption peaks near three wavelengths: 153, 220, and 375-nm. As shown in the inset, the spectrum defined by plotting $T_r - T_f$ versus wavelength shows very similar features. This is consistent with the expectation that $T_i - T_{RA}$ is proportional to $T_r - T_f$ for reproducible transient absorption features.

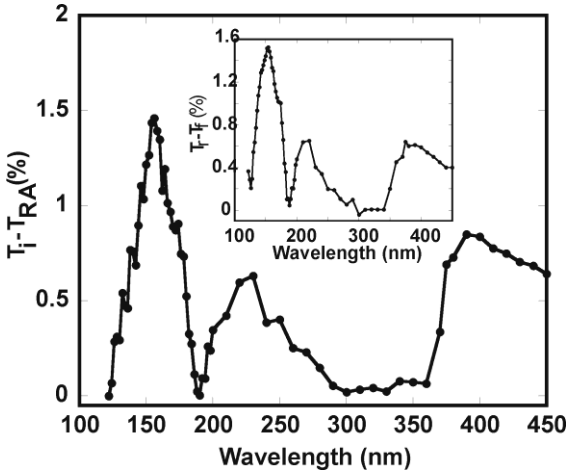

Fig. 5. Transient absorption spectrum obtained by plotting $T_i - T_{RA}$ as a function of wavelength. The corresponding spectrum obtained by plotting $T_r - T_f$ is shown in the inset. $T_r - T_f$ reflects the transmission change at the end of a laser exposure cycle (transmission recovery), and $T_i - T_{RA}$ reflects the transmission change at the beginning of a laser exposure cycle.

The peak near 153 nm is consistent with the H_s^- center absorption, reported at 161 nm by Beaumont et al.[17] All CaF_2 crystals contain trace amounts of hydrogen, but the low concentration is hard in detect spectroscopically. The H_s^- center an H^- ion that occupies an F^- ion site in the CaF_2 lattice. Bessent *et al*. suggest that the neutral analog of the H_s^- center occupies an interstitial site at room temperature, an—H_I^0 center.[18] Since we do not observe H_s^- absorption in as-received samples, hydrogen presumably occupies interstitial sites prior to irradiation. Thus the initial formation of H_s^- centers may involve the production of fluorine vacancies i.e. F-center. Hydrogen then moves into these vacancies and traps an electron then becomes H_s^-. This would also explain the increase in the magnitude of the transient absorption

at 153-nm with prolonged irradiation. (We show later that the transient H_s^- center absorption is related to the F-center formation). It is likely that subsequent charge transport to and from these hydrogen atoms is accompanied by the motion of the hydrogen atom between interstitial and substitutional sites. The hydrogen hopping motion can be rapid on time scales of minutes.[18]

We propose that the transient transmission changes are due to the reactions:

$$H_i^0 + e^- \rightarrow H_s^- \quad (1a)$$

$$H_s^- + h^+ \rightarrow H_i^0 \quad (1b)$$

The principal hole center in CaF_2 is the V_k center—essentially a F_2^- molecular ion associated with a fluorine vacancy. V_k centers are mobile at temperatures above 173 K,[19] and can be stabilized at higher temperatures by impurities.

The transient absorption near 220 nm is consistent with the Ca^+ ion at an interstitial site (Ca_I^+ defect), reported by Massner and Smakula.[20] The Ca^{2+} interstitial is a disorder-related defect; if this defect traps an electron, it becomes a Ca_I^+ defect that absorbs near 220 nm. The formation energy of a Ca^{2+} interstitial/vacancy pair is expected to be about 7.5 eV[21,22]—much higher than the energy required to form the F– interstitial pair (2.7 eV). We believe that calcium interstitial defects are present in the crystal as grown, and that the transient transmission changes are produced by charge transfer only. The increase in the transient absorption during the early stages of irradiation is presumably due to the increase in electron traps like F-centers with continued irradiation. We attribute the transmission recovery during the off portion of a laser on/off cycle to hole trapping at a Ca_I^+ center to form non-absorbing Ca_I^{2+} center. The proposed reactions responsible for the transient transmission signals observed at 200 nm are:

$$Ca_I^{2+} + e^- \rightarrow Ca_I^+ \quad \text{and} \quad (1a)$$

$$Ca_I^+ + h^+ \rightarrow Ca_I^{2+} \quad . \quad (1b)$$

The peak at 375 nm is consistent with absorption due to the F-center,[23] which corresponds to an electron trapped in a fluorine vacancy. F-center formation at 157-nm occurs by a two-photon process via the formation of F-H pairs.[15] The recovery of transmission at 153 nm can take place by two processes: recombination with fluorine interstitials and aggregation with other F-centers and F-center aggregates. F-centers are mobile at room temperature and readily aggregate.[11,14,15,24] In the limit of large aggregates, the latter process produces the nanoparticles responsible for much of the persistent transmission change at this wavelength.[6-8,11-15]

To compare the transient absorption features at 153 nm, 220 nm and 375 nm, we plot transmission signals acquired at a fluence of 2.3 J/cm^2 in Fig. 6. These signals were acquired after a 12,000 pulse exposure to ensure reproducible changes. The change is largest at 153 nm (about 2 %), weakest at 220 nm (less than 1 %), and intermediate at 375 nm (about 1.5%). The kinetics of the transmission changes at 153 and 220 nm are quite similar, and contrast markedly with the kinetics of the transmission changes at 375 nm. In the recovery stage, transmission reaches about 70% of the value before exposure in 180 s at 153 and 220 nm [Figs. 6(a) and 6(b)]. At 375 nm, this degree of recovery requires about 600 s [Fig. 6(c)]. [Note the longer time scale in Fig. 6(c).]

Transmission measurements at lower pulse repetition rates (e.g., 1 Hz) yield very similar signals after comparable total exposures (number of pulses). Therefore, these transmission signals are not affected by possible cumulative heating during prolonged exposure.

Similar to the changes observed at 153 nm (Fig 4(a)) the drop and recovery saturates after a certain amount of irradiation at 220 nm but at 375 nm, even over 50000 pulses no such saturation was observed. This suggests that as we create more defects that absorb at this wavelength, the greater the changes observed when irradiation is turned on and turned off.

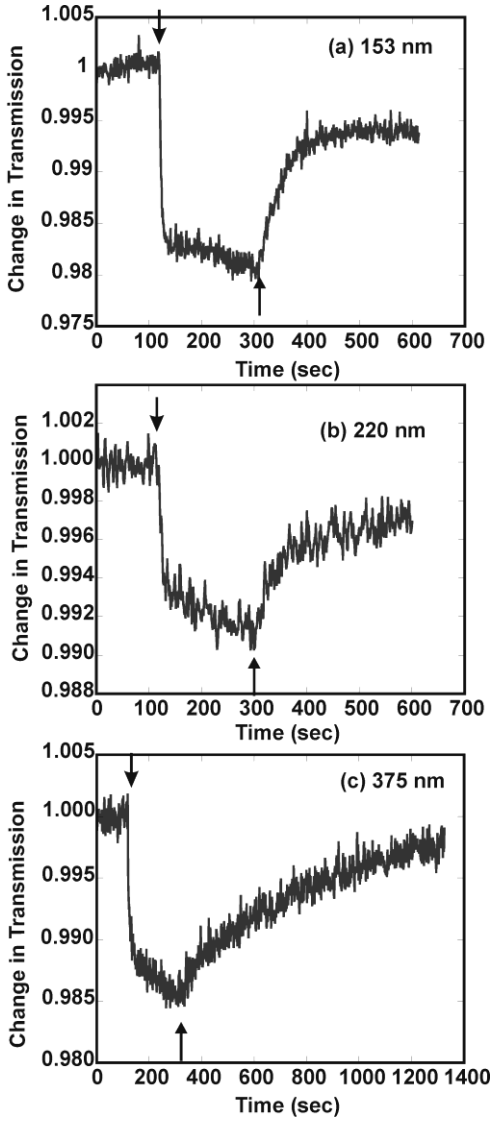

Fig. 6. Transmission signals at (a) 153 nm, (b) 220 nm, and (c) 375 nm during a laser on/off cycle at a fluence of 2.3 J/cm^2. The arrows pointing down indicate when the laser was turned on and the arrows pointing up indicate when the laser was turned off

Transient absorption at 153 nm. Additional evidence for the role of impurity hydrogen in the *transient* absorption at 153 nm was provided by comparing the transient signals from polished samples annealed in hydrogen, in air, and in oxygen. The annealing treatments were performed at 500 °C for two hours. Figure 7 shows the transmission drop for each sample at a fluence of 1.8 J/cm^2, where the signals have been translated vertically to the same initial transmission value. In each case, the samples were exposed to 18,000 pulses before acquiring

the transient signals. The largest transmission drop is observed for the sample annealed in H_2, consistent with absorption by a hydrogen-related defect. The smallest transmission drops were observed for the sample annealed in O_2 and the sample tested immediately after polishing. An intermediate transmission drop was observed for the sample annealed in air—possibly due to hydrogen produced by the dissociative absorption of airborne water. These treatments had no measurable effect on transient absorption at 220 nm. The hydrogen anneal did increase the transient absorption at 375-nm somewhat, consistent with the enhanced rates of F-center production observed by Bessent *et al*. during x-irradiation of CaF_2 annealed in hydrogen.[18]

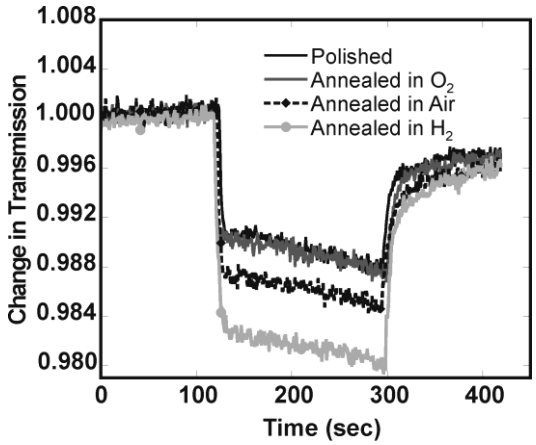

Fig. 7. Transmission signals acquired during a laser on/off cycle at a fluence of 1.8 J/cm^2 for four CaF_2 samples annealed at 500° C for 2 h in the indicated atmospheres.

We note that samples annealed in hydrogen at 500 °C for two hours showed no VUV absorption at 153 nm prior to exposure to F_2 laser radiation. However, samples annealed at a somewhat higher temperature (700 °C for 2 hours—data not shown) do show an absorption peak at 153 nm. The appearance of transient transmission changes at 153 nm in samples that have not been annealed in hydrogen indicates that the transient measures are a significantly more sensitive probe of hydrogen in the CaF_2 lattice than simple VUV spectroscopy. This may be due to the incorporation of hydrogen in H_I^0 as well as H_S^- centers.

Growth of transient amplitude at 153 nm and 220 nm. As noted above, the amplitude of the transient absorption drop ($T_i - T_{RA}$) at 153 nm starts small and reaches a steady state value after sufficient 157-nm exposure. This is shown explicitly in Figs. 8(a) and 8(b), where the amplitudes of the transient absorption changes at 153 and 220 nm are plotted as a function of laser exposure at 2.1 J/cm^2. The transient transmission amplitudes at these two wavelengths grow over the first 15 min, which corresponds to about 9000 laser pulses, and subsequently plateau.

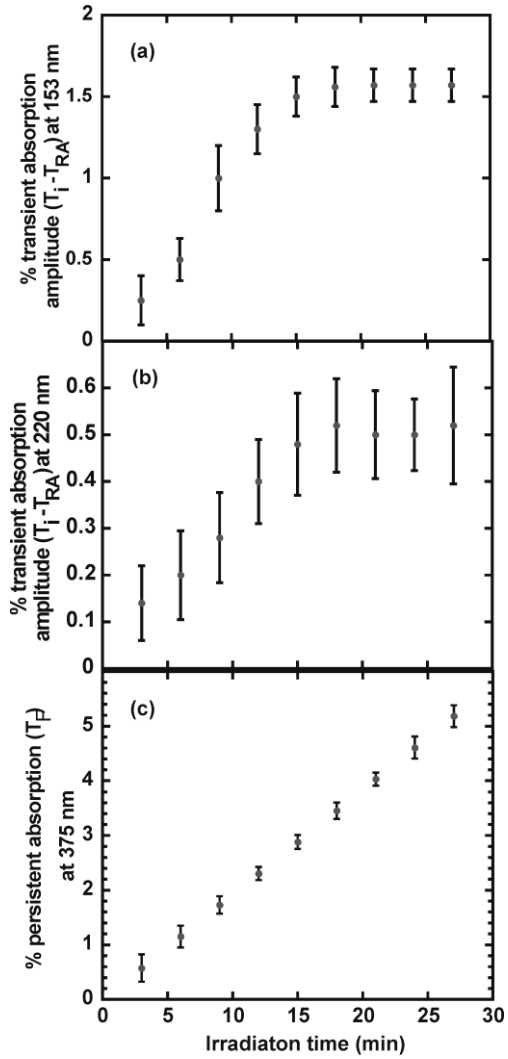

Fig. 8. Transmission change amplitudes ($T_i - T_{RD}$) at (a) 153 nm and (b) 220 nm as a function of laser exposure at a fluence of 2.1 J/cm^2. (c) Transmission at 375 nm (T_f) plotted as a function of exposure under the same conditions.

The transient transmission signals are very small in the early stages of irradiation. At the onset of irradiation, the production of free electrons by the laser (mostly by two-photon excitations across the band gaps) is insufficient to generate significant H_s^- and Ca_I^{1+} densities from their respective precursor defects. In the early stages of irradiations, the production of free electrons requires two-photon excitations across the band gap.

Much higher free electron densities in the presence of ionizable electron traps, such as F-centers and F-center aggregates. F-centers, and M-centers are readily ionized by single 7.9 eV photons.[25,26] Although other defects (principally nanoparticles) contribute to the transmission at 375-nm, the amplitude of the transmission change at this wavelength provides a crude indication of how the F-center densities evolve with time during prolonged irradiation. The persistent transmission change [plotted as an absorption, $(1 - T_f)$] at 375 nm as a function of exposure is shown in Fig. 8(c), also at 2.1 J/cm^2. As expected, the initial F-center densities are low—consistent with a low density readily ionizable electron traps at the onset of exposure.

In contrast with the transmission changes at 153 and 220 nm, the transmission at 375 nm decreases in a linear fashion throughout the longest exposures employed in this work. This suggests that the density of ionizable electron traps increases in a similar fashion. If so, the plateau in the transient absorption signals in Figs. 8(a) and 8(b) is not due to a shortage of free electrons, but due to the limited densities of H_s^- and Ca_I^{1+} precursor defects. After about 9000 laser pulses, we appear to be converting nearly all the precursor defects to absorbing H_s^- and Ca_I^{1+} defects.

Effect of 157-nm radiation on transmission recovery at 375 nm. The transmission signals in the F-center band (375 nm) are significantly affected by the history of exposure. The gray curve in Fig. 9 shows a transmission signal during a typical laser on/off cycle at a fluence of 2 J/cm^2. This signal is comparable to the signal of Fig. 6(c), acquired at 2.3 J/cm^2. The dark curve shows a comparable signal where, instead of turning the laser off at time t = 200 s, the laser fluence was reduced to 0.8 J/cm^2. The presence of the low fluence, 157-nm radiation for times t > 200s has greatly accelerated the transmission recovery. Further more we found that in

absence of the probe beam the recovery is slower than with the probe beam. The Deuterium lamp has an intense line at 160 nm and so it appears that absorption close to 160 nm enhances the recovery process.

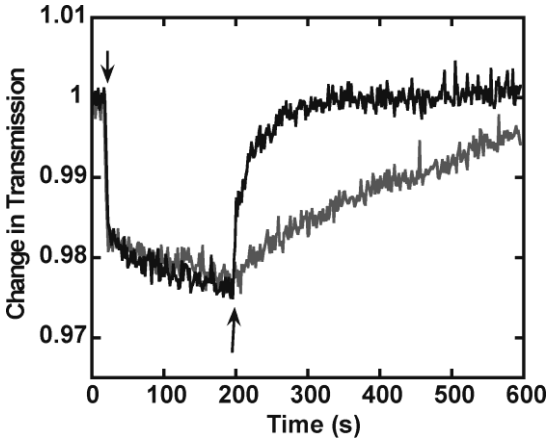

Fig. 9. Transmission signals acquired at 375 nm for a cleaved sample at an initial fluence of 2 J/cm^2. The dark curve shows the normal transmission response when the laser is turned off at time t = 200 s. The gray curve shows the transmission response to a simple reduction in laser fluence to 0.8 J/cm^2 at time t = 200 s. Recovery is much faster when the laser fluence is reduced, as opposed to being turned completely off.

In a study of F-center aggregation in CaF_2, Kotomin *et al*. have suggested that the activation energy for F-center diffusion can be reduced by electronic excitations.[27] Their results were consistent with an activation energy for diffusion of 0.7 eV without excitation, and 0.4 eV with excitation. Mobile F-centers can aggregate with other F-centers to form a variety of aggregate centers. They can also recombine with interstitial fluorine. Both processes would destroy F-centers and increase transmission at 375 nm. Both processes would proceed more rapidly if the activation energy for F-center diffusion drops significantly. When the laser fluence is reduced, the rate of F-center production drops markedly, but the F-center mobility may remain high. The balance between defect creation and annihilation shifts dramatically when the laser fluence is lowered from 2 to 0.8 J/cm^2, in favor of rapid annihilation. The same but smaller

effect is also observed with just the probe beam which is not as intense as the laser but also contains a line at 160 nm.

Models for transmission changes at 153 nm and 220 nm. To model the transient transmission changes at 153 and 220 nm, we proposed that absorbing H_S^- and Ca_I^{1+} interstitial color centers are produced when free electrons produced by the laser are captured at precursor sites. For the sake of definiteness, we propose that these precursor sites are neutral, substitutional hydrogen, H_S^0, and interstitial Ca_I^{2+}, respectively. The transmission recovers when the absorbing centers loose their electrons, probably by trapping holes released from hole traps after the laser is turned off.

During laser exposure, electron and hole trapping (color center creation and annihilation) operate in parallel. When the laser is turned off, free electrons are no longer generated, and hole trapping (color center annihilation) dominates. We focus first on the simpler, second case, with the laser off, where only one process (color center annihilation) operates. Both H_S^- and Ca_I^+ center are destroyed by hole capture. These reactions are special cases of bimolecular annihilation, which take the from $A + B \rightarrow 0$. For H_S^- annihilation, we identify A with the H_S^- center, B with the hole, h^+, and 0 with the inert defect H_I^0. The annihilation of the Ca_I^+ is described similarly.

The kinetics of bimolecular annihilation can be modeled using rate equations. We assume the annihilation rate is proportion to the product of the participating defect densities.

$$\frac{d[H_s^-(t)]}{dt} = -C[H_s^-(t)][h^+(t)] \tag{3}$$

where C is a rate constant. When hole transport can be described in terms of a random walk between metastable trapping sites, C can be interpreted as the number of sites visited by the hole per unit time.[28]

To solve Eq. (3) we need to express $[h^+]$ in terms of $[H_S^-]$. Models incorporating the assumption that the density of mobile holes is much greater than the density of H_S^- centers were found to describe the data, but the resulting best-fit parameters were consistent with nearly equal densities ($[h^+] \approx [H_S^-]$). In the work below, we explicitly assume that the densities are equal. Letting $A = [h^+] = [H_S^-]$, Eq. (3) becomes

$$\frac{dA(t)}{dt} = -CA(t)^2 \tag{4}$$

Equation (4) has solutions of the form

$$A(t) = \frac{A_0}{(1 + CA_0 t)} \tag{5}$$

where $A_0 = [H_S^-]_{t=0}$ is the initial H_S^- center concentration—that is, the concentration immediately before the laser is turned off. Our transient transmission changes are small (usually less than 2%), so the transmission change due to H_S^- will be proportional to $[H_s^-]$ to a good approximation. The transient change at 153 nm then becomes:

$$T(t) = T_r - \alpha A(t) = T_r - \frac{\alpha A_0}{(1 + CA_0 t)_0} \tag{6}$$

where α is the constant of proportionality and T_r is the transmission in the long time limit. The same equation applies to transient transmission signal at 220 nm after replacing the H_S^- center densities with Ca_I^{1+} densities.

Figure. 10 shows transmission signals at 153-nm and 220-nm during the recovery stage (with the laser off), along with fits of Eq. (6). Here $t = 0$ corresponds to the onset of recovery, when the F_2 laser beam is blocked. The model provides a good description for both signals.

This is consistent with a bimolecular annihilation reaction that destroys the absorption when a hole is captured by an H_S^- center or a Ca^{1+} interstitial. Both initial defect densities increase with fluence, as expected. Conversely, rate constant *C* is independent of fluence, consistent with rate-limited transport of holes to the annihilation sites.

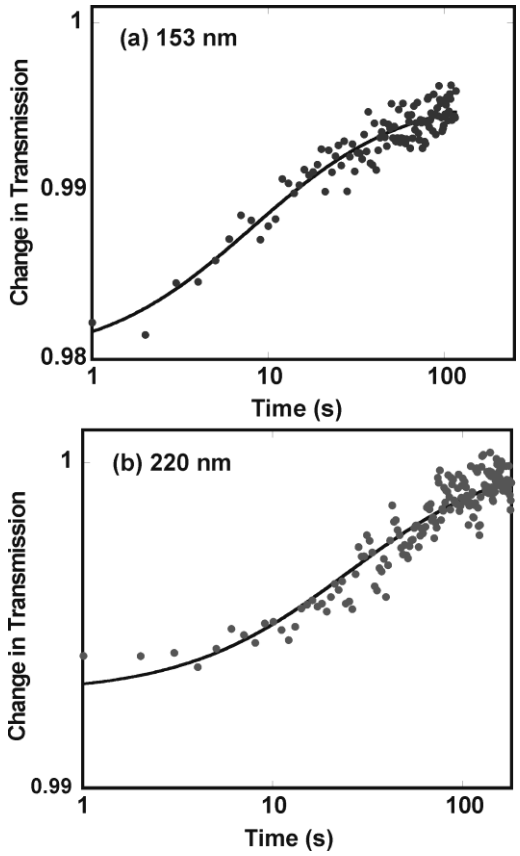

Fig. 10. Transmission signals plotted during the recovery stage of a laser on/off cycle at (a) 153 nm and (b) 220 nm. The lines show fits of Eq. (8) to the data.

To model the transmission drop at the onset of laser exposure, we add a source term to the rate equation to account for defect production. The simplest assumption is to assume that color centers are produced at a constant rate (that should depend on laser fluence). Since our curve fit results suggested that the color center and hole densities were nearly equal during transmission recovery, we will assume this holds during the transient transmission drop as well. We also assume that the defect densities do not change dramatically between laser pulses, so that

we can replace the instantaneous defect density with an average. The rate equation then becomes:

$$\frac{dA(t)}{dt} = S - CA(t)^2 \tag{7}$$

where S is the average rate of defect production when the laser is on. This equation has solution:

$$A(t) = \sqrt{\frac{S}{C}} \tanh\left(\sqrt{SC}t\right) \quad , \tag{8}$$

and corresponding transmission signal is

$$T(t) = 1 - \alpha A(t) = 1 - \alpha\sqrt{\frac{S}{C}} \tanh\left(\sqrt{SC}t\right) \quad . \tag{9}$$

Equation (9) provides a good description of the transmission drops at 153 and 220 nm at modest fluences and short times. However, at the high fluence of the fluence range employed, the 153 nm signal displays a noticeable, *persistent* change in transmission during single laser on/off cycles. These are not described by Eq. (9). For the sake of completeness, we found that the transmission drop under these conditions could be modeled by a simple linear transmission drop that applied whenever the laser was on. This is consistent with the linear drop in transmission at 153 nm observed during prolonged irradiation, as Fig. 1. Most of this drop is persistent, not transient, and is likely due to VUV absorption by nanoparticles. The full model then becomes:

$$T(t) = 1 - mt - \alpha\sqrt{\frac{S}{C}} \tanh\left(\sqrt{SC}t\right) \tag{10}$$

where m is the rate at which transmission drops due to colloid production.

Log-log plots of transmission signals at 153 and 220 nm during the laser on stage of a laser on/off cycle are shown in Figure 11. This data was acquired at a fluence of 2.2 J/cm^2 and a pulse repetition rate of 10 Hz. The parameter *C* (recombination rate) is independent of fluence for both signals, consistent with transport limited defect annihilation. If transport were thermally activated, and if the sample temperature were significantly changed by laser exposure, we would expect *C* to vary with fluence. This is not observed.

Reactions (1a) and (1b) require electrons. As reported above, we believe these electrons are supplied by the ionization of F- and F-aggregate centers, and not two-photon excitations across the band gap. The amplitude of the transmission drops at 153 and 220 nm are plotted in the insets of Fig. 12. Although the data are noisy, the magnitude of the transmissions drops are almost proportional to fluence at both wavelengths. This is consistent with the electron production by the single photon ionization of F- and F-aggregate centers.

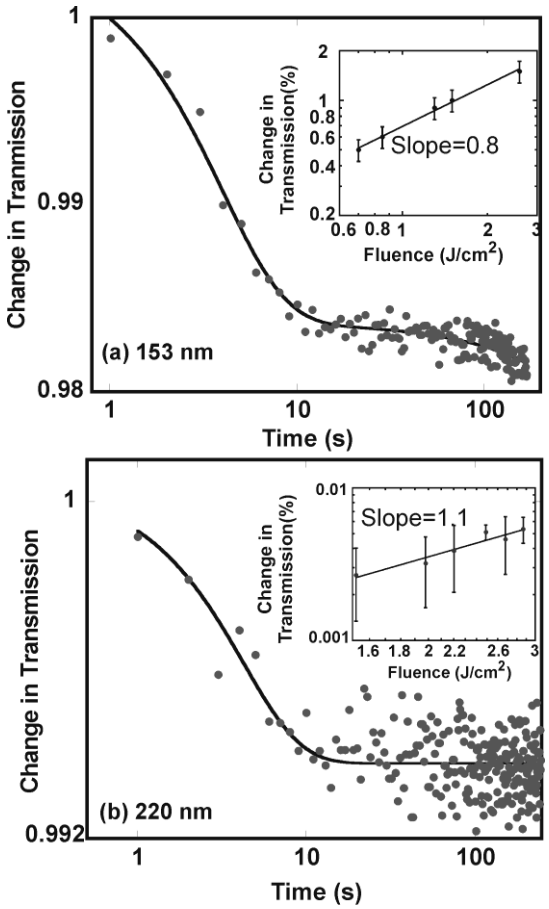

Fig. 11. Transmission signals during the transmission drop stage of a laser on/off cycle at (a) 153 nm and (b) 220 nm. The dark lines show fits of Eq. (11) to the data. The fluence dependence of the magnitude of the fast drops [$(T_i - T_{RD})$, where T_{RD} is measured after the first 30 laser pulses] are shown in the insets.

Model for transmission changes at 375 nm. F-centers in intrinsic CaF_2 are produced by the nonradiative decay of excitations produced when a free electron is captured by a self-trapped hole. These excitations are produced by two-photon excitations across the band gap. To form an F-center, a neutral fluorine atom moves from a lattice site to a distant interstitial site. Fluorine interstitials are immobile at room-temperature. As noted above, F-centers have limited mobility at room temperature; ionized F-centers appear to be much more mobile. Thus F-centers can be produced by two photon excitations across the band gap, and can be destroyed by vacancy-interstitial recombination when a diffusing F-center encounters an interstitial.

F-centers readily aggregate to form more complex defects. The simplest of these is the M-center—an F-center pair. In the limit of large aggregates, the fluorine vacancies donate their electrons to form metallic calcium metal. This process is possible in part because the molar volume of calcium metal is similar to the molar volume of calcium ions in CaF_2. Thus there are two processes which can consume F-centers: recombination at interstitials and aggregation with other F-centers to form F-center aggregates. Both annihilations reactions are second order in the F-center density, and Eq. (7) applies.

Figure 12(a) shows data acquired during the recovery stage of the transient transmission signal at 375 nm on a log-log plot, along with a least squares fit of Eq. (7) to the data. The fit is good, and the value of *C* is independent of the transmission value immediately before the laser was turned off (T_f above). When Eq. (7) is used to fit the much faster recovery observed when the fluence is merely reduced in Fig. 9, the best fit value of *C* is increased by a factor of about 20—consistent with our hypothesis that low fluence laser radiation increases the defect annihilation rate by increasing the F-center mobility. The fit to the transmission recovery curve in Fig. 10 is not as good as the fit in Fig. 12(a)—possibly because the low fluence (0.8 J/cm^2) allowed for some defect production.

If formation of F-center aggregates accounts for transmission recovery we suggest that the fast drop in transmission when irradiation is restored is most likely due to dissociation of these aggregates. Figure 12(b) shows a log-log plot of the transmission drop stage of a transient transmission signal at 375 nm. The dark line is a least squares fit of Eq. (10) to the data. Interestingly, the value of *C* in Eq. (10) fit the transmission drop stage of the laser on/off cycle (laser on) is about 20 times the value of *C* in Eq. (7), fit to the transmission recovery stage (laser off). A similar difference was observed for the data of Fig. 10, between the C value for transmission recovery with the laser off and recovery with the laser fluence reduced to 0.8 J/cm^2.

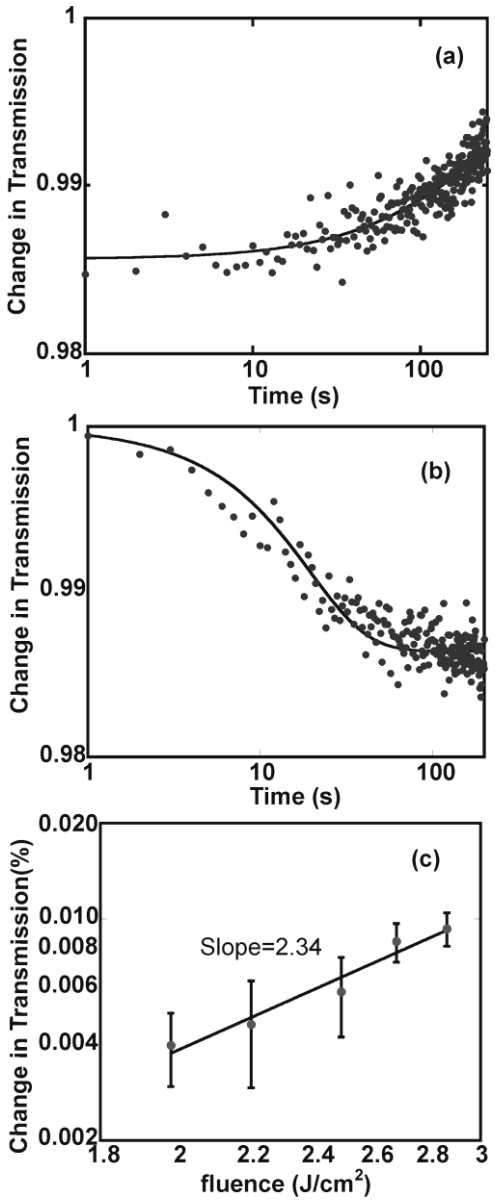

Fig. 12. Transmission signals at 375 nm during the (a) recovery and (b) initial drop stages of a laser on/off cycle. The lines show fits of Eq. (8) [in (a)] and Eq. (11) [in (b)] to the data. (c) The fluence dependence of the magnitude of the fast drops ($T_i - T_{RD}$), where T_{RD} is measured after the first 30 laser pulses.

Fig 12(c) shows the amplitude of the transmission drop during the laser-on portion of a laser on/off cycle as a function of fluence. The slope of the line is about 2 and suggests a two-photon process. This is inconsistent with charge transfer reactions like those responsible for the transient absorptions at 153 and 220 nm. Heating of the sample during irradiation can be non-

linear and if thermal dissociation of F-center aggregates is the process by which the fast drop in transmission is produced then one would expect a non-linear fluence dependence.

4. Discussion

We observe both persistent and transient changes in transmission during 157-nm irradiation of CaF_2. In previous work, we observed transient changes in the transmission of 157-nm laser radiation when the 157-nm intensity was cycled from low values to about 8 J/cm^2 and back again.[1] At the highest fluences, the transmission change approached 50%. This is well above the 2% transient changes observed at 153 nm associated with the H_s^- defect. The previously reported, large transmission changes at high fluences almost certainly due to the growth and bleaching of the colloid absorption hear 160 nm; in the work above, this appears as a persistent, rather than transient change. At the high fluences used in previous work (up to 8 J/cm^2), 157 nm irradiation would locally heat the largest nanoparticles and promote fluorine diffusion to the fluorine-free colloid material. This process would be facilitated by the mobility of ionized F-centers,[27] which helps account for the fast transmission recovery at much lower fluences in Fig. 9 above.

Mühlig *et al*. observed transient transmission changes of about 2% at 193 nm during 193-nm irradiation at fluences less than 10 mJ/cm^2.[2] These changes took place over tens of thousands of pulses, and were fully recoverable. No persistent transmission change was observed. The only transmission changes we observe in this region correspond to the tail of the colloid band near 160 nm in Fig. 2(a). That said, it is not clear that any of the transmission changes we observe could be responsible for the transient change reported by Mühlig *et al*.

In some contexts, the transient transmission changes described above are more sensitive to some defects than other optical methods. For instance, we observe transient transmission changes at 153 nm attributed to the H_s^- center in CaF_2 [Fig. 6(a)] that had not been intentionally treated to introduce hydrogen. VUV spectra of these same samples show no clear features in this

region, either before or after prolonged exposure to 157 nm laser radiation [Fig. 2(a)]. We conclude that most of the hydrogen in our calcium fluoride initially does not form H_s^- centers. In CaF_2 doped with trivalent rare earths, for instance, negative hydrogen ions can occupy other lattice positions that do not absorb at 153 nm. When nominally pure CaF_2 is exposed to 10,000, 157-nm pulses at fluences above 1 J/cm^2, much of this hydrogen is apparently converted to H_s^- centers which are readily detected in the transient VUV absorption.

The F-centers formed during 157-nm exposure at the relative high fluences employed for the transient transmission measurements reported above are probably necessary for the detection of the H_s^- and Ca_I^+ transient transmission signals at 153 and 220 nm, respectively. The VUV detection of hydrogen and interstitial calcium may prove useful for material used in applications where these defects are detrimental. For instance, interstitial calcium is an anti-site defect, and probes the lattice order of the crystalline material. Given the F-center densities required to observe the signals, transmission measurements would count as destructive testing in many cases.

5. Conclusions

In this study we have presented evidence of transient VUV and UV absorption in CaF2 with peaks at 153 nm, 220 nm and 375 nm under 157-nm irradiation and attribute them to the H_s^- center, Ca^{1+} interstitial and the F-center in CaF2. Samples annealed in H_2 show an increase in the transient absorption at 153-nm consistent with H impurity being responsible for absorption at this wavelength. All three peaks show a drop of 1-2 % in transmission over 1800 pulses. When irradiation is terminated we observe transmission recovery at all three wavelengths that attain a constant value after approximately 180 sec in the case at 153 nm and 220 nm and over 1200 sec at 375 nm. After this recovery the transmission can be brought down to the previously induced value within a few pulses. This transient absorption is affected by surface treatments suggesting that the surface defects play a role in this absorption. We propose that capture of

holes at H_S^- center and the Ca^{1+} interstitial destroys the absorption at these wavelengths and that trapping of an electron at H_I^0 center, Ca^{2+} re-induces absorption. For the F-center we suggest that aggregation of F-centers leads to loss of absorption at 375 nm and the dissociation of F-aggregates when irradiation is restored re-induces absorption. A bimolecular annihilation model provides a good description of the drop and recovery of transmission at all three wavelengths. Irradiation also produces persistent darkening in the crystal at 160, 375, and 560 nm. We show here that the persistent darkening at 160 nm and 550 nm are related and propose that the persistent absorption at 160 is due to the free electron Plasmon of Ca nanoparticles.

Acknowledgment

This work was supported by the U.S. Department of Energy under Grant DE-FG02-04ER-15618.

References

1 L. P. Cramer, S. C. Langford, and J. T. Dickinson, "The formation of metallic nanoparticles in single crystal CaF_2 under 157 nm excimer laser radiation," J. Appl. Phys. **99,** 054305 (2006).

2 C. Mühlig, W. Triebel, G. Töpfer, J. Bergmann, S. Brückner, C. Chojetzki, and R. Martin, in *Advanced Characterization Techniques for Optics, Semiconductors, and Nanotechnologies, SPIE Proceedings Vol. 5188*, edited by A. Duparre and B. Singh (SPIE, Bellingham, WA USA, 2003), p. 123-133.

3 S. M. Avanesyan, S. Orlando, S. C. Langford, and J. T. Dickinson, in *Ultrafast Phenomena in Semiconductors and Nanostructure Materials VIII*; *Vol. 5352*, edited by K.-T. Tsen, J.-J. Song, and H. Jiang (SPIE—The International Society for Optical Engineering, Bellingham, WA, 2004), p. 169-179.

[4] S. M. Avanesyan, S. Orlando, S. C. Langford, and J. T. Dickinson, "Point defect production by ultrafast laser irradiation of alkali-containing silica glasses and alkali halide single crystals," Appl. Surf. Sci. **248,** 129-137 (2005).

[5] J. T. Dickinson, S. C. Langford, S. M. Avanesyan, and S. Orlando, "Color center formation in KCl and KBr single crystals with femtosecond laser pulses," Appl. Surf. Sci. **253,** 7874-7878 (2007).

[6] V. M. Orera and E. Alcalá, "Optical properties of cation colloidal particles in CaF_2 and SrF_2," Phys. Scripta **44,** 717-723 (1977).

[7] F. Beuneu and P. Vajda, "Radiation-induced defects in CaF_2: An electron-spin resonance and dielectric constant investigation," J. Appl. Phys. **78,** 6989-6993 (1995).

[8] M. Reichling, "The role of defect diffusion and metallization for electron-stimulated desorption from CaF_2," Nucl. Instrum. Meth. Phys. Res. B **101,** 108-114 (1995).

[9] L. P. Cramer, B. E. Schubert, P. S. Petite, S. C. Langford, and J. T. Dickinson, "Laser interactions with embedded Ca metal nanoparticles in single crystal CaF_2," J. Appl. Phys. **97,** 074307 (2005).

[10] P. O. Nilsson and G. Forssell, "Optical properties of calcium," Phys. Rev. B **16,** 3352-3358 (1977).

[11] L. W. Hobbs, "Point defects stabilization in ionic crystals at high defect concentrations," J. Phys. (Paris) **37,** 3-25 (1976).

[12] V. M. Orera and E. Alcalá, "Formation and size evolution of Ca colloids in additively colored CaF_2," Physica Status Solidi (a) **38,** 621-627 (1976).

[13] V. M. Orera and E. Alcalá, "Photothermal bleaching of Ca colloids in additively colored CaF_2," Solid State Commun. **27,** 1109-1112 (1978).

[14] M. L. Sanjuan, P. B. Oliete, and V. M. Orera, "The enhanced raman scattering of phonons in CaF_2 and MgO samples containing Ca and Li colloids," J. Phys.: Condens. Matter **6,** 9647-9657 (1994).

[15] K. S. Song and R. T. Williams, *Self-Trapped Excitons*, Vol. 105, 2nd ed. (Springer, Berlin, 1996).

[16] R. Bennewitz, C. Günther, M. Reichling, E. Matthias, S. Vijayalakshmi, A. V. Barnes, and N. H. Tolk, "Size evolution of low energy electron generated Ca colloids in CaF_2," Appl. Phys. Lett. **66,** 320-322 (1995).

[17] J. H. Beaumont, J. V. Gee, and W. Hayes, "Absorption in the vacuum ultraviolet of alkaline earth fluorides containing hydrogen," J. Phys. C **3,** L152-L154 (1970).

[18] R. G. Bessent, W. Hayes, J. W. Hodby, and P. H. S. Smith, "An investigation of the effects of x-rays on undoped and on hydrogen doped alkaline earth fluorides," Proceedings of the Royal Society of London. Series A, Mathematical and Physical Sciences **309,** 69-90 (1969).

[19] J. H. Beaumont, W. Hayes, D. L. Kirk, and G. P. Summers, "An investigation of trapped holes and trapped excitons in alkaline earth fluorides," Proceedings of the Royal Society of London. Series A, Mathematical and Physical Sciences **315,** 69-97 (1970).

[20] D. Messner and A. Smakula, "Color centers in alkaline earth fluorides," Phys. Rev. **120,** 1162–1166 (1960).

[21] A. D. Franklin, "Born model calculation of defect energies in CaF_2," Journal of Physics and Chemistry of Solids **29,** 823-841 (1968).

[22] K.-D. Li, H. Y. Xiao, and L. M. Wang, "Computer simulation study of defect formation and migration energy in calcium fluoride," Nucl. Instrum. Meth. Phys. Res. B **266,** 2698-2701 (2008).

[23] B. C. Cavenett, W. Hayes, I. C. Hunter, and A. M. Stoneham, "Magneto optical properties of F centres in alkaline earth fluorides," Proceedings of the Royal Society of London. Series A, Mathematical and Physical Sciences **309,** 53-68 (1969).

[24] C. Görling, U. Leinhos, and K. Mann, "Comparative studies of absorptance behaviour of alkaline-earth fluorides at 193 nm and 157 nm," Appl. Phys. B **74,** 259-265 (2002).

[25] H. Shi, R. I. Eglitis, and G. Borstel, "*Ab initio* calculations of the CaF_2 electronic structure and *F* centers," Phys. Rev. B **72,** 045109 (1-9) (2005).

[26] H. Shi, R. I. Eglitis, and G. Borstel, "*Ab initio* calculations of the oxygen—vacancy dipoles and M centers in CaF_2," Computational Materials Science **39,** 430-436 (2007).

[27] E. A. Kotomin, V. N. Kuzovkov, and A. I. Popov, "The kinetics of defect aggregation and metal colloid formation in ionic solids under irradiation," Radiat. Eff. Defects Solids **155,** 113-125 (2001).

[28] H. Schnörer, V. Kuzovkov, and A. Blumen, "Bimolecular annihilation reactions with immobile reactants: Unequal reactant concentrations," J. Chem. Phys. **93,** 7148-7152 (1990).

CONCLUSIONS

Laser-induced positive ion emission has been observed from fused silica under 157-nm irradiation. These ions often have kinetic energies well in excess of the incident photon energy. The covalent nature of the Si-O bond in silica argues against a purely electrostatic emission mechanism for ion emission. These emissions are attributed to the production of chemical states whose antibonding character is sufficient to yield emission (the Menzel-Gomer-Redhead mechanism). Neutral atoms and molecules (O, Si and SiO) are emitted by defect interactions along the surface; these defects are produced principally by the photo-induced cleavage of strained bonds. Negative ions are produced *after* the laser pulse by electron attachment to neutral O and Si and SiO.

Quadrupole time- and mass-resolved measurements of neutral particles emitted during the laser ablation of PTFE at 157 nm show intense signals due to $(CF_2)_N$ fragments, where N ranges from $N = 1$ to the upper limit of our mass filter, $N = 6$. The observation of intense emissions at masses other than the monomer rule out thermally-activated depolymerization of the polymer chain as an important source of material removal. The high kinetic energies (about 0.6 eV) and fluence dependence (typically 1.7^{th} order) of the faster fragments are consistent with emission due to photochemical scission of C-C bonds. These observations provide strong support to previous arguments for the photochemical etching of PTFE at 157 nm.

It was found that fragments greater than our mass spectrometer range (up to 2000 amu) are produced during ablation of PTFE at 157 nm. The broad range of emitted masses during 157-nm ablation of PTFE is unique and unlike laser ablation for other materials and gives rise to some unique and unusual behavior in the way it expands. Heavy fragments are emitted away from the surface normal, almost parallel to the surface. This behavior is due to pressure gradients created within the cloud of emitted fragments due to which heavy fragments are accelerated away from the surface normal. These pressure gradients arise due to the Gaussian

beam profile of the F_2 excimer laser. 2-dimensional hydrodynamic calculations of plumes with two components (high pressure light fragments and low pressure heavy fragments) support this contention. These calculations also reveal that by creating the above conditions in the plume one can obtain high quality uniform thin-films of PTFE over large areas. This study also shows that due to the presence of heavy fragments off-normal deposition might be more efficient in producing high quality PTFE thin than deposition along the surface normal.

Transient VUV and UV absorption was observed in CaF_2 with peaks at 153 nm, 220 nm and 375 nm under 157-nm irradiation and attribute them to the H_s^- center, Ca^{1+} interstitial and the F-center in CaF_2. Samples annealed in H_2 show an increase in the transient absorption at 153 nm consistent with H impurity being responsible for absorption at this wavelength. All three peaks show a drop of 1-2 % in transmission over 1800 pulses. When irradiation is terminated we observe transmission recovery at all three wavelengths that attain a constant value after approximately 180 sec in the case at 153 nm and 220 nm and over 1200 sec at 375 nm. After this recovery the transmission can be brought down to the previously induced value within a few pulses. This transient absorption is affected by surface treatments suggesting that the surface defects play a role in this absorption.

We propose that the H_s^- center and the Ca^{1+} interstitial exist in the crystal; capture of a hole by these defects destroys the absorption at these wavelengths and that trapping of an electron at these sites re-induces absorption. For the F-center we propose that aggregation of F-centers to form M-centers leads to loss of absorption at 375 nm and the dissociation of the M-center when irradiation is restored re-induces absorption. A bimolecular annihilation model provides a good description of the drop and recovery of transmission at all three wavelengths. Irradiation also produces persistent darkening in the crystal at 160, 375, and 550 nm. We show here that the persistent darkening at 160 nm and 550 nm are related and propose that the persistent absorption at 160 is due to the free electron Plasmon of Ca colloids.